UiT Norges arktiske universitet

Faculty of Science and Technology
Department of Geosciences

# Engineering geology of the Jettan rockslide, Kåfjorden

**Jørgen Nicolai Berg**

GEO-3900 Master's thesis in Geology, May 2020

i

# Abstract

The unstable rock slope (URS) Jettan is located at Nordnesfjellet in Kåfjorden municipality in Troms and Finnmark County, 800 m above the fjord. The rockslide has an estimated volume of 6 Mm$^3$, and moving at a rate of up to 50 mm a$^{-1}$. Jettan is considered a "high risk object" within the Norwegian unstable mountain framework. This is due to the potential displacement wave impact to housings, infrastructure and industry. As such there has been a scientific interest in the site since 1999 generating several studies, reports, investigations and theses. Continuous monitoring began in 2007.

The goal of this thesis was to gain a larger understanding of the unstable rock slope and its driving mechanisms. To do this, exiting data on lithology and structure, geophysics, borehole investigations, seasonal movement trends, past avalanche activity, published geological models and engineering geology studies were reviewed. This array of data was complimented by the work of this thesis including in-depth lithological study, rock mass descriptions, detailed geomorphological mapping, an updated analysis of movement and external drivers. The existing data, and the data gaps covered by this thesis, allowed the construction of a 3D model. Previous studies have shown that Jettan is highly seasonally controlled. High movement rates are recorded in the spring due to snow melting and a continuous deformation in the autumn is considered to be due to permafrost processes. Analysis in this thesis confirmed seasonal variations at Jettan, with high deformation in the summer, lower deformation in the winter and a lower but continuous deformation in the autumn. Jettan is a complex URS with areas showing different morphology, movement direction and movement rates. As dip of the foliation is rarely above 25°, a possible sliding surface is assumed to be a combination of foliation planes and joint sets building a stepped sliding surface. In field a repeating weakness zone was found parallel to the foliation, and it is suggested that it contributes to the overall reduction of the stability for the slope together with groundwater processes. In the boreholes the main sliding surface was interpreted to be at 45 m bgl. The 3D model supports both a stepped and planar sliding surface, and suggested several possible failure scenarios. New volume estimates gave a volume of 7.87 Mm$^3$, for the most realistic larger failure scenario. This is a larger estimate than previous studies, and the greater depth to the sliding surface in this interpretation is seen as the main reason for a larger volume in the 3D model.

# Acknowledgments

# Table of Contents

# Abbreviations

| | |
|---|---|
| URS | Unstable rock slope |
| DEM | Digital elevation model |
| InSAR | Interferometric Synthetic Aperture Radar |
| LOS | Line of sight |
| OTV | Optical televiewer |
| bgl | Below ground level |
| asl | Above sea level |
| BP | Before present |
| ka | Thousand years |
| NGU | Geological Survey of Norway |
| NVE | Norwegian Water Resources and Energy Directorate |
| NGI | Norwegian Geotechnical Institute |
| DMS | Differential Monitoring of Stability |
| UCS | Unconfined compressive strength |
| GSI | Geological Strength Index |

# 1 Introduction

## 1.1 Background of the study

Norway is a country of dramatic landforms with steep mountains plunging into the sea and fjords. The landscape has been formed over millions of years throughout several geological events and glacial cycles. Unstable mountainsides pose hazards in exposed areas and can cause landslides. Landslides can lead to infrastructure disruption and damage, and at worst fatalities. Landslides can also result in secondary consequences, for example displacement waves within a fjord or a lake (Hermanns et al., 2012c). This can be catastrophic, since most people in Norway live close to the coastline and therefore stay inside the hazard zone. In Norway over 33,000 historic landslide events have been registered causing 4,475 fatalities as of 2011 (Hermanns et al., 2012a). Looking at the ten most adverse mass movements, five of them are directly associated with slope failure or a subsequent displacement wave (Hermanns et al., 2012a).

A mountain area which is partly or fully detached from its surrounding rock and has started moving, is termed as a unstable rock slope (URS) (Høst et al., 2006). When the movement is rapid through a sudden event by fall, gliding or as a stream it is referred to as an avalanche. In Norway avalanches in hardrock are divided into different categories according to their volume. This is because the volume has a major impact on the potential damaging effect (NGI, 2019). By definition rockfall has a volume below 100 $m^3$, rock avalanches have a volume up to 100,000 $m^3$ and volumes above 100,000 $m^3$ are termed a rockslide (Høst et al., 2006).

A big step towards reducing the consequences of landslides in Norway has been to map, evaluate and monitor unstable mountain areas. The Geological Survey of Norway (NGU) started systematic mapping and classification of unstable rock slopes in 2005. Since 2009 this work has been on commission from the Norwegian Water Resources and Energy Directorate (NVE). NVE does the monitoring of the high-risk objects mapped by NGU to be able to evacuate people from hazard areas before a catastrophic rock slope failure event occurs. URSs often go through an acceleration phase before potentially failing (Petley, 2004). Observing movement rates could therefore theoretically predict when the failure will occur and alert people in exposed areas. In Norway over 300 unstable areas or potential unstable areas have been mapped (NGU, 2019b). A classification system to evaluate the hazard and risk level was

established to determine which sites should be permanently monitored for evacuation purposes (Hermanns et al., 2014).

Nordnesfjellet in Kåfjord municipality consists of an area called Jettan. This is a large active unstable rock slope on the flank of Storfjorden. The rockslide is estimated to be around 6 $Mm^3$, and moving at a rate of up to 50 mm $a^{-1}$ (Blikra et al., 2009; Blikra et al., 2012). Jettan is considered a "high risk object" within the Norwegian unstable mountain framework. This is due to the potential displacement wave impact to housings, infrastructure and industry (yearly probability of 1/100 - 1/1000) (NGU, 2019b). 11 objects are periodically monitored in Norway, while Jettan is one of the six URSs that are constantly monitored. The site has been continuously monitored since 2007 by GPSs, lasers, extensometers, crackmeters, tiltmeters, borehole instruments (DMS), web-cameras and a metrological station (NVE, 2019).

## 1.2 Aim of the study

The aim of this research project is to gain a greater overall understanding of the URS Jettan, by analyzing the slope in 3D and investigating the mechanical controls on the rockslide movement. There is a large amount of existing literature regarding Jettan. A big part of this thesis will consist of putting all the literature together for a greater overall understanding of the area.

The following question will be answered in this thesis:

- What are the main geological structures present in the area?
- What are the main failure zones of the rockslide?
- What are the characteristics of the failure zones (depth, strength, thickness, repetition etc.)?
- What are the main controls on the movement of the rockslide?
- Can movement rates be linked to the groundwater levels, and what affect may failure zones have on groundwater flow (or vice-versa)?

To answer these questions the following tasks have been done:

- Conduct a review of previous studies outline the main geology and bedrock structures in the area.
- Provide an upgraded morphostructure map of the unstable area.
- Interpolate failure zones from borehole logging, downhole geophysics and surface mapping.
- Link movement rates, vectors and failure zones for a fuller understanding of how the slide is deforming.
- Link movement rates with meteorological records.
- Assimilate all data into Leapfrog Geo for creation of a 3D model.

## 1.3 Available data

As well as data collected from field campaigns as a part of this project, many other published studies present data from Jettan. This includes mapping (Blikra et al., 2009; Braathen et al., 2004; Skrede, 2013) and investigated using logged borehole cores (Ganerød, 2013, 2014), televiewer data from boreholes (Elvebakk, 2013, 2014), permafrost investigations (Blikra et al., 2014), continuous monitoring data (Nordvik et al., 2010), ground- and satellite- based radar and InSAR (Eriksen et al., 2017a; Eriksen et al., 2017b; Lauknes et al., 2010; Skrede, 2015), geophysics (Rønning et al., 2008; Tønnesen et al., 2004), tunnel design report (Blikra & Bunkholt, 2012), stability analysis (Nystad, 2014), displacement wave modeling (NGI, 2007, 2013, 2018) and looking at cores, bathymetry and seismic data in the fjord to reconstruct past activities (Hegstad, 2014).

Other available datasets which have been utilised are presented in table 1.

*Table 1: Datasets, source and resolution used in the project.*

| Data | Source, date | Resolution |
|------|-------------|-----------|
| Drone photos | Fieldwork, 2018-19 | 72 dpi |
| Orthophotos | Kartverket, 2016 | 0.25 m |
| Aerial photos | NVE and NGU | |
| Monitoring data | NVE, 05.2010 – 05.2020 | |
| InSAR data | NGU, 07.2016 – 09.2020 (NGU, 2020) | |
| Borehole data | NGU, lithology, core loss, foliation, joints and fracturing (Elvebakk, 2013, 2014; Ganerød, 2013, 2014) | |

## 1.4 Study area

### 1.4.1 Location

Jettan is a part of Nordnesfjellet mountain in Troms and Finnmark county (figure 1). The unstable area is located between 0 and 800 m asl on the W-facing slope of the mountain. Jettan neighbors two other URSs at Nordnesfjellet, Midtre Nordnes and Indre Nordnes, forming a complexly deforming mountain ridge. The mountain ridge is bound by Storfjorden on the western side, and Kåfjorden and Manndalen valley on the eastern side. The fjords merge north of Nordnesfjellet, where they become Lyngenfjord, which is traced northward to the continental shelf. The Lyngen Alps stands out with the highest mountains in the area, including some peaks over 1800 meters. Nordnesfjellet is less dramatic with a flat mountaintop at 900 m asl and is therefore considered as part of the paleic surface. Below the URS the main road connecting Troms and Finnmark (E6) used to pass, but a tunnel has now been constructed going through Nordnesfjellet. This has resulted in less traffic in the impact hazard zone.

*Figure 1: Left: Location of the Jettan rockslide on the western side of Nordnesfjellet mountain, in Troms and Finnmark county in northern Norway. The black rectangle shows the location at Nordnesfjellet. Right: URSs are delineated using backscarps, and field station location is indicated. Based on 2016 aerial photograph (Google, 2019; Kartverket, 2016, 2019).*

## 1.4.2 Climate and weather?

The climate in Troms and Finnmark county varies according to location, which also affects the movement rates for an URS. The county has a mild and humid coast climate characterized by large amounts of precipitation, and a relatively dry inland climate. This is attributed to the complex and mountainous topography of the coast, making the flatter inland areas more sheltered. Precipitation can range from 1000-1500 mm $a^{-1}$ at the coast, to 300-600 mm $a^{-1}$ at the inland (Dannevig, 2019). A great variation is also seen in temperatures between the coast and the inland parts. The lowest temperatures reach -10 to -15°C at the coast, with a mean temperature of -2°C. In the inland areas the lowest temperatures reach -30 to -40°C, with a mean temperature of -15°C. In the warmest months of the summer the mean temperatures are 11-12°C by the coast and around 14°C in the inland (Dannevig, 2019).

Jettan lies at the transition from a steep coastal landscape to flatter plateau-like morphology inland. A weather station was installed at the URS in 2008, 791 m asl. The weather station measures air temperatures, ground temperatures, wind strength and direction, sunshine duration, humidity, precipitation, snow depth and barometric pressure. The average air temperature is positive in May/June and usually dips under zero from October. The coldest period is in January to March, whereas the warmest is in July. The average temperature is around 10°C in the summer and approximately -10°C in the winter. The ground temperatures react slower to changes, therefore the ground gets above and below zero around a month later than the air temperatures. The average temperature in the summer is below 10°C and in the winter the average is rarely below -5°C. The wind is strongest in the winter and typically blowing from the south/southeast. Summer is the season with the greatest amount of precipitation (May to September), and the annual precipitation is usually over 300 mm. The snow cover is in general greatest in April (Norsk_Klimaservicesenter et al., 2020).

# 2  Literature review

The Jettan rockslide has been a subject of studies, reports, investigations and theses since 1999. In the following chapter a summary of the work done at Jettan is presented. The rockslide has been heavily mapped (Blikra et al., 2009; Braathen et al., 2004; Skrede, 2013) and investigated using logged borehole cores (Ganerød, 2013, 2014), televiewer data from boreholes (Elvebakk, 2013, 2014), permafrost investigations (Blikra & Christiansen, 2014), continuous monitoring data (Nordvik et al., 2010), ground- and satellite- based radar and InSAR (Eriksen et al., 2017a; Eriksen et al., 2017b; Lauknes et al., 2010; Skrede, 2015), geophysics (Rønning et al., 2008; Tønnesen & Dalsegg, 2004), tunnel design report (Blikra & Bunkholt, 2012), stability analysis (Nystad, 2014), displacement wave modeling (NGI, 2007, 2013, 2018) and looking at cores, bathymetry and seismic data in the fjord to reconstruct past activities (Hegstad, 2014).

The site has also been continuously monitored since 2007, and is monitored with installations as extensometers, crackmeters, tilt-meters, GNSS, ground-based radar, laser, borehole instruments recording vibrations, water levels and temperature, meteorological station and web cameras (NVE, 2019). Ongoing projects of the site is this thesis and a study regarding structurally controlled rock slope deformation in northern Norway by Vick et al. (2020).

## 2.1  Regional geology

The bedrock in Troms County consists of metamorphic pre-Cambrian rock overlain by Caledonian Nappe sequences. These rocks have been deformed though several ductile geological events, as well as post-Caledonian rifting sand Quaternary glacial cycles.

The pre-Cambrian basement rocks are mainly gneisses, volcanic and sedimentary supracrustal rocks with an age ranging from Archean to Proterozoic age. These rocks are to be found in Finnmark, on the coast at West-Troms and in some tectonic windows in Alta-Kvænangensvinduet and Sørkjosvinduet (Zwaan, 1988). Most of the region is covered in Caledonian Nappe rocks, including Nordnesfjellet.

## 2.1.1 Caledonian nappes

The Caledonian nappes have been built up by four different Allochthon thrust events: the Uppermost-, Upper-, Middle- and Lower Allochthon (Ramberg et al., 2006). The first three can be found in Troms County (figure 2).

The study area is located in the Reisa Nappe Complex, rocks of the Upper Allochthon, comprising the Vaddas-, Kåfjord- and Normannvik Nappe (Zwaan, 1988). The nappes were thrust up in the Silurian, with the Normannvik Nappe representing the highest in the sequence, and the Vaddas Nappe the lowest. The nappes have gone through metamorphoses with increasing grade upwards in the packages. Vaddas Nappe consists of volcanic and sedimentary rocks, Kåfjord of garnet mica schists with amphibole as layers and lenses and Normannvik Nappe of mica-schist in combination with calcite-marble and dolomite (Zwaan, 1988).

During the orogeny, shear zones formed close to the thrust faults which bound the different nappes and thrust them on top of each other. The orogeny did not only form shear zones, but the deformation has also resulted in the formation of ductile fabrics including folds and foliation (Zwaan, 1988).

Two different nappes have been identified at Jettan. The Kåfjord nappe is mapped at the base of the slope, comprising garnet mica schist with kyanite and staurolite (NGU, 2019c). The boundary between the Kåfjord and overlying Normannvik Nappe is mapped at ca. 200 m asl, and within the Normannvik Nappe packages of gneiss, calcite-marble, garnet-mica-schist and dolomite marble are present.
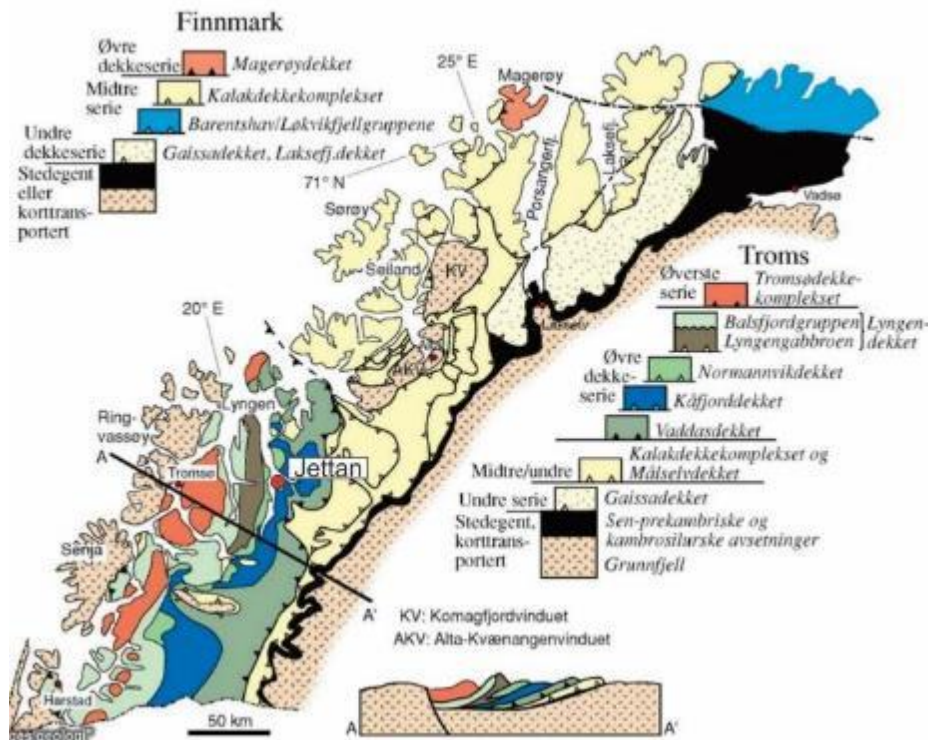
*Figure 2: Nappe sequence in Troms and Finnmark. Modified from Ramberg et al. (2006).*

### 2.1.2 Post-Caledonian lineaments and structures

After the Caledonian orogeny an extensional phase began, and the collapse of the orogeny was initiated leading to the opening of the Atlantic Ocean (Ramberg et al., 2006). Bergh et al. (2007) suggested that the rifting happened in several stages starting in the Perm-Jurassic and ending in the Paleogene. The rifting led to faults striking NW-SE, NNE-SSW and NE-SW (Indrevær et al., 2013).

There are two major fault complexes seen in Northern Norway with a post Caledonian origin, the Vestfjorden-Vanna and the Troms-Finnmark fault complexes (Indrevær et al., 2013). They are characterized by moderate to steep dipping normal faults trending NNE-SSW and ENE-WSW found partly onshore and partly offshore, and they are bound by a major horst, the West Troms Basement Complex (WTBC) (Indrevær et al., 2013). Northward from the southern part of the Troms-Finnmark fault complex the Ringvassøya-Loppa fault complex is displayed showing an N-S trend (figure 3). Indrevær et al. (2013) suggested that the faulting was happening on pre-existing Precambrian and Caledonian structures in the bedrock as for example ductile shear zones and lithological boundaries.
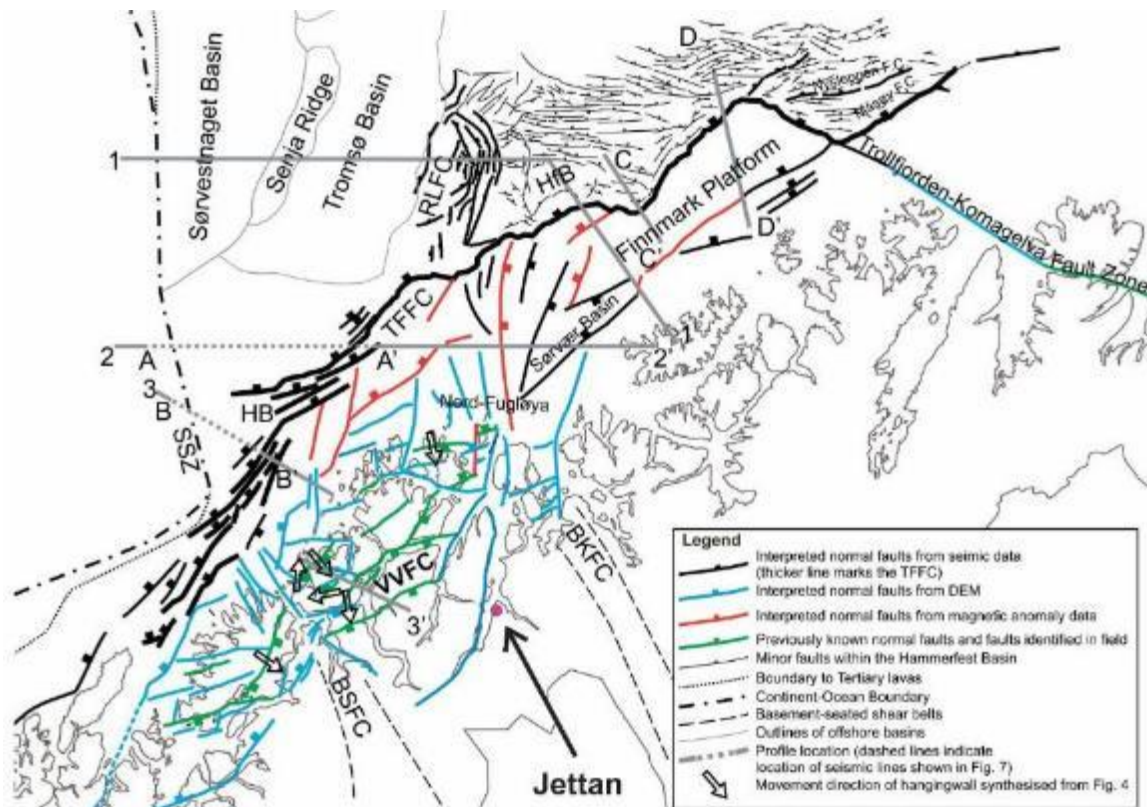
*Figure 3: Mapped Post-Caledonian normal faults in Northern Norway. Modified from Indrevær et al. (2013)*

The largest structural lineaments in central Troms around the study area is oriented NNE-SSW to N-S e.g. Lyngenfjorden and Ullsfjorden, E-W to ENE-WSW e.g. crossing Reisadalen towards Kåfjorden, and NW-SE e.g. Normannvikdalen and Rotsunddalen (Zwaan, 1988). The Normannvikdalen feature/fault is discussed to either be a normal fault of neotectonic origin (Dehls et al., 2000), or as a surface expression of a deep-seated gravitational slope deformation (DSGSD) or creep of topsoil (Redfield et al., 2016).

West of Nordnesfjellet the Lyngen peninsula stretches and is characterized by steep triangular faced spurs that dips into Lyngenfjorden, a feature commonly observed along active normal faults (Osmundsen et al., 2010). InSAR data suggests that the Lyngen peninsula is the horst and the footwall of a normal fault (Lyngenfault), and areas east the hanging wall including Nordnesfjellet (Osmundsen et al., 2010). The hanging wall is subsiding by a few mm $a^{-1}$ in comparison to the footwall (Osmundsen et al., 2010). There are some uncertainties around the interpretation of this fault, as Satens Vegvesen has not registered vertical movement of the southern part of Storfjorden (Blikra & Bunkholt, 2012).

At Nordnesfjellet two lineaments striking E-W to WNW-ESE one along Innerbuktlia and one at Indre Nordnes from Lyngenfjorden to Manndalen, and several lineaments striking NE-SW is mapped (figure 4) (Zwaan, 1988). From filed investigation and aerial photos several other lineaments were found (figure 4). The lineaments at Nordnesfjellet has been interpreted as faults from the fact that at least some of them show a discontinuity in the lithology.



*Figure 4: Lineaments and bedrock map at Nordnesfjellet. Modified from NGU (2019c).*

### 2.1.3  Quaternary geology

Glaciers have had a big impact on the landforms seen in Norway and in the study area in Troms (Ramberg et al., 2006). U-valleys and fjords have been formed through glacial erosion, and isostatic uplift from rebound has exposed steep rock slopes (Ramberg et al., 2006).

The Quaternary is characterized by multiple climatic fluctuations as a result of the Milankovich cycles (Berger, 1988; Nesje, 2012). The last ice age, the Weichsel, lasted from 117 to 11.5 ka (Nesje, 2012). Ice retreat following the Weichsel occurred as smaller fluctuations before complete deglaciation. A re-advance during the Younger Dryas (ca. 11-10 ka) resulted in the formation of the most dominant moraine in Troms County, the Tromsø-Lyngen moraine, which shows marked terminal and lateral moraines. In Lyngenfjorden, the Tromsø-Lyngen moraine is seen north of Jettan, at Spåknes just south of Rotsundet (figure 5). From 9.9 – 9.8 ka ± 150 years, the ice had retreated south of Jettan to Ørnes in Lyngen, called the Ørnes event (Corner, 1980). At the same time an ice-front accumulation was deposited at Holmen in Kåfjordalen (Corner, 1980). At a later stage a new ice-front accumulation was deposited at Skibotn, the Skibotn event, at ca. 9.6-9.5 ka ± 150 years (Corner, 1980).
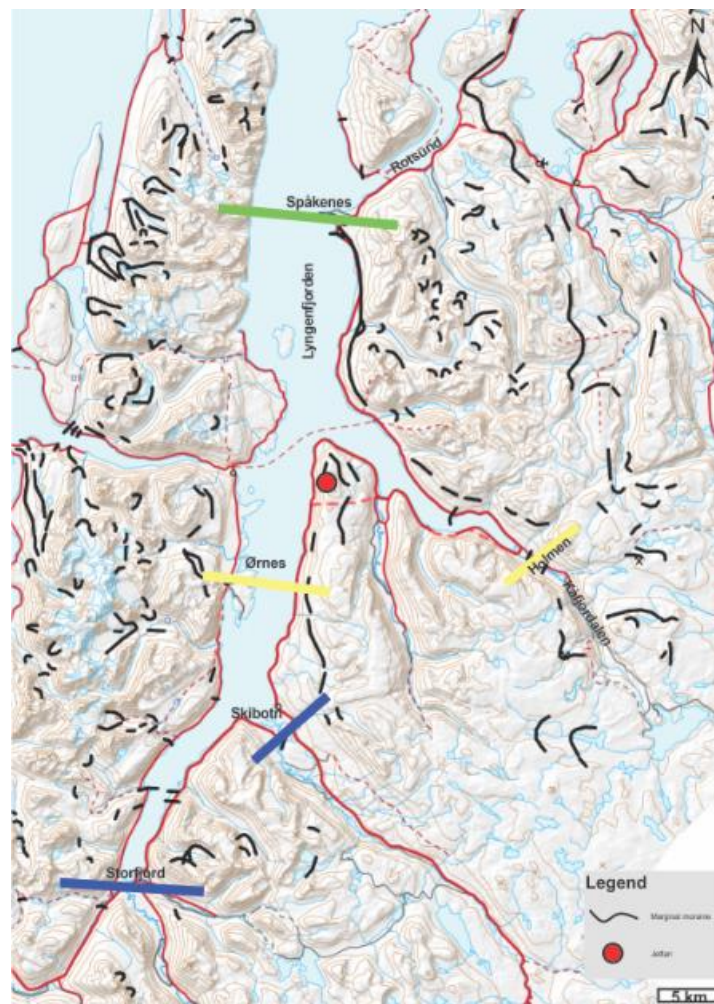


*Figure 5: The ice front position during the deglaciation and marginal moraines. Green line = Tromsø - Lyngentrinnet, yellow line = the Ørnes event and blue line = the Skibotn event. Modified from NGU (2019a) (CORNER, 1980).*

At Nordnesfjellet marginal moraines are mapped on both slope aspects, with a more dominant moraine morphology on the eastern side (figure 5). The moraine ridges are mapped at 700 m asl in the south and 500 m asl in the northern outer end of the peninsula (NGU, 2019a). One of these moraine ridges is seen at Jettan, where it has collapsed into a big fracture (Blikra & Christiansen, 2014).

## 2.2 Geology at the site

### 2.2.1 Structures and morphology

The URS is bound by an inherited normal fault oriented NE-SW at the southern border, and by a joint controlled backscarp oriented NW-SE at the northern border (Blikra et al., 2009; Blikra et al., 2006; Braathen et al., 2004; Skrede, 2013). There has been some different interpretations on where the backscarp of the unstable area is located in the uppermost part. Blikra and Bunkholt (2012) have included the outer limit of the upper marble dome as the backscarp, while others interpreted the backscarp to be in front of the marble to the west (Skrede, 2013). Jettan is usually divided into different domains or sub-areas based on the structural and morphological expression as well as movement rates and direction. Dividing it into northern, southern and upper eastern domain has been the most popular (Blikra & Christiansen, 2014; Eriksen et al.,

2017a; Eriksen et al., 2017b), while Skrede (2013) has divided it into seven different sub-domains from A to G.
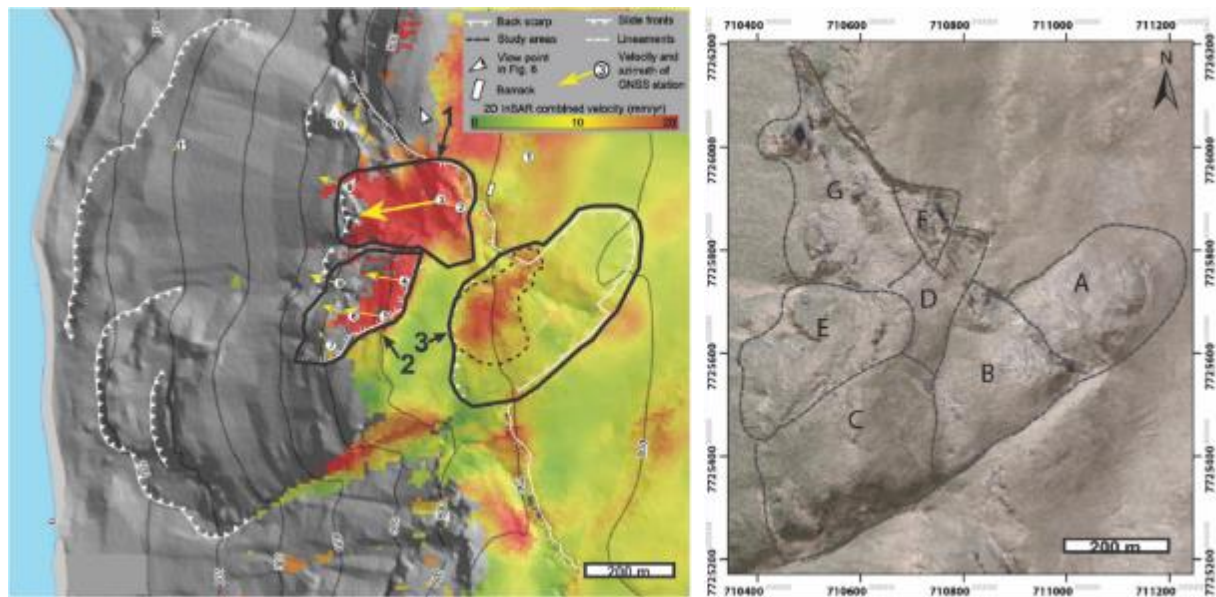


*Figure 6: Left: The most popular domains divided into northern (1), southern (2) and upper (3), modified from Eriksen et al. (2017b). Right: Skrede (2013) domains divided from A-G.*

I will now present the different morphological findings of these studies using the former.

The northern domain (figure 6), located west of the field station, is a complex area built up by a dominating NW-SE-striking back-scarp, a blocky field with disintegrated materials and two dominating large dislocated blocks. The blocks are aligned with the backscarp and divided by large synthetic or antithetic fractures (Eriksen et al., 2017a; Skrede, 2013).

In the southern domain (figure 6) a simpler geometry is observed with a scarp-terrace-scarp morphology. At the rear a large fracture divides the area from a less steep area behind, and in the south the area is cut by a scarp orientated parallel to the NE-SW striking fault (Eriksen et al., 2017a; Skrede, 2013). The scarps are oriented NNE-SSE, aligning with the upper back fracture which delineates the subdomain, while they are oriented NE-SW further downslope indicating more movement in the southern part of the terraces (Eriksen et al., 2017a; Skrede, 2013).

South of the southern domain consists of a bigger terrace and its underlying scarps and smaller terraces (Skrede, 2013). The joints here are dominantly oriented NE-SW and NW-SE building up zigzag patterns in the upper scarps (Skrede, 2013). To the north, a NE-SW striking scarp divides the area from the southern domain, and to the south a large sub vertical wall aligned with the NE-SW striking normal fault marks the outer boundary of the unstable area (Eriksen et al., 2017a; Skrede, 2013). Sequences of marble and garnet-mica-gneiss build up the wall, and big persistent joints could be found (Eriksen et al., 2017a; Skrede, 2013).

At the upper domain (figure 6) in the highest elevation of the URS a gentle protrusion in the terrain is found and has been interpreted as a marble dome (Eriksen et al., 2017a; Skrede, 2013). Extensional fractures dominate the marble dome. A steep hillside divides the marble from the underlying talus-dominated area to the west, and is interpreted to be part of the backscarp and the start of the active part of the URS (Skrede, 2013). The area below the marble dome is separated in the southern part by the NE-SW striking fault and is dominated by talus material of marble in the upper and eastern part, and some scarps to the west (Eriksen et al., 2017a; Skrede, 2013). In the northwestern part several parallel scarps align with the backscarp (Eriksen et al., 2017a; Skrede, 2013). In the middle to lower parts of the URS talus material and avalanche deposits from previous events dominate, but some scarps and lobes are present. The area is moderately vegetated except of some parts covered by recent rockfall activity. A large

column is to be found in the lower northwestern area and is referred to as "Jettankallen" in Norwegian.
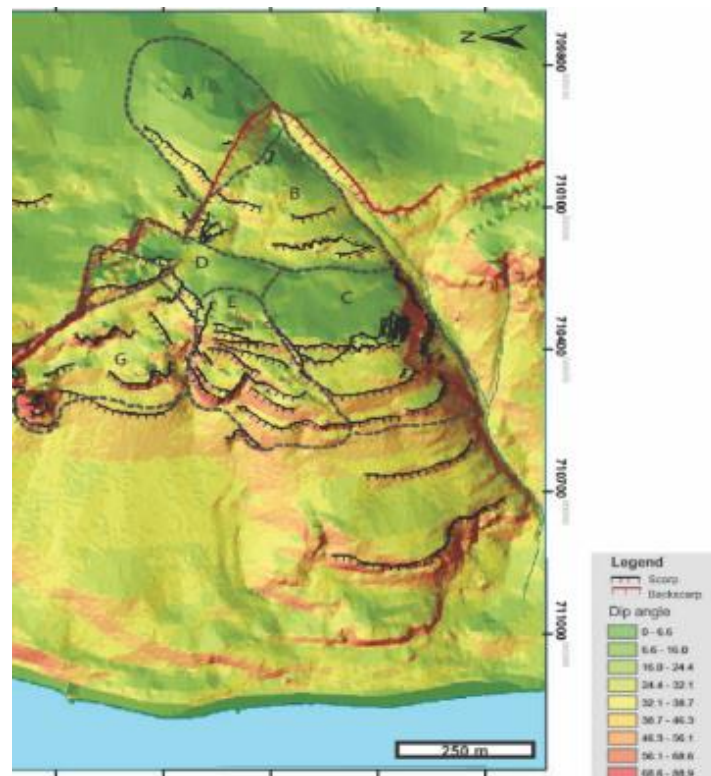


*Figure 7: Scarps and dip angle at Jettan with the different domains used by Skrede (2013). Modified from Skrede (2013).*

Three main joint sets are found at Jettan (figure 8). The most dominant joint set (J1) is oriented NE-SW dipping 55-90° towards NW, and because of its steep dip it is also dipping towards SE. Joint set two (J2) is oriented ESE-WNW dipping 50-90° towards N and 60-90° towards S. The last joint set (J3) is oriented NW-SE dipping 70-90° towards SW and NE (Nystad, 2014). Additionally there are two joint sets oriented NNE-SSW and NNW-SSE (table 2) (Skrede, 2013). The persistence of the joints has a dominating planar trend with constant dip angle.

Furthermore it was observed listric joints, joints making a stepped geometry with the foliation and joints changing their dip when entering a different lithology (Skrede, 2013).

Foliation at Jettan is measured to be sub-horizontal with a dip rarely above 20-25° (figure 8B). The dip direction varies from dipping towards SW and NW in general, but with the small dip angle only small variations could lead to a different dip direction Nystad (2014); (Skrede, 2013)
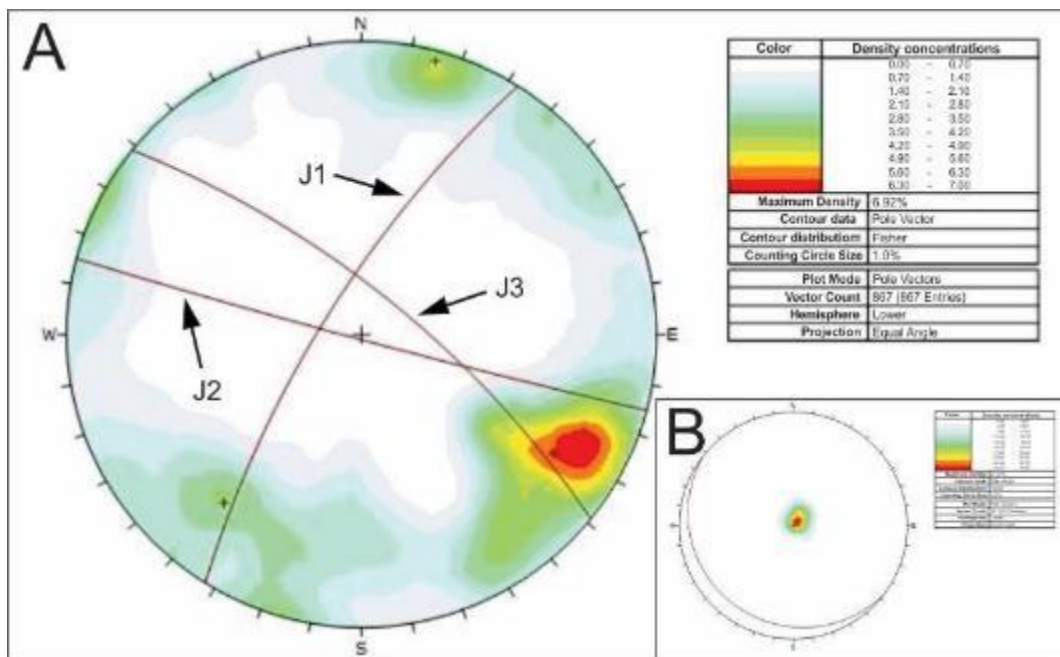


*Figure 8: Stereographic plot of the structural measurements at Jettan. A) Joint measurements visualized as contour plot with great circles representing the main joint sets. B) Measurements of foliation visualized as contour plot. Modified from (Nystad, 2014).*

*Table 2: Dip and dip direction for the different joint sets*

|    | Dip   | Dip direction              |
|----|-------|----------------------------|
| J1 | 55-90 | NW/SE (~302) (Nystad, 2014) |
| J2 | 50-90 | N/S (~195) (Nystad, 2014)   |
| J3 | 70-90 | SW/NE (~40) (Nystad, 2014)  |
| J4 | >60   | WNW (Skrede, 2013)          |
| J5 | >60   | ESE (Skrede, 2013)          |

### 2.2.2 Lithologies at Jettan

Nordnesfjellet is divided by a major nappe boundary separating the Nordmannvik and the Kåfjord nappe, and is comprised of three dominant lithologies: garnet quartz mica gneiss, calcite silica gneiss and marble (figure 4) (NGU, 2019c). The garnet quartz mica gneiss is expressed as a blastomylonite or as more schist when it contains a higher mica content (Skrede, 2013). In areas with high mica content the rock has fractured along big, flat foliation surfaces. Where it has been exposed for weathering, the rock is more weathered and decomposed (Skrede, 2013). The calcite silica gneiss consists of layers that are either carbonate rich or silica rich, ranging from a few centimeters to 10's of meters thick (Skrede, 2013). The rock is exposed in bands throughout the whole area with greater thickness in the lower scarps (figure 9) (Skrede, 2013). The marble is found in the upper most part of the unstable area, and as a lens in the steep back scarp, a displaced block and Jettankallen in the northwest (figure 9) (Skrede, 2013). In the URS different ductile deformation structures are present in various scale, as blastomylonites in the garnet mica gneiss, sheet folds in quartz layers, boudins (from centimeters to meters) in calcite silica gneiss and minor folds in amphibole rich calcite silica gneiss layers (Skrede, 2013).
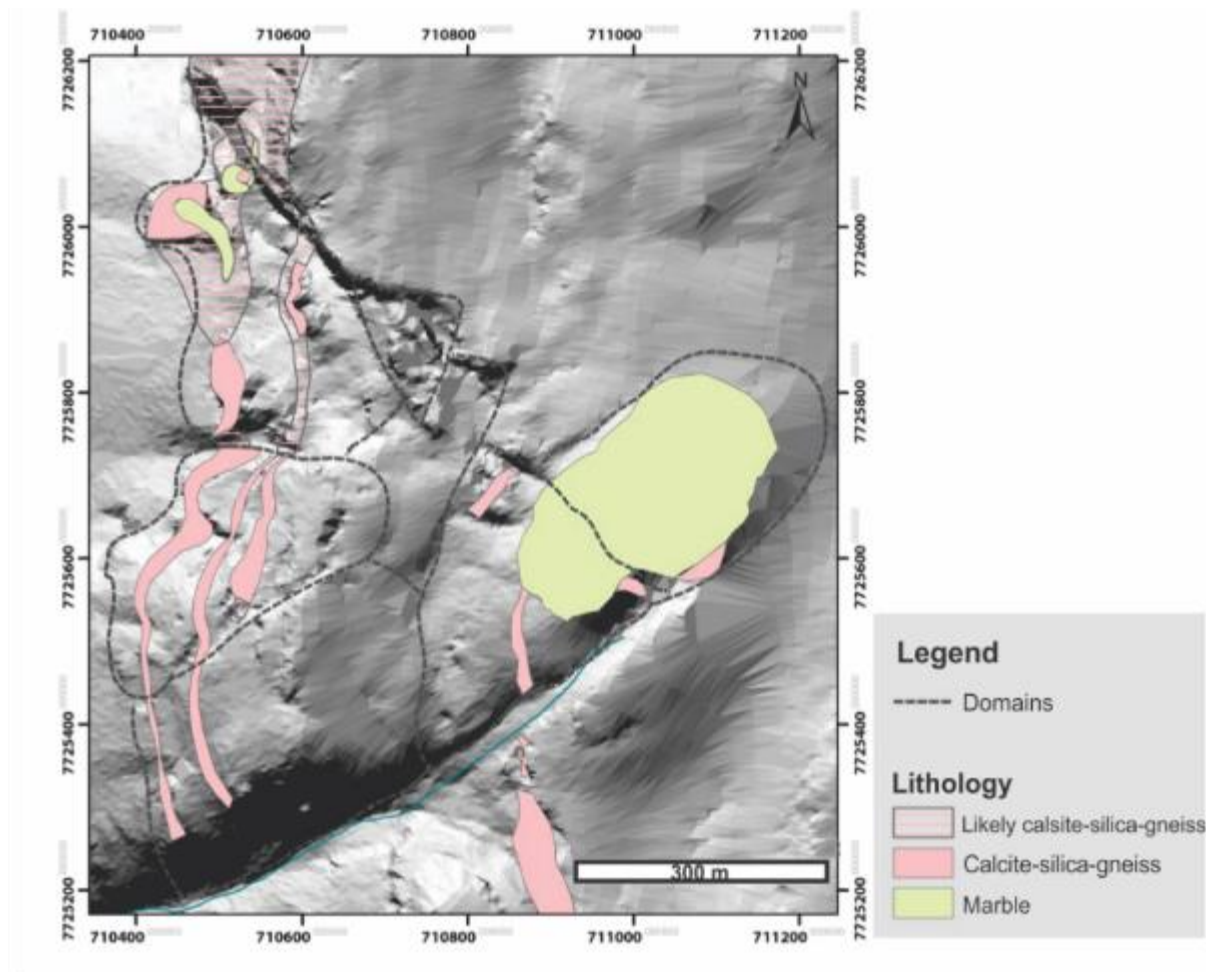
*Figure 9: Bedrock map of Jettan, non-colored consists of garnet-quartz-mica-gneiss (Skrede, 2013).*

## 2.3 Geophysical investigations

Geophysical profile investigations were done at Nordnesfjellet in 2003 and 2007 as part of the project "Risk and vulnerability analyses of rock avalanches in Troms" (Rønning et al., 2008; Tønnesen & Dalsegg, 2004). The goal of the investigation was to examine the controlling structures of the URS and their extent and thickness, as well as looking for permafrost at depth. Low resistivity values, indicated by areas of cold colors on figure 10, 11 and 12, may indicate a structural weakness as highly crushed rock would increase the water content and therefore lower the resistivity. High resistivity values, indicated by worm colors, maybe express drained talus, weathered rock or permafrost. (Rønning et al., 2008).

Seven profiles including 2D resistivity, geo-radar and seismic were conducted (figure 13). Resistivity profile 1 showed a weakness zone in the center of the profile in connection with the

NW-SE backscarp with a dip towards east, and east of this zone a possible weak zone dipping towards west (figure 10 and 13) (Tønnesen & Dalsegg, 2004). Resistivity profile 2 showed a weakness zone in the center of the profile in connection with the NW-SE striking backscarp with a sub vertical dip, and indications that it could be a smaller vertical weakness zone in the SW of the profile (figure 11 and 13) (Tønnesen & Dalsegg, 2004). Resistivity profile 3 revealed weakness zones close to or at the NE-SW striking fault, expressed as one bigger and one smaller zone with a vertical dip, and one weakness zone outside of the unstable area to the SE also seen in connection with an old fault (figure 12 and 13) (Rønning et al., 2008).
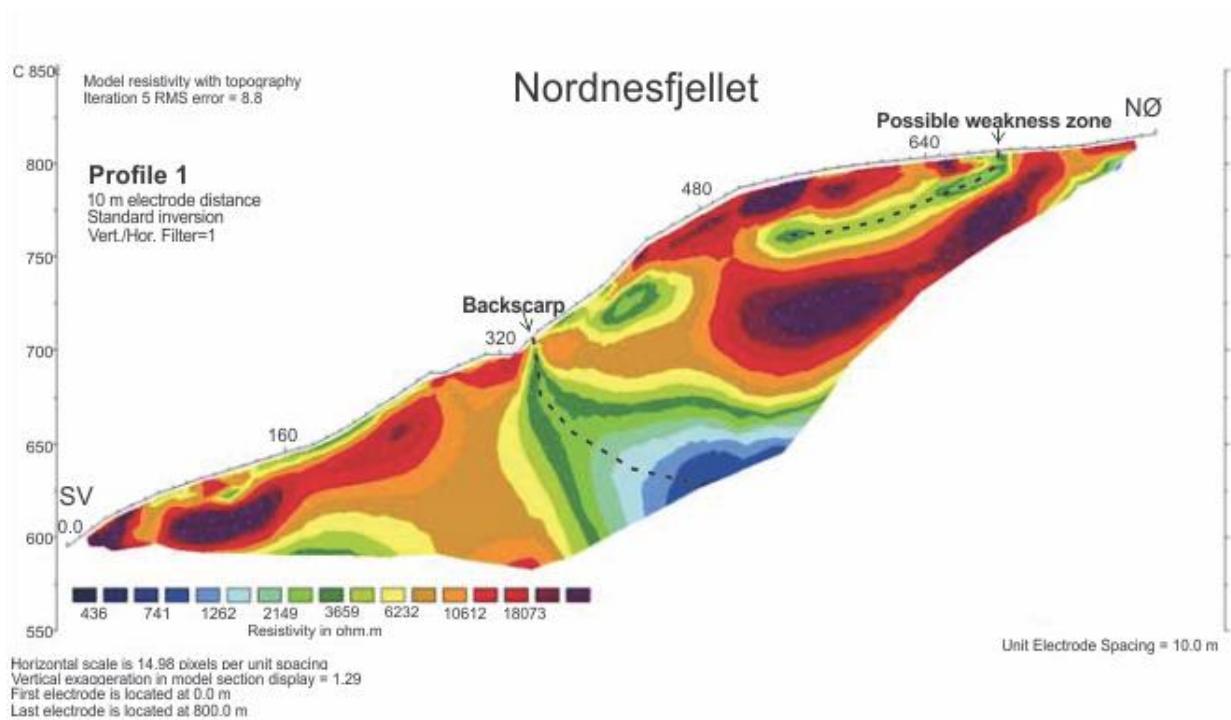


*Figure 10: 2D resistivity profile showing resistivity in depth. Blue color resembles high resistivity, red to purple color low resistivity. The backscarp and a possible weakness zone is marked. Location of profile is seen in figure 13. Modified from Tønnesen and Dalsegg (2004)*
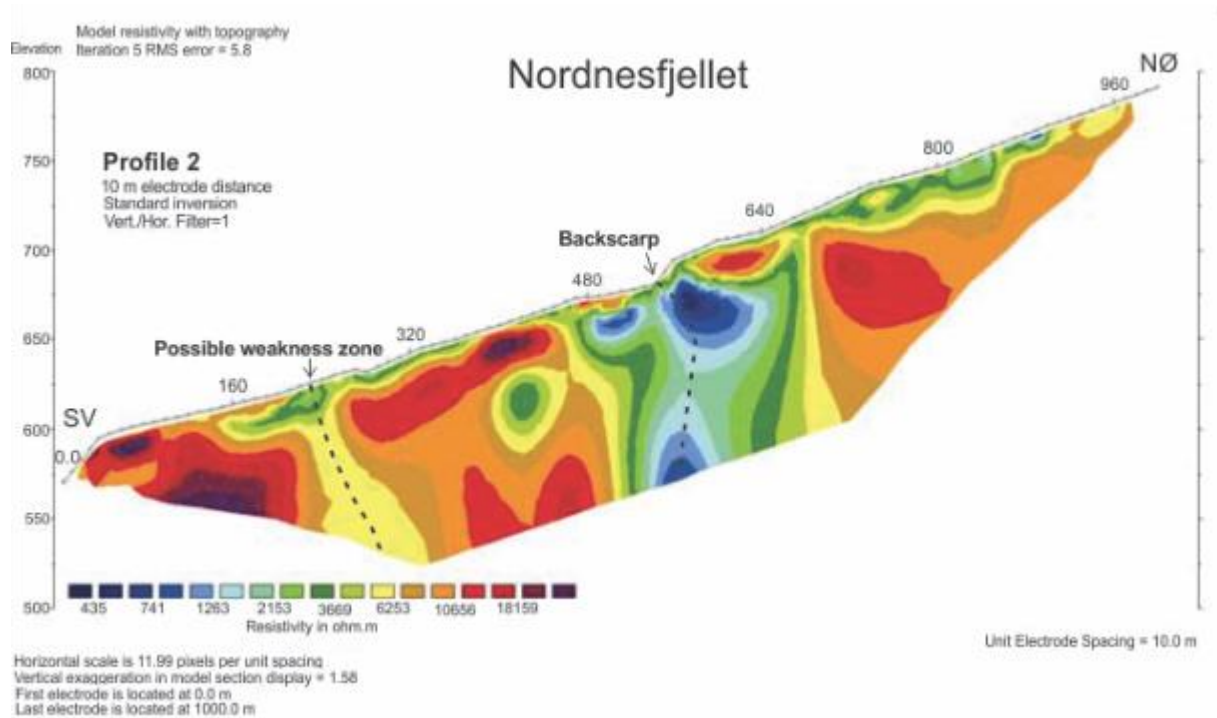
*Figure 11: 2D resistivity profile showing resistivity in depth. Blue color resembles high resistivity, red to purple color low resistivity. The backscarp and a possible weakness zone is marked. Location of profile is seen in figure 13. Modified from Tønnesen and Dalsegg (2004).*
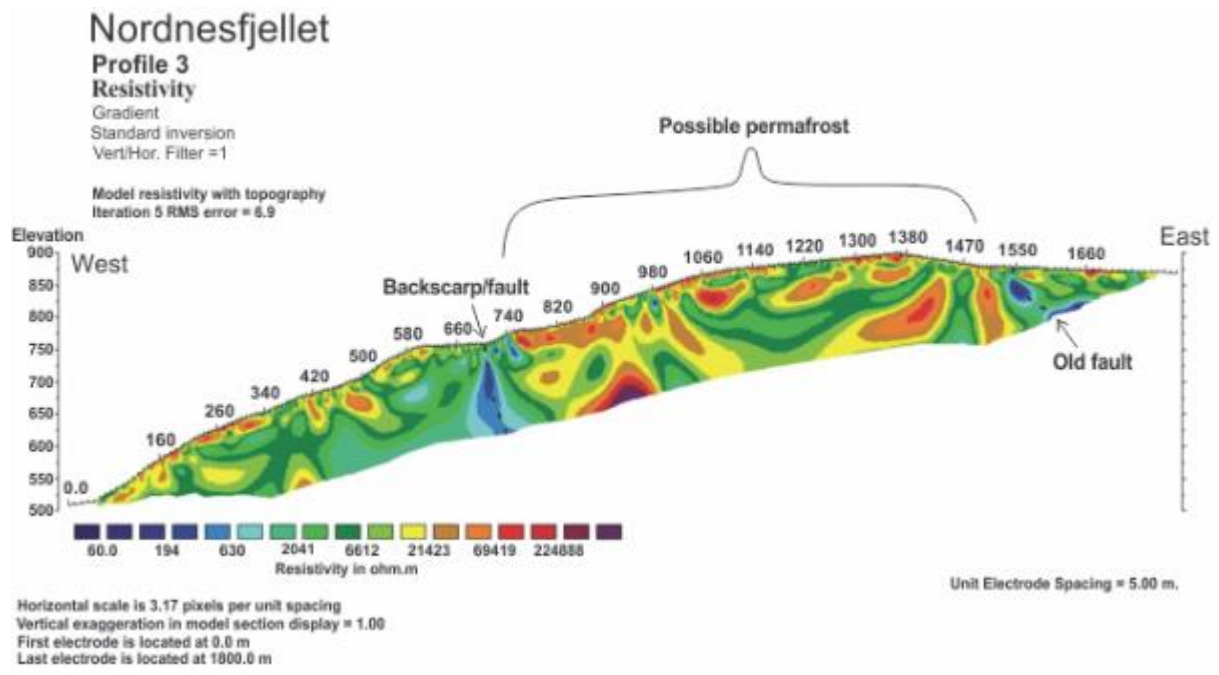


*Figure 12: 2D resistivity profile showing resistivity in depth. Blue color resembles high resistivity, red to purple color resembles low resistivity. The backscarp, old fault and possible pockets of permafrost is marked. Location of profile is seen in figure 13. Modified from Rønning et al. (2008).*

Geo-radar measurements revealed a zone of cupped and shallow fractures/shear zones below blocks NE of the main weakness zone seen in resistivity profile 1 (Tønnesen & Dalsegg, 2004). This zone has a gentle dip towards west and it could be an indication of very slow movement. West and southwest of the main weakness zones in each profiles, geo-radar measurements indicates several sub-horizontal reflectors that could indicate crushed/fractured zones or layering (Tønnesen & Dalsegg, 2004). Heavily crushed rock down to 50 m, and moderately crushed rock down to 150 m below surface, measured normal to the terrain (Rønning et al., 2008).

Tønnesen and Dalsegg (2004) could not find any reliable evidence that permafrost is to be found in the URS, while Rønning et al. (2008) possibly found pockets of permafrost to the SE of the NE-SW striking fault outside of the URS (figure 12). High resistivity values inside the URS have been interpreted as drained rock masses close to the surface (Rønning et al., 2008). Because of the steep and chaotic terrain no measurements were done in the lower part of the slope, and as a consequence no lower boundary was found in the unstable area (Rønning et al., 2008).
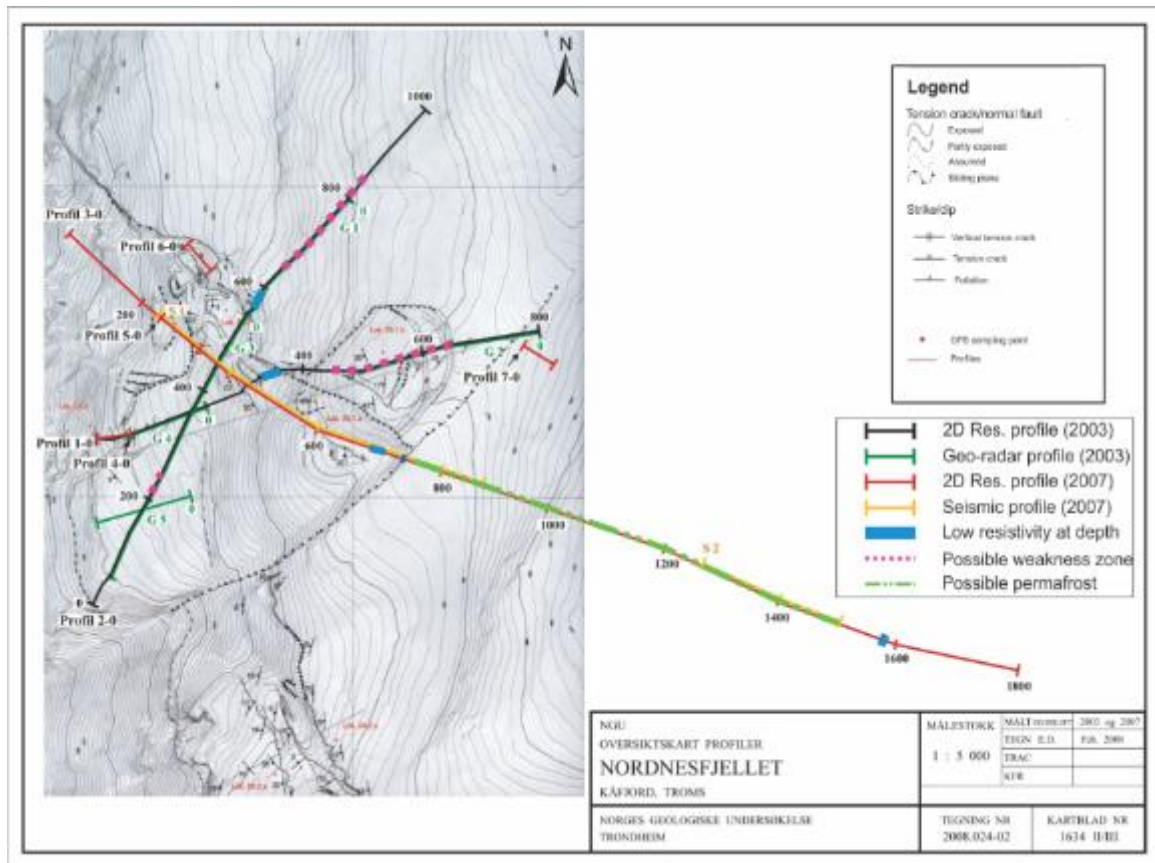
*Figure 13: Geophysical investigations done at Nordnesfjellet in 2003 and 2007. Low resistivity at depth (blue boxes) is referred as weakness zone and backscarp. Modified from (Rønning et al., 2008).*

## 2.4 Boreholes

Three cores have been drilled at Jettan (figure 14). The aim was to get a greater understanding of how the unstable area is moving and constrained by looking at bedrock type, fracture frequency and zones where movement could or is happening. The cores were logged and an optical televiewer (OTV) was used to image the boreholes from the inside. Rock quality was later tested for cores taken from borehole 1 and borehole 3.

*Figure 14: Location of boreholes at Jettan (Kartverket, 2016).*

### 2.4.1 Borehole 1

Borehole number 1 was drilled at 607 m asl to 198.8 m below ground level (bgl). It consists of banded garniferous mica schist, mica schist with layers of marble and marble with layers of mica schist (figure 16) (Ganerød, 2013). Ganerød (2013) logged a 25 cm thick zone of carbonate breccia with clasts of mica schist, and possibly clay at 45.2 – 45.5 m below ground level (bgl),and attributed this as the main zone of displacement and as possibly a fault plain (figure 15). This correlated well with the OTV images, from which Elvebakk (2013) concluded that the area of poorest stability was at 46 m bgl. The fault plain has an estimated dip of 65-70°, and the top fracture of the fault plane dips around 40°, resulting in a dip of the sliding plane between 40° and 70° (Ganerød, 2013). From Elvebakk (2013) this fault plane was estimated to have a dip of 40 degrees towards NW.
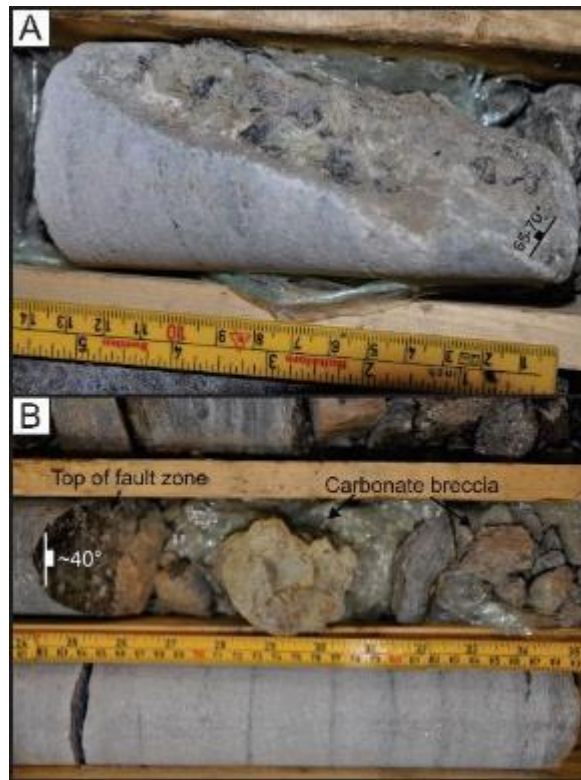
*Figure 15: Old fault plain at 45.5 m bgl with a dip between 65° – 70° seen as the main zone of displacement containing a layer of breccia. B) Fracture at the top of the fault zone with a dip around 40°. The fault zone contains carbonate breccia and possibly clay. Modified from Ganerød (2013).*

Deeper zones with crushed material were also found at 156.6 – 157.7 m, and a zone with crushed rock and possibility clay at 148.5 – 152 m deep (Elvebakk, 2013; Ganerød, 2013). The foliation dips towards west at 0 – 45 m bgl with an dip angle between 10° - 20° (Elvebakk, 2013). Around 45 m bgl the dip angle measures up to 45° - 60° with a varying dip direction. Below 60 m bgl, the foliation dipping direction varies and has a dip angle from 0° - 15° (Elvebakk, 2013). High fracture frequency was found at 26 - 32 m, 36 - 40 m, 58 - 64 m, 140 - 160 m, 165 - 168 m, 176 - 182 m, and 193 - 198 m (figure 16). Poor to medium quality rock regarding Q-value (rock quality) was found in the intervals 15 – 20 m, 26 – 30 m, 36 – 46 m, 58 – 64 m, 105 – 125 m, and 148 – 181 m. In these intervals the RQD (Rock Quality Designation) values were also low, implying that the low Q-values are due to the high density of fractures (Nystad, 2014). Groundwater was not observed in the borehole (Nystad, 2014).

*Figure 16: Borehole 1. A) Fracture frequency. B) Dip direction and dip angle for foliation (black) and fractures (red). C) Lithologies and crushed zones (Elvebakk, 2013; Ganerød, 2013; Nystad, 2014).*

## 2.4.2 Borehole 2

Borehole number 2 was drilled 654 m asl to a depth of 98.08 m bgl. Borehole 2 has the same banded appearance of lithologies as in borehole 1 (figure 18). Two zones of heavily crushed and deformed rock stand out at 46.5 – 46.52 m and 53 – 53.11 m (figure 17). The zones consist of clay and have a foliation varying from sub-horizontal to sub-vertical (Ganerød, 2014). The zone that is marking the upper limit has a dip on 45°.
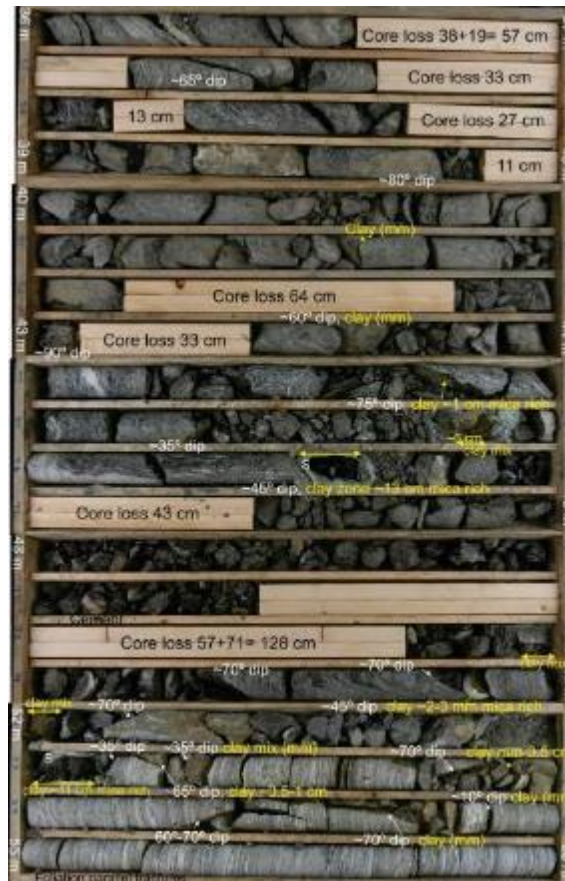
*Figure 17: Main zone of crushed rock from 36-53 meter, including highly fractured and crushed rock with clay and core loss. Modified from Ganerød (2014).*

In addition, finely crushed rock was found at 89.5 – 91 m with cohesive breccia and cohesive gouge, interpreted to be an reactivated inherited fault (Ganerød, 2014). Results from the OTV displayed a foliation dipping SW for the whole borehole and a dip angle between $10° – 25°$. Except from 25 to 55 m bgl the foliation dips further to the west and has a dip ranging from $55°$ - $75°$ (Elvebakk, 2014). Highest fracture frequency is found at $40 – 42$ m bgl, at $32 – 42$ m bgl the fractures are dipping $45°$ - $75°$ towards SW, and between $59 – 80$ m bgl fractures are dipping between $15° – 75°$ towards WNW (Elvebakk, 2014). Groundwater is observed at 90 m bgl, and during the drilling water was drained out at two locations (figure 18) (Nystad, 2014). Drainage of water during drilling is likely a consequence of highly fractured rock, in the borehole these observations correlate well (figure 18)
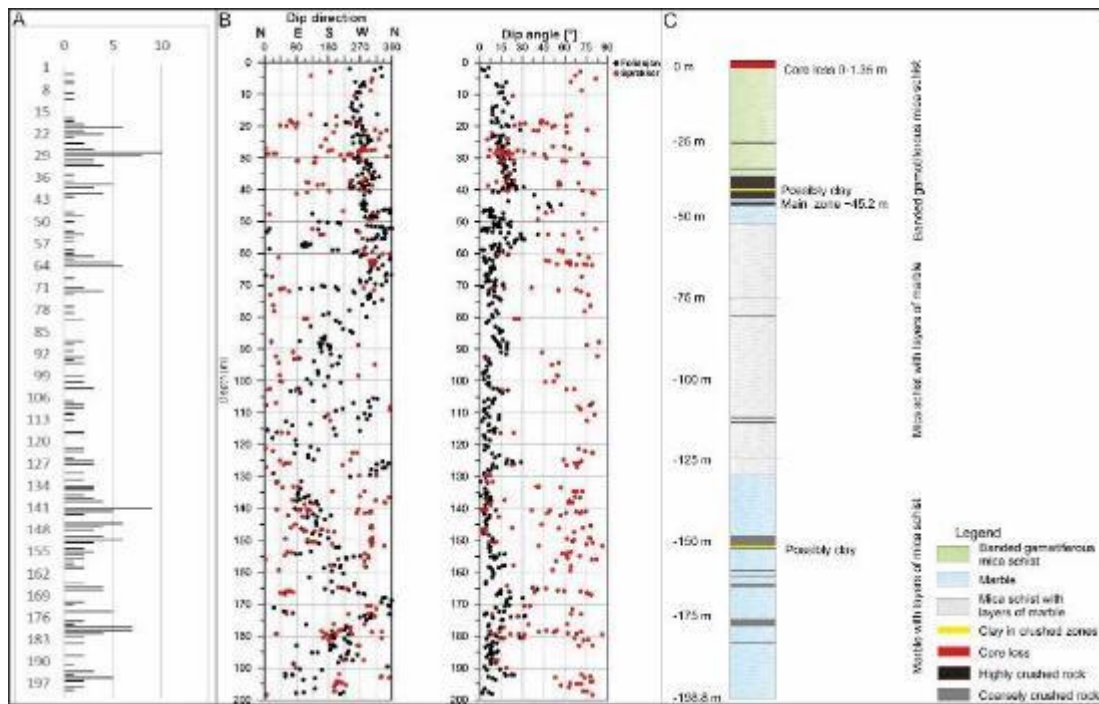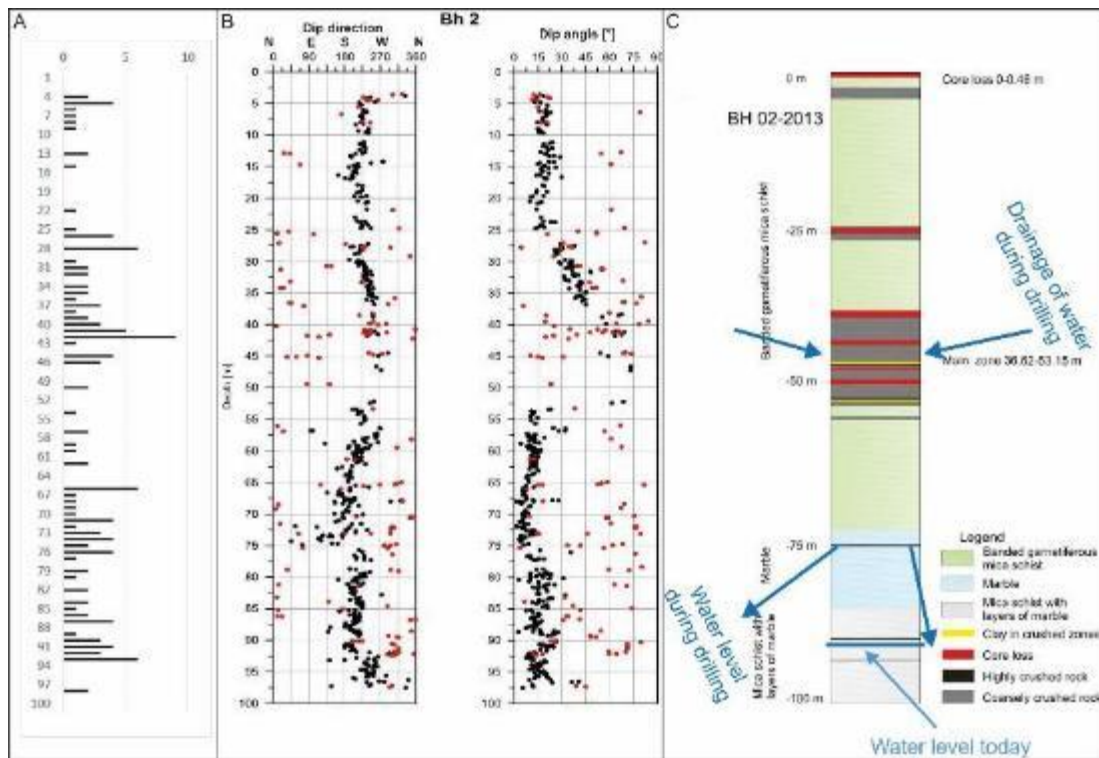
*Figure 18: Borehole 2. A) Fracture frequency. B) Dip direction and dip angle for foliation (black) and fractures (red). C) Lithologies and crushed zones logged with water level during drilling (Elvebakk, 2013; Ganerød, 2013; Nystad, 2014).*

### 2.4.3 Borehole 3

Borehole 3 was drilled at 522 m asl to a depth of 100.94 m bgl including the same lithologies as found in borehole 1 and 2 (figure 20). Borehole logging by Ganerød (2014) concludes the main zone of deformation to be at 42.3 – 46 m (figure 19). Besides this zone, fault rock at 72.0-72.3 m and fine crushed rock at 80.8 – 81.30 m was found. The foliation in the borehole varies from dipping towards south and east from 0 to 45 m bgl, from 45 m to 70 m bgl towards east, below 70 m bgl towards west and at the bottom towards north. The dip angle is approximately around 15° (Elvebakk, 2014). Fractured zones were found at 24 – 45 m, 75 – 80 m and 80 – 81 m. Joint-parallel foliation was found in the zone from 75 – 80 m with a dip towards west (Elvebakk, 2014).

*Figure 19: Main zone of crushed rock in borehole 3 at 42.3 to 46 m. Core loss is seen in the start of the zone and the rest is dominated by crushed rock. Modified by Ganerød (2014).*

Poor rock quality regarding Q-value was found at 24 – 46m, poor to middle quality at 59 – 60 m and 75 – 83 m. These low Q-values correlates well with RQD values, implying that the low Q-values are an effect of highly fractured zones (Nystad, 2014). Groundwater was observed at 90 m bgl in the borehole (Nystad, 2014).
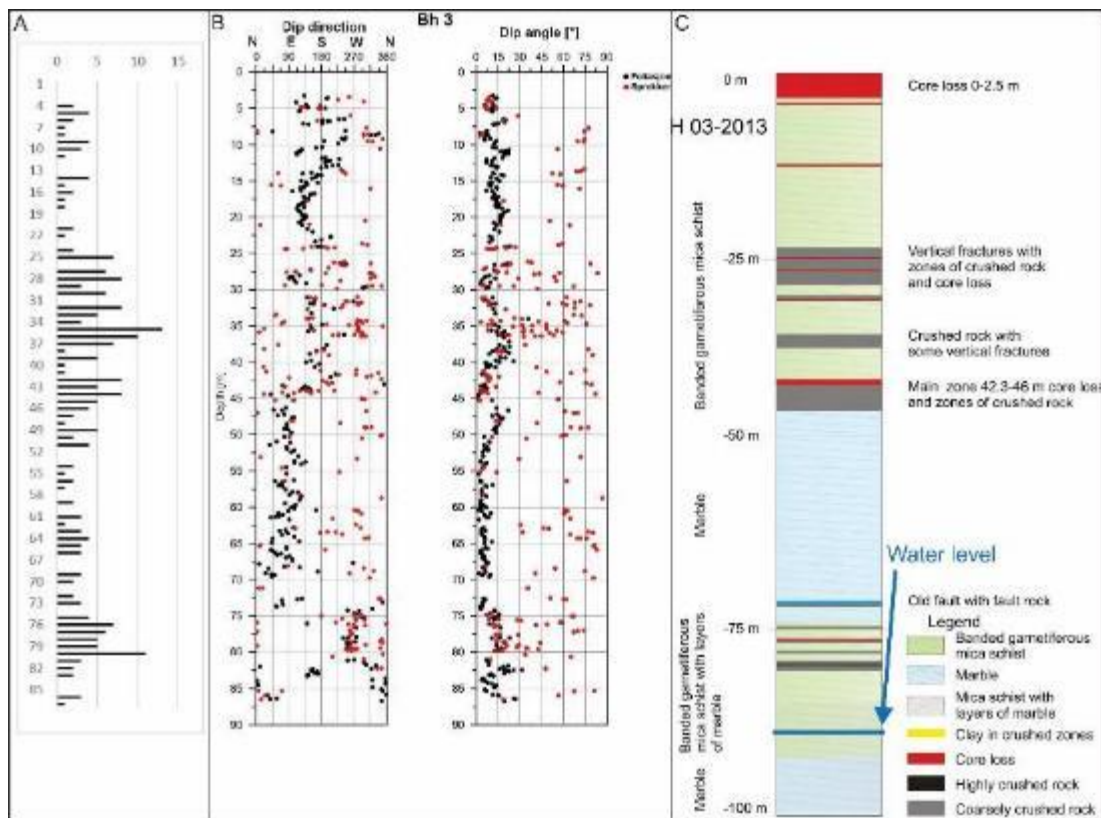
### 2.4.4 DMS-column

In borehole 1 a DMS-column (Differential Monitoring of Stability) was installed January 2013. The DMS-column registries movement, temperature and water pressure. Nystad (2014) looked at results from the period 01.05.2013 to 06.02.2014, and found that the highest movement rates are at 45m depth with a total movement of 6-7 mm for the period analyzed (figure 21). In this zone orientation of the movement is towards west (260°). Below the zone total movement is on 3-4 mm towards east, and above the zone total movement is on 5-6 mm.
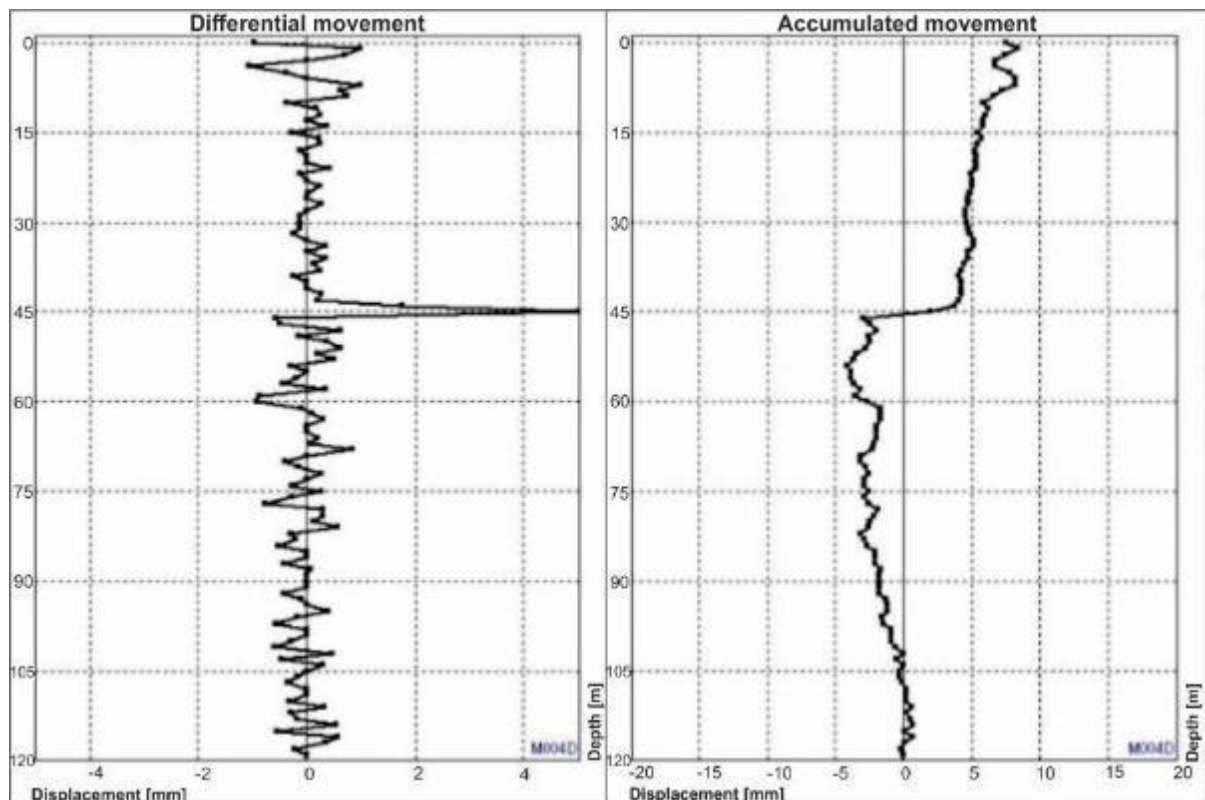


*Figure 21: Left: Differential movement in the DMS-column towards 260°. Right: Accumulated movement in the DMS-column towards 260°. Modified from Nystad (2014)*

## 2.5 Seasonal deformation at Jettan

Studies show that it is common to find correlations between movement and weather. Increased deformation is usually experienced during snowmelt in the spring, followed by low to almost no deformation in the autumn and winter (Blikra & Christiansen, 2014). At Jettan an increased deformation is seen in the spring due to snowmelt, but unlike other URSs Jettan displays

additional movement throughout the autumn (Blikra & Christiansen, 2014). The lower boundary for permafrost at the Nordnesfjellet peninsula lies between 600 – 700 m asl, therefore Jettan lies partly inside the area where permafrost could occur (Christiansen et al., 2010).
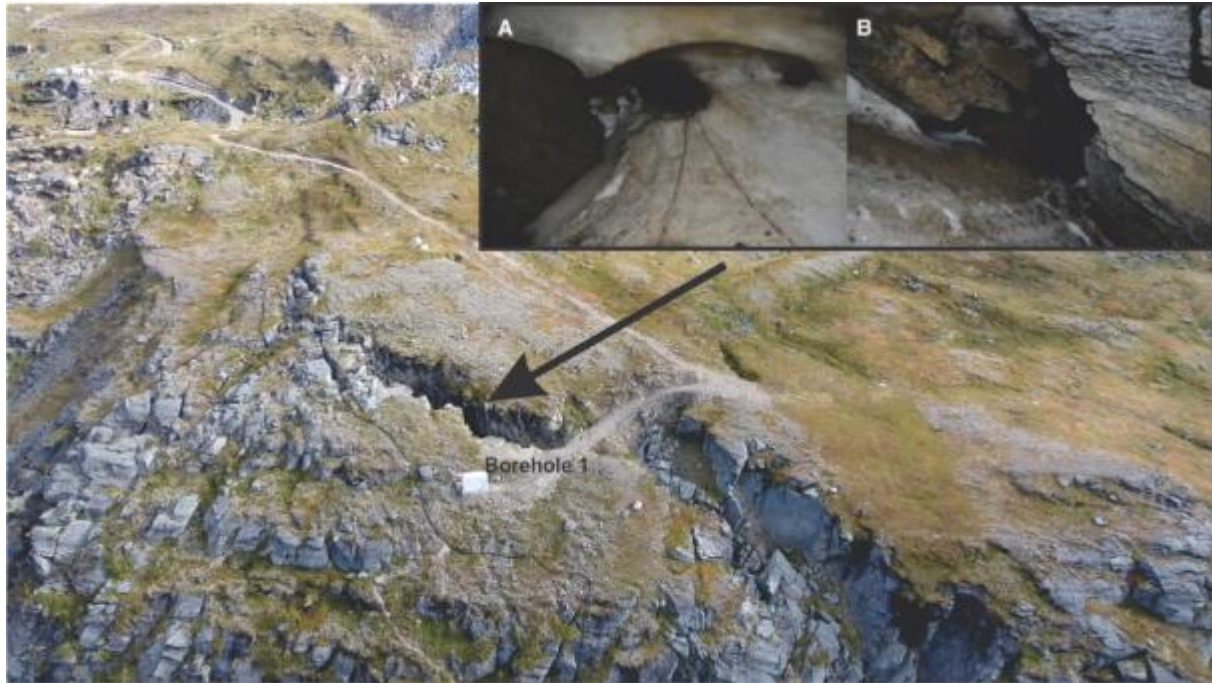


*Figure 22: Large surface fracture containing ice. A: Ice at 20-25 m depth with meltwater channels. B: Ice continuing down into a channel (Blikra & Christiansen, 2014).*

Blikra and Christiansen (2014) investigated how permafrost controls the deformation at Jettan. The study looked at deformation in the bedrock, a three years analysis of the local meteorology, investigations of the back scarp, and temperatures under the snow cover and in the bedrock. The geometry of the topography, the accumulation of snow and the complex joint patterns at Jettan creates a unique setting that leads to localized permafrost at or below the permafrost limit. In one of the large surface fractures (figure 22) ice was found at the depth of 20-25 m in the autumn, indicating that local permafrost is occurring (Blikra & Christiansen, 2014). The study revealed big seasonal variation in deformation; acceleration in movement from May,

reduction of movement in December and even a greater reduction of deformation again in February (figure 23).
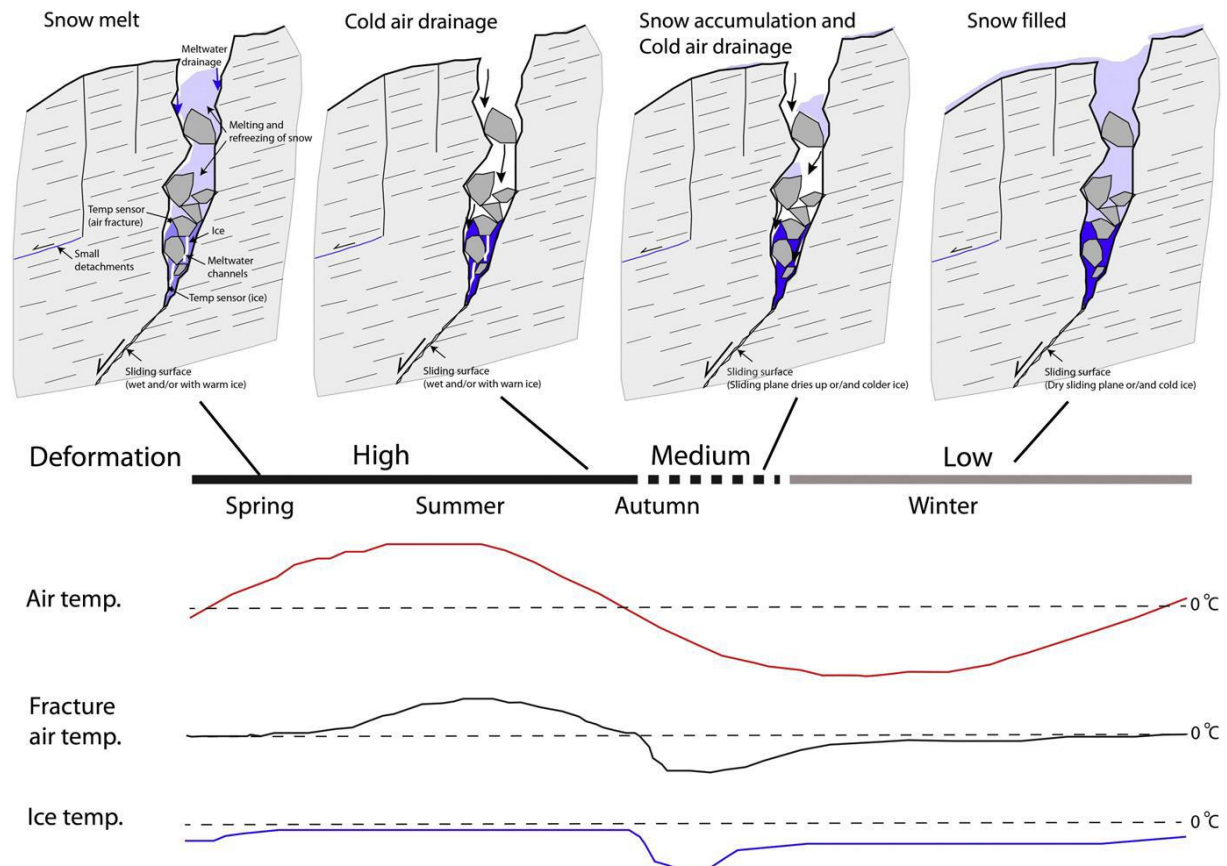


*Figure 23: Permafrost controlled rockslide model. Annual deformation displayed with air-, fracture- and ice-temperature in the lower part of the backscarp (Blikra & Christiansen, 2014).*

From the study by Nordvik et al. (2010) where they looked at ten crackmeters time series and three laser time series, there was no correlation between deformation and snowmelt in the spring time. This does not fit well with a later contribution from Blikra and Christiansen (2014) where the highest deformation rates were found in the spring and summer (melting period). Results from Nordvik et al. (2010) rather showed that the deformation was affected by the temperature, directly on instruments or heating/cooling of bedrock, indirectly by melting and formation of ice. A seasonal pattern displaying deformation with largest rates in the autumn, interpreted as an effect of freezing of water in the cracks leading to an expansion of the cracks (Nordvik et al., 2010).

In the following a description of the different seasonal periods of deformation found by Blikra and Christiansen (2014) will be presented.

## 2.5.1  Spring to autumn, high deformation

Deformation increases when the snow melts in the spring, but a deceleration is not seen when the snowmelt is heavily reduced or has stopped. This indicates an additional driving mechanism than water pressure alone. When the daily air temperature becomes positive, usually around middle of May, a sudden increase in deformation is recorded. A temperature above zero degrees leads to melting of the snow cover. Meltwater infiltrates fractures and raises the ice temperature from -0.5°C to just below 0°C. As a result, the ice in the fractures melts, sliding planes are saturated and the shear strength is reduced leading to high deformation. The warmest periods in summer records temperatures up to 8-10°C in the upper part of the fracture. Little or no insolation from the sun leads to low temperatures in the deeper part of the fracture, and a consequence is that the ice survives the summer period.

Usually in October, the air temperature outside of the fracture become remarkably colder compared to the temperature inside the fracture. The cold dense air sinks into the fracture replacing the warm air, leading to less deformation by lowering the ice temperature.

## 2.5.2  Late autumn to early winter, medium deformation

Accumulation of cold air in the fractures causes a gradual reduction of deformation during a 1 to 2-month period from early winter. This accumulation of cold air increases the shear strength of the ice, and the reduction in melt water leads to drier sliding surfaces. When and how long this medium deformation period is happening depends on the extent of the snow accumulation in the fracture and the characteristics of the cold-air drainage.

When the snow cover occurs early, closing the fracture, cold-air-accumulation in the lower part of the fracture is stopped. The ice temperature reduction causes a lowering of the shear strength on the sliding planes, allowing a continued reduced medium deformation. When the snow cover arrives late, cold-air-accumulation lasts for a longer period reducing the ice temperature and deformation rate. The increased shear strength in the fracture could lead to a deformation rate of almost zero.

### 2.5.3 Early winter to spring, low deformation

This period lasts for around 3 to 5 months and is characterized by a stable minimum deformation. The snow covering the main fracture prevents influence from the environment outside, making a stable temperature just below 0°C inside the fracture. In the beginning of to the middle of May, when the air temperature outside of the fracture goes above 0°C the snow cover melts and the cycle restarts.

## 2.6 Mass-wasting activity in the past

A thesis by Hegstad (2014) reconstructs the local post-glacial mass-transport in Lyngenfjorden by looking at five sedimentary cores (figure 24), swath bathymetry and high-resolution seismic data. From the data Hegstad (2014) found several different mass-transport deposits (MTDs) in the fjord adjacent to the Jettan runout zone. The MTDs are often overlying glaciomarine sediments. This suggests that the complexes formed after the last deglaciation (~10,800 cal. years BP). Above one of the MTDs, a turbidity deposit dated to 3026-2930 cal. years BP interrupts a post-glacial hemipelagic package of sediments (erosive boundary). The deposit is found beneath Indre Nordnes URS (2.4 km south of Jettan) and is therefore linked to a rock avalanche deposit found beneath Indre Nordnes. This rock avalanche have entered the fjord, initiated a turbidity current in the unstable glacial sediments which has eroded the seabed and made the boundary found the core (Hegstad, 2014).
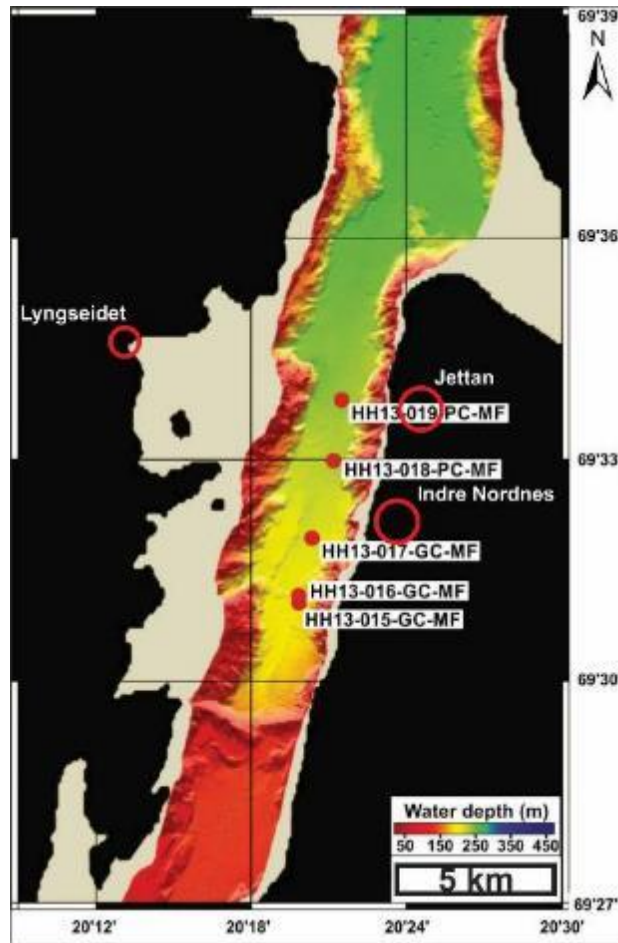
*Figure 24: Locations of the different cores in the Lyngenfjord indicated with red circles. Core number 19 is the northern most core (HH13-019-PC-MF). Jettan, Indre Nordnes and Lyngseidet is marked with red open circles. Modified from Hegstad (2014).*

Core number 19 is located close to the run-out area of the Jettan URS (figure 24). The core did not consist of any rock avalanche deposits, but three units deposited from turbidity flow (figure 25) (Hegstad, 2014). The lowermost unit, contained benthic foraminifera dated to 10,321 cal. years BP just below the upper erosional boundary to the turbidity unit above (Hegstad, 2014). The unit above gives an age which falls inside of the Skibotn event (10,393 – 10,316 cal. years BP). The turbidity current deposits could be a consequence of a rock avalanche from Jettan, seen in comparison to what found beneath Indre Nordnes. However Hegstad (2014) concluded that there has probably not been any large rock avalanches that have reached the fjord since the last deglaciation.
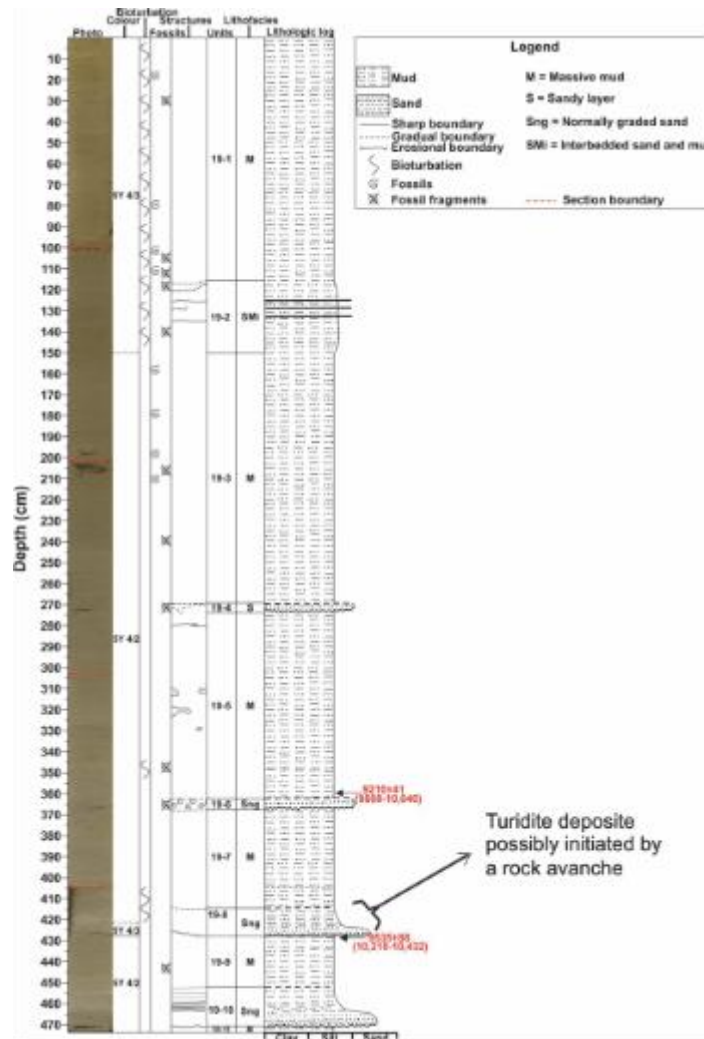
*Figure 25: Lithological log of core HH13-019-PC-MF displaying core photo, occurrence of bioturbation and fossils, Munsell color codes and structures. Units, sub-units and lithofacies are indicated. The dated levels are indicated with arrows (14C years are on top and calibrated years BP in brackets). Modified from Hegstad (2014).*

## 2.7 Movement initiation

Jettan was uncapped from the glacier somewhere between Younger Dryas (ca. 11-10 ka) and the Ørnes event (9.9 – 9.8 ka ± 150 years) (Corner, 1980). At Jettan a small moraine ridge is located at 620 to 640 m asl which has been correlated to the Younger Dryas (Blikra & Christiansen, 2014). The moraine ridge has collapsed into a big fracture, a relationship indicating that the URS is postglacial, and after the Younger Dryas (Blikra & Christiansen, 2014). This big open fracture is located in the upper part of the area 2 (southern area, figure 6 and 22) close to borehole 1.

Cosmogenic surface exposure dating has been done in the upper most part of the NE-SW striking backscarp, resulting in an age of 6520 ± 335 years BP (Blikra & Christiansen, 2014). This indicates that movement along the fault was reactivated 6000 – 7000 years ago (Blikra & Christiansen, 2014). From past mass-wasting activity, a turbidite with an age of around the Skibotn event (10,393 – 10,316 cal. years BP) (Hegstad, 2014) was found. This deposit could be in connection with a possible avalanche from Jettan that occurred 10,000 years ago. Hegstad (2014) concluded that no larger avalanches have happened since the last glaciation, and that the mountain side has been relatively stable the last 10,000 cal. years BP, apart from the event correlated to Indre Nordnes. As Hegstad (2014) only investigated the fjord adjacent to Jettan, there could have been smaller events from Jettan, possibly not reaching the fjord.

These evinces suggest that the western part started moving, collapse of moraine, before the upper eastern part, cosmogenic surface exposure dating. No evidence of large rock avalanches after deglaciation is recorded, therefore a more steady movement is suggested to have accrued to today's date with some rock fall activity (Blikra & Christiansen, 2014)

## 2.8  Movement at Jettan

A number of studies have investigated the movement rate and movement direction at Jettan(Blikra et al., 2009; Blikra et al., 2006; Eckerstorfer et al., 2018; Henderson et al., 2007; Nordvik et al., 2010; Skrede, 2013). The most recent study presents 3D surface displacement from interpolated satellite- and ground-based InSAR in connection with structures and geomorphology at the URS (Eriksen et al., 2017a), and interpreted surface displacement using 2D InSAR (Eriksen et al., 2017b). This study will be presented in the following.

Satellite InSAR measures surface displacement by frequently "throwing" microwave electromagnetic energy towards the ground, measuring the distance between the satellite and the ground (Eriksen et al., 2017b). The radar is only sensitive to displacement along the line-of-sight (LOS) to the satellite, and cannot detect displacement orthogonal to the LOS direction (figure 26) (Eriksen et al., 2017b). 2D InSAR data was conducted by using displacement data from overlapping localities of two high-resolution TerraSAR-X datasets gained from ascending and descending orbits (Eriksen et al., 2017b). Maps and cross-sections were made displaying dip angles, magnitude and spatial variation of the surface displacement (Eriksen et al., 2017b).
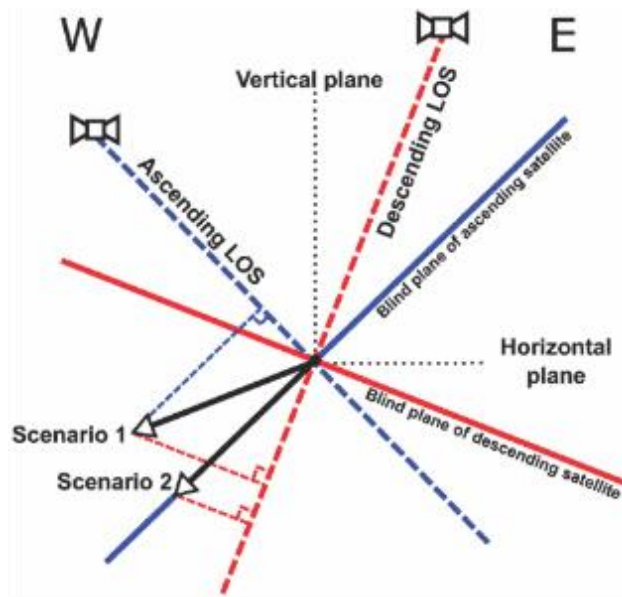
*Figure 26: West-east cross-section showing sensitivity to displacement for InSAR data in ascending and descending satellite orbits. Solid red and blue lines indicate blind planes. Arrows show direction and magnitude of two displacement scenarios having different sensitivity from ascending and descending satellite orbits (Eriksen et al., 2017b).*

Results showed that 2D InSAR compared to GNSS data displayed approximately the same findings for the horizontal and the combined displacement, but with some deviation in the vertical component and displacement dip. From the 2D InSAR data three areas with particularly high movement rates stand out (figure 27).

Area 1 (figure 27) has a movement rate on up to 50 mm a$^{-1}$ and is the most rapidly moving area. The displacement pattern in Area 1 is heterogeneous with a dip varying from into-, out- and down slope (Eriksen et al., 2017b). 3D azimuth vectors strike towards WNW with a shallow plunge angle (Eriksen et al., 2017a). The 3D azimuth could be seen in connection with the gentle foliation (towards west), a complex graben system built up by orthogonal steep fractures trending NW-SE and NE-SW, making ridges, depressions, terraces and scarps (Eriksen et al., 2017a). Eriksen et al. (2017a) suggests a displacement going into the slope in the eastern part (upper most), and a displacement going out-of-the-slope in the western part (lower most) along listric and planar fractures (figure 28).

Area 2 (figure 27) shows a homogeneous displacement pattern with a steeper dip than Area 1, and a movement rate up to 35 mm a$^{-1}$ towards WNW (Eriksen et al., 2017b). A downslope increases in velocity and decreases in plunge (35 mm a$^{-1}$ in the lower part and 25 mm a$^{-1}$ in the upper part), was suggested by Eriksen et al. (2017a) to indicate that displacement is

concentrated on fracture sets parallel to the hillside and that these fracture sets are more continuous than in Area 1. The homogeneous displacement pattern could be seen in connection with uniform NE-SW to NNE-SSW-trending ridges, depressions and scarps. Furthermore the 3D vector data was interpreted to indicate movement on planar and/or listric sliding surfaces giving a step-wise structure and rotation backwards, creating uplift close to the scarps (figure 28) (Eriksen et al., 2017a).

Area 3 (figure 27) has been interpreted to be a rock glacier by Blikra and Christiansen (2014), and the 2D InSAR displacement pattern show a flowing movement supporting the rock glacier theory (Eriksen et al., 2017b).
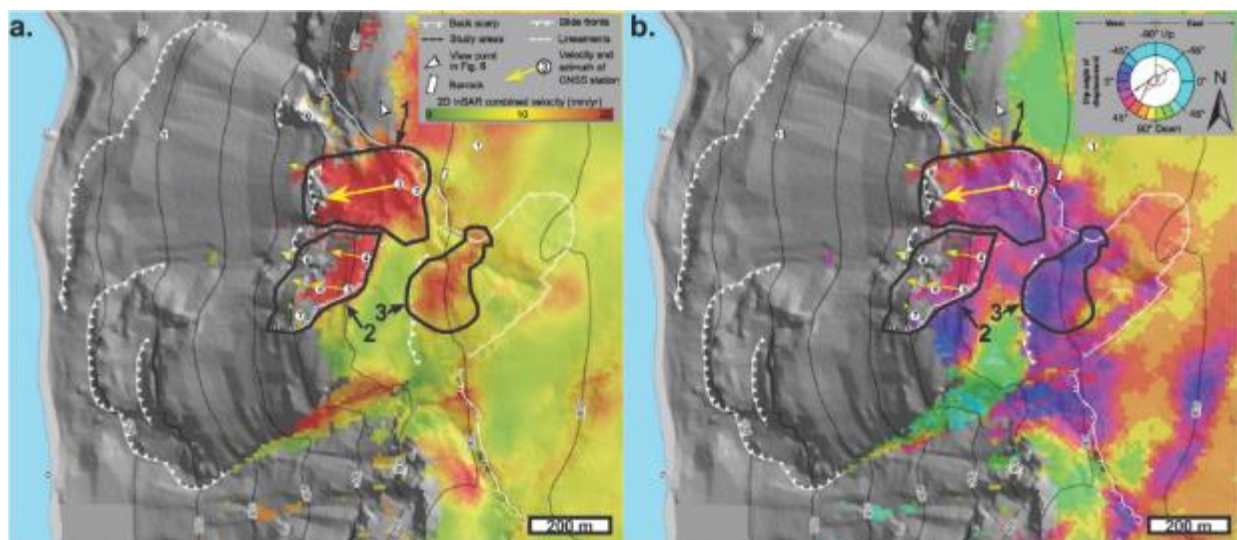


*Figure 27: Mean yearly velocity from 2D InSAR data and GNSS from the Jettan rockslide. The northern (1), southern (2) and upper (3) areas with the most movement are indicated. a) Combined velocity from 2D InSAR data. b) 2D InSAR dip of displacement. Modified from Eriksen et al. (2017b).*
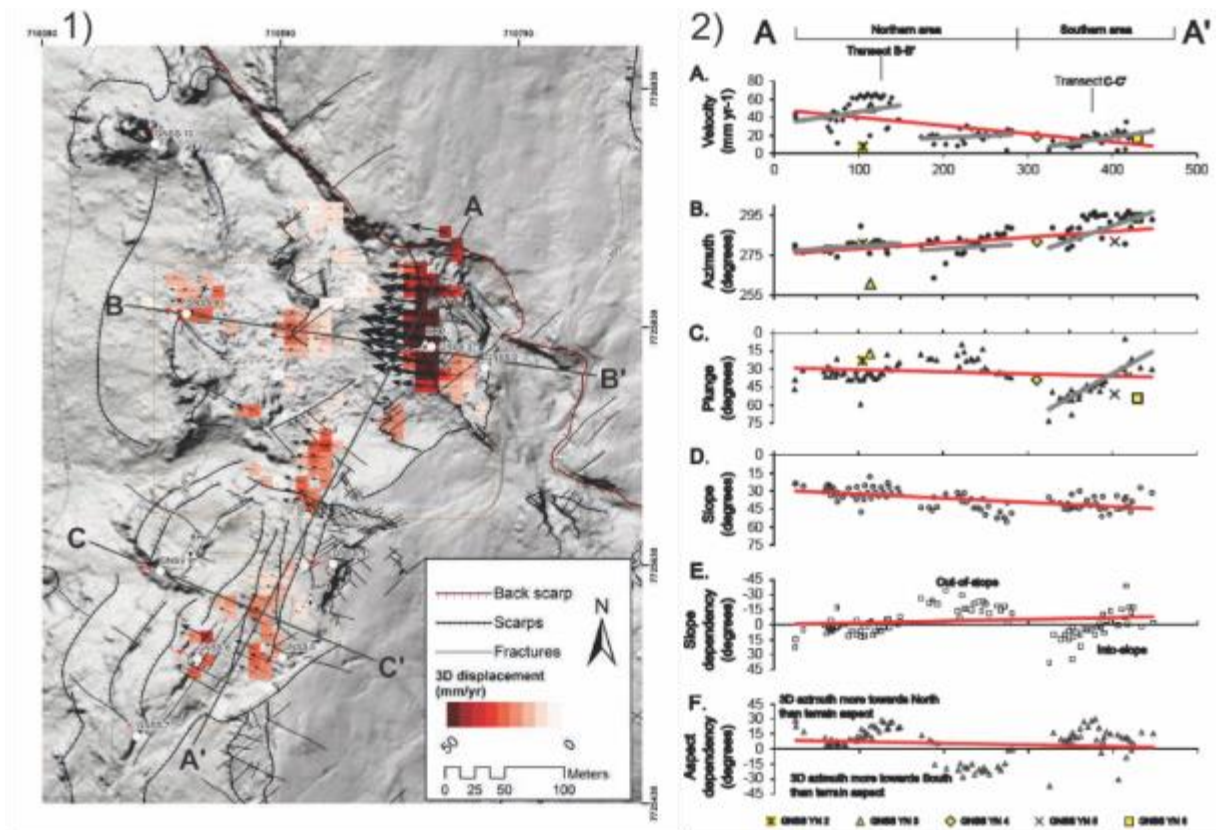
*Figure 28: Displacement vectors and properties of 3D vectors along cross-section A-A'. 1) 3D displacement vectors (black arrows) and GNSS displacement (red arrows), with geological structures and geomorphological elements. 2) Properties of 3D vectors along cross- section A-A'. 1) 3D displacement vectors (black arrows) and GNSS displacement (red arrows), with geological structures and geomorphological elements. 2) Properties of 3D vectors along cross-section A-A' and nearby GNSS stations, including (A) mean yearly velocity, (B) azimuth of displacement, (C) plunge of displacement, (D) slope of topography, (E) plunge of displacement compared to slope giving displacement into- or out-of-slope (slope dependency), and (F) displacement direction towards north or south compared to aspect. Gray lines indicate linear internal trends. Modified from Eriksen et al. (2017a).*

## 2.9 Geological model/cross-section

Several papers and studies have interpreted profiles for different domains at Jettan based on field investigation, boreholes and the geophysics profiles. In the following I will present the geological models made by Nordvik et al. (2010), Nystad (2014) and Eriksen et al. (2017a) to show different interpretations.

Nordvik et al. (2010) did analysis of seasonal displacements at Jettan. Crackmeter data indicated areas with extension and areas with contraction inside the URS (figure 29). The extension zones were assumed to be due to fracture evolution, where single blocks in a larger graben structure back-rotate towards the main crack. A possible geometry was suggested to be a stepped sliding surface. Deformation ongoing in the autumn was seen as frost and permafrost

processes and indicating that there are frozen parts in the fractures (figure 29). This was later confirmed, see chapter 2.4.
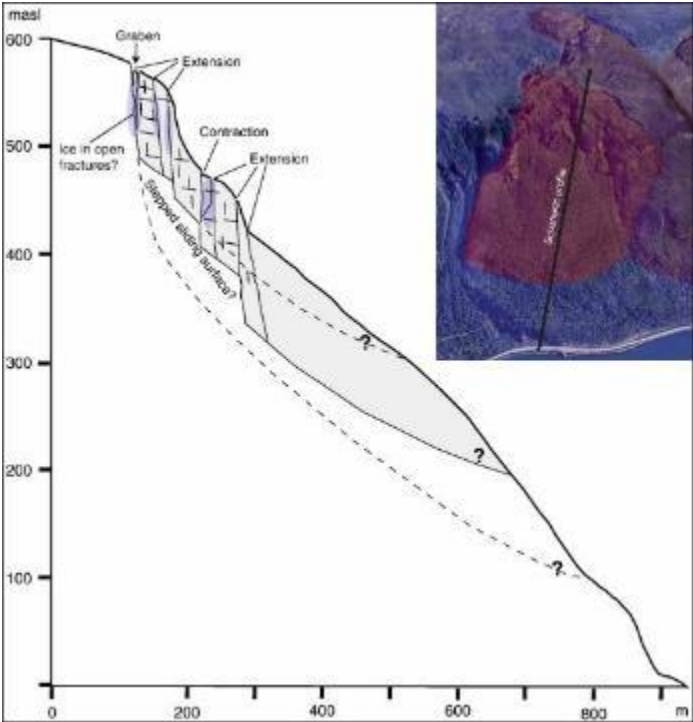


*Figure 29: Cross-section indicating possible extension and contraction zones in the slope, locations where there could be ice in fractures and possible sliding surfaces. Modified from Nordvik et al. (2010).*

Nystad (2014) made three profiles at Jettan (figure 30). The main goal was to locate where the sliding surfaces for the URS are, and then later make an estimate of the possible volumes for avalanche scenarios. In the profile's fractures, boreholes, groundwater and sliding surfaces are marked, as well the orientation and position of backscarps.
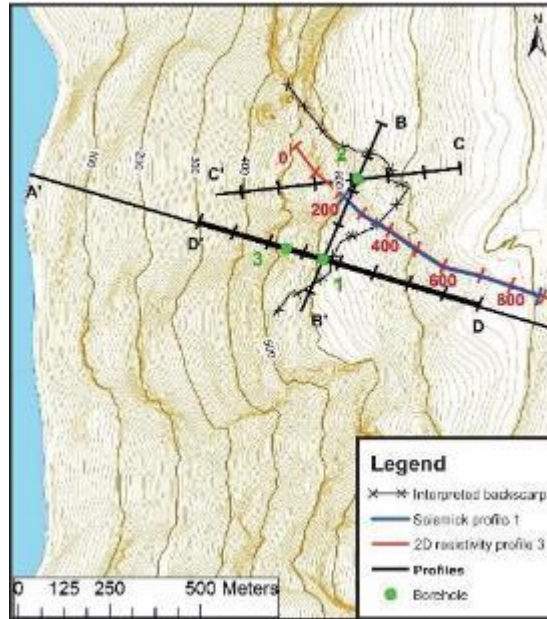
*Figure 30: Position of the different profiles from Nystad (2014)*

Profile CC' is the northern most profile oriented WSW, and traces through borehole 2. The groundwater level was found to be at 91 m bgl in borehole 2 (figure 31). Another finding was a hanging groundwater table from 46-49 m bgl to 75 m bgl where the water was drained during drilling. Sliding planes were interpreted from borehole data which led to the conclusion of three main sliding surfaces that daylight in the slope. These zones are at 25-27 m, 36-53m and 75 m bgl, and contained crushed and fractured rock. Another zone with crushed rock at 89.5-90.7 m bgl, had joints dipping between 40-70° and was interpreted not to daylight in the slope. The back fracture had dip too steep to daylight in the slope and was therefore interpreted to be a deep going structure. Movement data was used as a tool to determine where in the slope the different sliding planes daylight.
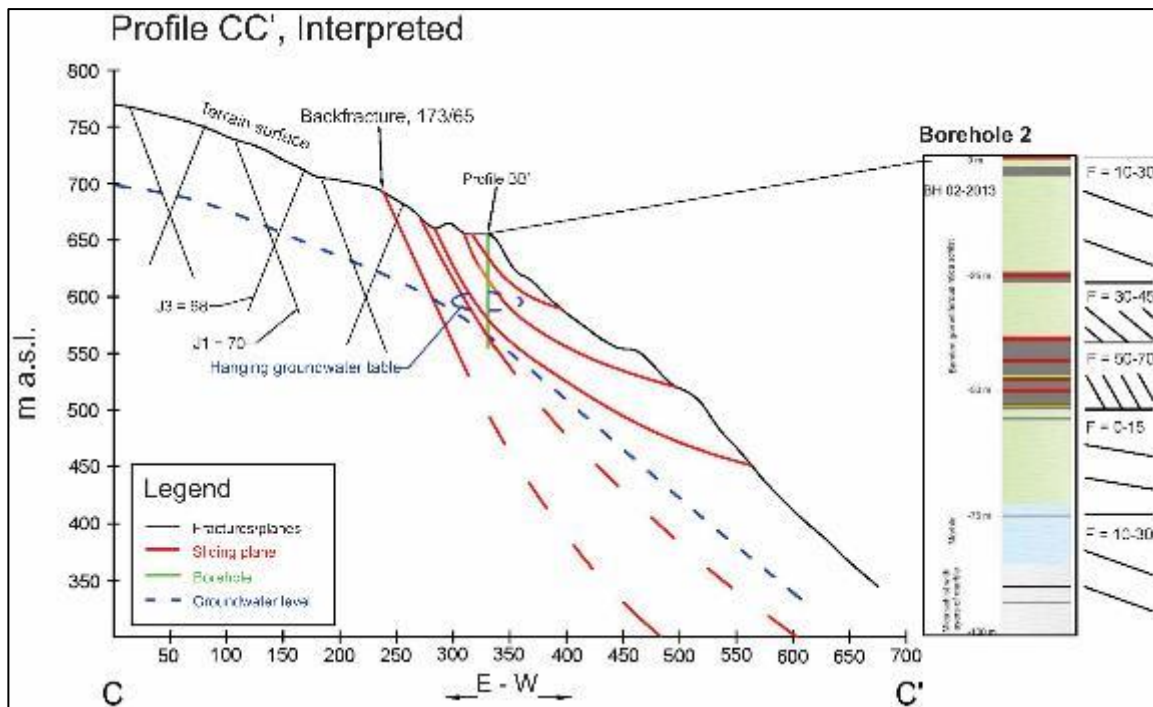
*Figure 31: Profile CC. Modified from Nystad (2014).*

Profile DD' is located in the middle of the Jettan URS oriented WNW, and traces through borehole 1 and 3. In borehole 1 no groundwater has been detected and therefore the water found in borehole 3 has been interpreted as a hanging groundwater table (figure 32). The main zones of crushed and fractured rock were found at 45 m depth in borehole 1. This zone is where the highest movement rates in the DMS-column were measured and is therefore considered the main sliding plane. In borehole 1 a crushed zone interpreted as a fault was found at around 150 m bgl, marked in the profile as "fault?" (figure 32). Borehole 3 contains two main crushed zones at 25-30 m bgl and at 45 m bgl. The sliding plane at 45 m bgl has been interpreted as the same as the one found in the DMS-column and is seen as the lowest sliding plane (figure 32). Joints that have been measured in the surface had a steeper dip than what was found in the boreholes, possibly indicating that the joints curve and get less steep at depth. Movement data was used as a tool to determine where in the slope the different sliding planes day lighted.
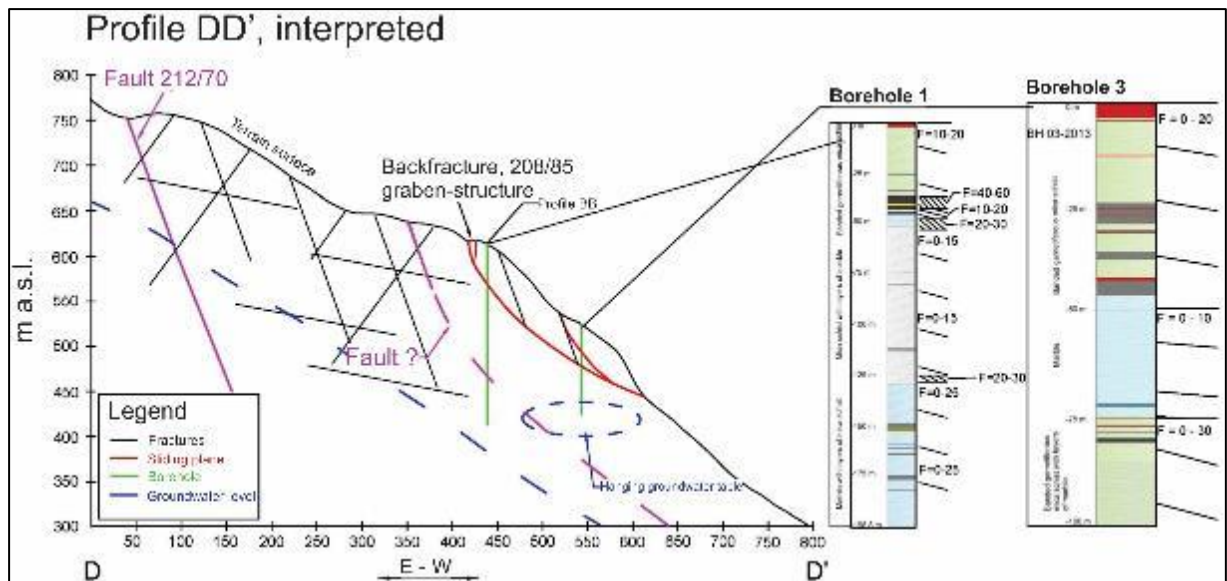
*Figure 32: Profile DD'. Modified from Nystad (2014).*

Eriksen et al. (2017a) produced two geological cross-sections by using data from the DMS column and core logging of boreholes, mapped structures from Skrede (2013), and his own findings from displacement data. Location of the different profiles are shown in figure 28. The findings from the study suggest that the orthogonal NW-SE and NE-SW striking fractures favor a wedge-failure with the foliation or listric fractures as the main sliding surface (figure 33). This structure could lead to inward extension and restricted uplift close to the scarps, and compression in the lower part of the URS as a consequence of masses acting as "support" at the toe.
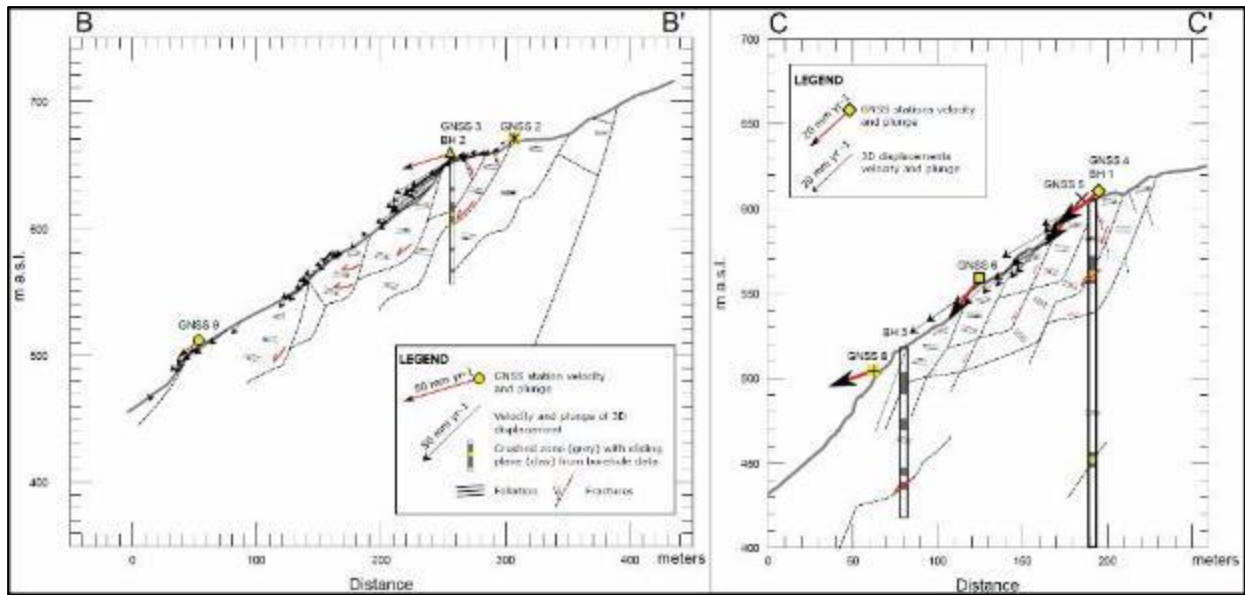
*Figure 33: Profie BB' and CC' from Eriksen et al. (2017a) showing suggestions of different sliding planes, foliation and movement. Modified from Eriksen et al. (2017a).*

## 2.10 Failure scenarios and displacement wave

A study done by Henderson et al. (2007) constructed possible failure scenarios based on geomorphological and structural mapping, yearly GPS measurements, InSAR data, geophysical measurements and continuous monitoring data. They concluded with three possible failure scenarios, respectively scenario 1a and 1b, and scenario 2 (figure 34). Scenario 1 encompasses the fastest moving area at Jettan, and is divided in to two sub-scenarios. 1a had an estimated volume of 7 Mm$^3$, scenario 1b a volume of 4 Mm$^3$ and scenario 2 was a collapse of both scenario 1a and 1b giving a total volume of 11 Mm$^3$ (Henderson & Blikra, 2007).
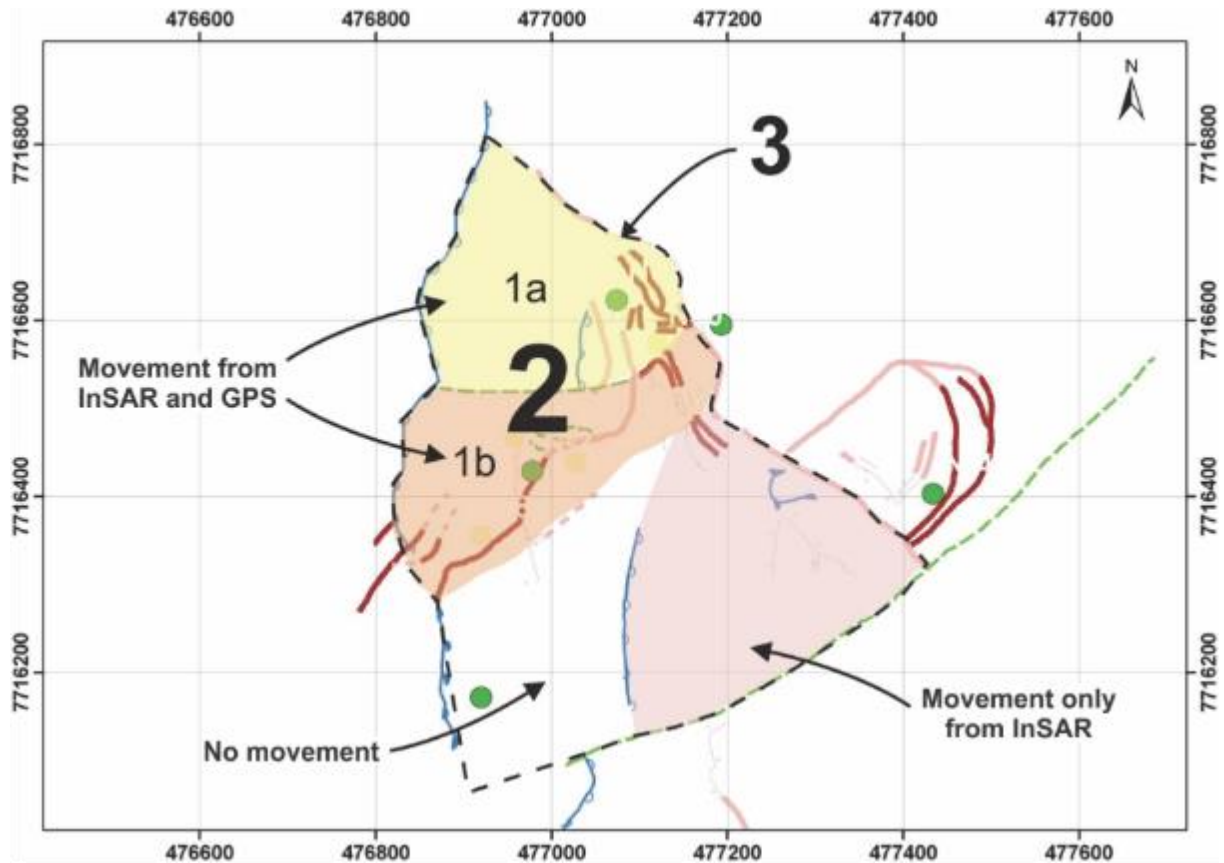
*Figure 34: Failure scenario 1a, 1b and 2 location at Jettan. Modified from Henderson and Blikra (2007).*

Later a rougher estimate was done based on new geophysical estimates showing that the unstable area probably is more than 100 m deep (Rønning et al., 2008). The volume was estimated to be between 12 and 22 $Mm^3$ for scenario 2, and 5-9 $Mm^3$ for scenario 1a, using depths between 70 m and 120 m (figure 35) (Blikra et al., 2009).
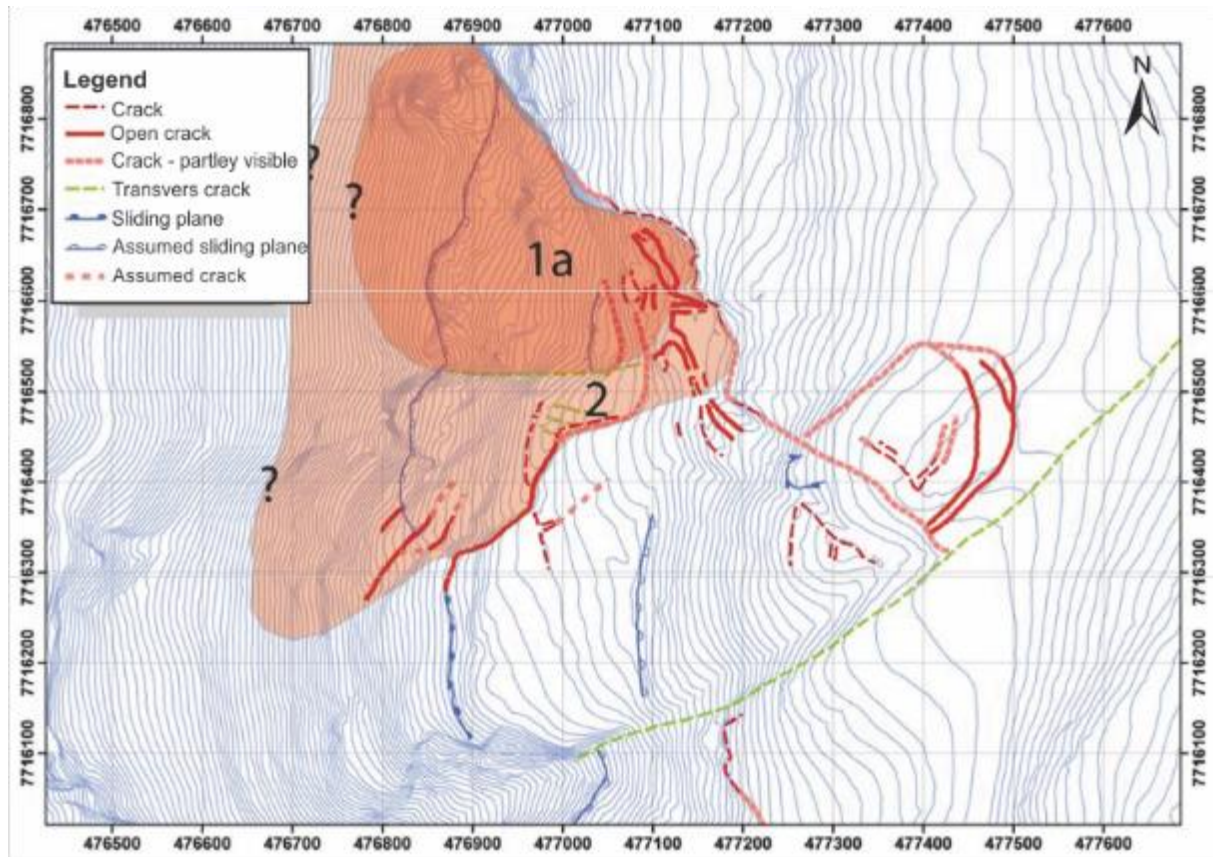
*Figure 35: Map showing the two failure scenarios at Jettan. Scenario 2 includes scenario 1a. Modified from Blikra et al. (2009).*

NGI conducted displacement wave analysis based on potential rock avalanche volumes from several URSs above Lyngenfjord (NGI, 2007). Modelling of a failure from Jettan used the estimated volumes from Henderson and Blikra (2007) of 7 and 11 $Mm^3$ (scenario 1a and 2 figure 35). The results from the modeling showed that the most exposed areas (Lyngseidet, Rottenvik, Karnes) would experience a run-up of 10-35 m in scenario 1a, and a run-up on 25-45 m for scenario 2 (NGI, 2007). In 2013 displacement wave modeling was again conducted, and based on the work by Blikra et al. (2006) and Blikra et al. (2009) of a scenario of 11 $Mm^3$ (scenario 2 figure 35). A new model technique was used giving better approximation on wave generation, prevalence and run-up. This modeling gave a maximum run-up of between 12-20m (Lyngseidet, Rottenvik, Karnes) (NGI, 2013).
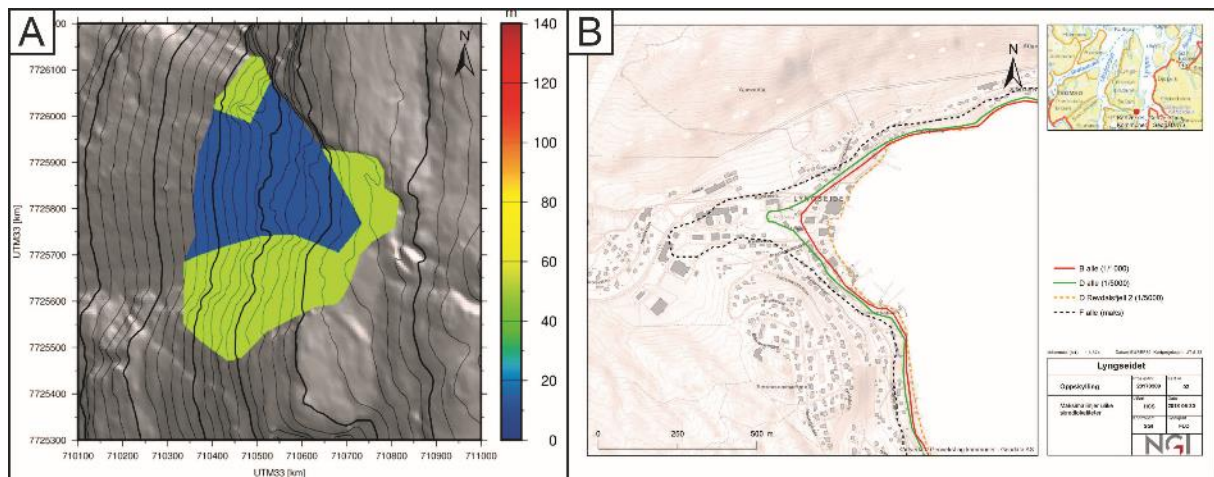
*Figure 36: A) Thickness down to sliding surface at Jettan and the extent of the different scenarios used. B) Different run-up scenarios for Lyngseidet. Modified from (Glimsdal et al., 2018).*

Based on the report from NVE (2016), homepage NVE (2019) and the thickness seen in figure 36A, a volume of 6 $Mm^3$ was estimated and a new modeling was done in 2018 (NGI, 2018). Results from the modelling gave a maximum height of the run-up at Lyngseidet to be 10 m a 1/1000-year event, and 13 m at a probability for a 1/5000-year event (figure 36B) (NGI, 2018). This result shows a much lower run-up than estimated from the previous reports from NGI (2007) and NGI (2013). The main reason for this is that the 2018 report used a volume almost half of what initially had been.

## 2.11  Stability analysis and modelling

As part of a master thesis strength testing, stability analysis, free swelling of clays, and modelling of Jettan was conducted (Nystad, 2014). For lab testing, 11 rock samples were collected at Jettan from borehole 1, three samples from the garnet-mica-schist, three samples from the mica-schist and five samples from the marble. Table 3 show which depth the samples were taken from.

Tabell 3: Overview of what depth the different rock samples were collected and with sample length in brackets (Nystad, 2014).

| Rock | Sample depth | | |
|---|---|---|---|
| Garnet mica schist | 7.7 m (80 cm) | 11.7 m (50cm) | 15.5 m (60 cm) |
| Mica schist | 76.5 m (100 cm) | 75.7 m (80 cm) | |
| Marble | 134.6 m (60 cm) | 137.3 m (50 cm) | 143.5 m (80 cm) |

Lab testing to determine density, E-modulus, Poisson's ratio and UCS was conducted. The rock samples gave the following results:

Tabell 4: Results from lab-examination (Nystad, 2014).

| Sample | Lithology | Density [g/cm$^3$] | E-modulus [GPa] | Poisson's ratio | UCS [MPa] |
|---|---|---|---|---|---|
| 1-2 | Garnet mica schist | 3.0 | 29.6 | 0 | 146 |
| 1-3 | Garnet mica schist | 2.9 | 31.7 | 0.06 | 206 |
| 1-5 | Garnet mica schist | 3.0 | 42.9 | 0.07 | 107 |
| 2-2 | Mica schist | 2.7 | 40.3 | 0.1 | 240 |
| 2-4 | Mica schist | 2.7 | 36.5 | 0.09 | 197 |
| 2-5 | Mica schist | 2.7 | 39.2 | 0.07 | 228 |
| 3-1 | Marble | 2.8 | 38.5 | 0.2 | 90 |
| 3-2 | Marble | 2.8 | 51.6 | 0.23 | 88 |
| 3-3 | Marble | 2.8 | | | 97 |
| 3-4 | Marble | 2.7 | 53.4 | 0.21 | 107 |
| 3-5 | Marble | 2.7 | | | 104 |

The garnet mica schist density is slightly higher (2.9 – 3.0 g/m$^3$) compared to what is typical in Norway for a mica schist (2.8 g/m$^3$), this could be a consequence of the high garnet content (Nystad, 2014). The mica schist densities are lower in comparison (2.8 g/m$^3$). The marble density is standard for what is typical in Norway for this rock (Nystad, 2014). The E-modulus values for the rocks at Jettan show good correlation with other analyses of the same rock types (Nystad, 2014). For the rocks at Jettan the unconfined compressive strength (UCS) collectively ranges from middle to high strength (Nystad, 2014).

Tilt table results gave a friction angle of 34.1° for the garnet mica schist, 31.1° for the mica schist and 31.0° for the marble (table 5). The mica schist and the marble correlates well with typical values for these materials, while the garnet-mica schist has slightly higher values than what would be expected (32.1°) (Nystad, 2014).

Table 5: Results from tilt test:

|  | Garnet mica schist | Mica schist | Marble |
|---|---|---|---|
| Friction angle | 34.1° | 31.1° | 31.0° |

Free swelling tests of borehole clay were also conducted from samples at 46.5 m and 53 m bgl in borehole 1. These showed free swelling of 145 (weight percent $< 20\mu m = 18.8$) and 110 (weight percent $< 20\mu m = 13.7$) respectively. Free swelling clays in Norway are active between 100 – 200 %, making the first sample medium active and the second sample slightly active (Nystad, 2014).

A simple kinematic analysis revealed that there is more than one failure mechanism possible at Jettan. Wedge failure and toppling was found as the most likely failure mechanisms (figure 37) (Nystad, 2014). Structural data used for the analysis is the same as seen in chapter 2.2.1. The kinematic analysis does not necessarily say something about the total stability of the slope, but rather that it is numerous mechanisms for failure and the possible mechanisms at Jettan (Nystad, 2014). Direct toppling, used in this kinematic analysis (figure 37B), is a failure mechanism associated with minor rock volumes and therefore often excluded for larger unstable rock slopes as Jettan (Hermanns et al., 2012b).
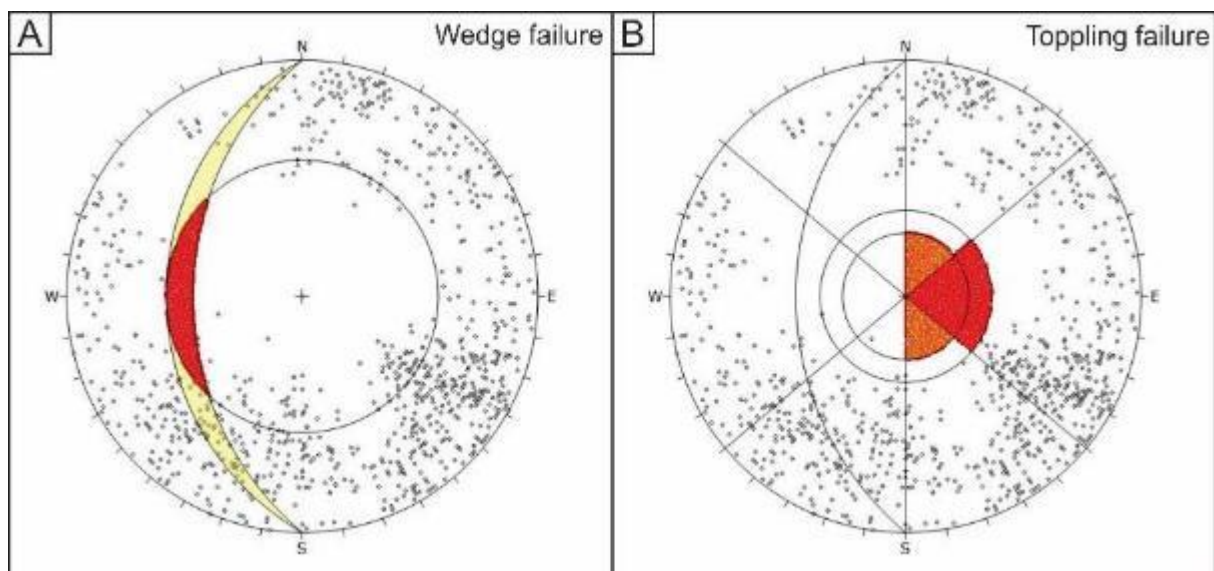


Figure 37: Kinematic analysis. A) Wedge failure is feasible as great amounts of intersections are found in the critical area (red colored area). B) Toppling failure is feasible as the foliation plots in the critical area (red colored area). Modified from Nystad (2014).

From the numerical modeling Nystad (2014) found higher deformation rates on the western side of the fault, correlating well with the place were deformation is happening today and historical deformation (pressure release after deglaciation). By increasing the K-value (stress factor) for the analysis, the deformation increases. From the SSR-analysis results show that when tested with groundwater going up to the main sliding surface, the factor of safety was reduced by fifty percent. Yet there is not likely that the groundwater reaches the sliding plane, as it is registered at 90 m bgl in borehole 2 and 3, and not recorded at all in borehole 1.

## 2.12 Hazard- and risk evaluation

As mentioned in chapter 1.1, NGU has on behalf of NVE mapped and classified unstable rock slopes in Norway. The classification system is scenario-based and secondary effects such as displacement waves or damming of river valleys are taken into account (Hermanns et al., 2012b). The hazard analysis of URS is based on two sets of criteria: 1) Investigation of the development of structures like backscarps, lateral limits and basal sliding plane, including kinematic analysis, persistence of main structures and the morphology of the URS. 2) Slide velocity, change in deformation rate, rockfall activity and historic or prehistoric events. Analysis of consequences include potential fatalities and secondary effects from the rockslide. Based on the analysis different scenarios are put into different categories depending on their risk - either low, medium or high risk (Hermanns et al., 2012b).

A rock avalanche from Jettan would reach the fjord and initiate a large displacement wave. The displacement wave could reach numerous houses and buildings, affecting several hundreds of people. This puts Jettan as a high-risk object in the risk matrix, with high hazard class and high consequences (figure 38) (NGU, 2016). The hazard score is set to 7.45, and has a minimum score at 6.25 and a maximum score at 9.50 (NGU, 2016).
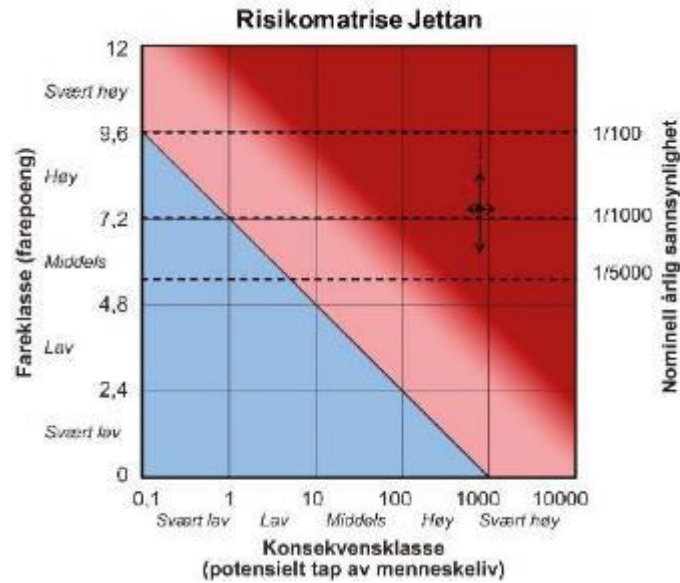
*Figure 38: Risk matrix for Jettan including nominal annual probability (NGU, 2016).*

## 2.13 Summary

The area consists of Caledonian bedrock with three dominant lithologies, foliated gneisses and interbedded layers of mica schist and marble (NGU, 2019c). In the south the area is bound by a fault striking NE-SW dipping NW, and in the north the lateral boundary is a persistent backscarp striking NW-SE. The area has two dominating steep planar joint sets with the same orientation as the backscarps (NW-SE and NE-SW), making zigzag patterns throughout the area (Skrede, 2013). The foliation has a low dip on average towards the fjord (Skrede, 2013).

The northern upper part of the unstable rock slope has a chaotic blocky characteristic with dislocated tilted terraces and blocks (Eriksen et al., 2017a; Henderson & Blikra, 2007; Skrede, 2013). Between the bigger blocks disintegrated material dominates, and NW-SW, NE-SW and N-S striking fractures and scarps comprise the whole area (Eriksen et al., 2017a). In the southern domain, a simpler geometry is seen by a terrace-scarp-terrace morphology. The terraces show a rotational movement seen by more opening of the fractures in the south compared to the north (Eriksen et al., 2017a). A talus area interpreted as a rock-glacier dominates a steeper area above (Blikra & Christiansen, 2014; Eriksen, 2013). At the top, a marble dome is present above the meeting of the two backscarps. In the lowest area thick talus

from previous rockfalls and avalanches dominate giving away to a series of large toe bulges (Skrede, 2013).

From the boreholes and geophysics multiple sliding surfaces have been interpreted. The main zones of deformation are seen around 46 m bgl in BH1 and 36-53 m bgl in BH2 (Elvebakk, 2013, 2014; Ganerød, 2013, 2014; Rønning et al., 2008; Tønnesen & Dalsegg, 2004). Considering that the boreholes and the geophysics data show crushed rock through the whole sequence, there could be sliding planes lower than what is found affecting the deformation of the main Jettan rockslide.

From InSAR data, GNSS data and continuous monitoring of the area, three areas with particularly high movement rates are found. The area with highest movement rates is the chaotic blocky area to the north with a movement of up to 50 mm a$^{-1}$ towards the NE (Eriksen et al., 2017a; Skrede, 2013). In the stepped geometrical area, movement is recorded towards NW with a yearly movement around 30 mm (Eriksen et al., 2017a). The rock glacier in the upper eastern part is the third area with high movement, and is interpreted as a rock-glacier because of its flowing movement (Eriksen et al., 2017b). Movement rates are heavily linked with seasonal variations, increased deformation in the spring during snowmelt, and a continuous deformation in the autumn due to permafrost processes (Blikra & Christiansen, 2014).

Despite the availability of many excellent published and unpublished datasets, a fully understanding of the site is yet to be achieved. To fill the gaps and to produce an engineering geology model of Jettan this thesis will look at data from fieldwork, geophysics, vector data and movement rates. Furthermore, a 3D framework will be used to gain a greater understanding of the rockslide at depth. The aim is to achieve a greater understanding of the internal structure and which mechanisms are controlling the deformation at the site.

# 3 Method

This chapter presents all methods used for this project. The main object for this study has been to gain a greater understanding of the URS. This was done by focusing on the different lithologies and creating a 3D model. Lithologies and sheared zones were mapped and investigated for a better understanding of their influence on the deformation. Geomorphological and mophostructural mapping was done to create a new and detailed geomorphological map. Structural mapping was done for producing deep going structures in the 3D model. Satellite InSAR and continuous monitoring data was used to estimate displacement and investigate the weather's impact on deformation. A 3D model was created for a better understanding of inner structures and possible sliding surfaces.

## 3.1 Geological and geomorphological mapping

Desktop mapping was conducted prior to field work based on Troms 2016 0.25 m orthophoto series (Kartverket, 2016) and DEMs from Troms 2014 0.5 and Troms 2015 0.25 m lidar projects (Kartverket, 2016). Structural, lithological and geomorphological mapping was done during one week in August, two days in September and two days in October. Structural data was gathered by a Silva Clinometer Compass and the app Clino. Together with measurements taken during the Skrede (2013) investigation, approximately 1,095 measurements were collected of joints and foliation planes. Geomorphological features including ground cover and features were mapped in the field. Morphological features related to rock slope failure (morphostructures) were of particular interest, for example backscarps, subscarps, tension cracks, displaced blocks, morphological depressions and talus material. A detailed outcrop mapping was done focusing on lithologies, shear zones and fault plane. Rock samples were prepared for thin section and analyzed using a Leica DMLP microscope equipped with a Leica DFC450 camera. A Mavic 2 Pro drone was used to capture aerial imagery and video, to aid in mapping morphological features. Hydrogeological factors such as points of seepage and alteration were noted. Positions were recorded in the field using a Garmin GPSMap 64st handheld GPS. Digital maps were produced using ArcMap version 10.6.1 based on the aforementioned spatial datasets.

Ring shear testing was done on a soil sample taken from weakness zone beneath the field station (figure 39). It was tested by Geolabs Ltd, United Kingdom. Ring shear samples were reconsolidated, manually pre-sheared through one rotation and stabilized. An effective stress of 250, 500 and 750 kPa were applied during shearing.



*Figure 39: Location of where the soil sample was collected.*

## 3.2  Monitoring data series

At Jettan there is installed continuous monitoring instruments that are of the responsibility of NVE. Data from the instruments was accessed through NVE's online portal giving live and historical records from weather station, crackmeter, extensometers, tiltmeters, lasers and GPSs. Air temperature and precipitation records was taken from the weather station gathered from Norsk_Klimaservicesenter et al. (2020). Tiltmeters was not included as the data is less reliable, hard to interpret and time consuming.

### 3.2.1  Weather station

Air temperatures are measured by a Vaisala HMP45A every five seconds and has an accuracy of ±0.2 °C at 20 °C. At -40 °C the accuracy is ±0.5 °C and at 60 degrees the accuracy is at ±0.4 °C (VAISALA, 2006). Maximum, minimum and mean air temperatures were gathered for comparison to movement rates. Of particular relevance was the time of the recording, maximum

and minimum temperatures, when the mean temperature shifted from negative to positive and vice versa, as well as anomalies. Precipitation is measured by a Lambrecht 1518H3 every hour and has an accuracy of ±2 % (Lambrecht, 2017). The precipitation measurements cannot distinguish between rain and snow. Thus, it is presumed that precipitation occurring when temperatures are below zero is snow. A particular interest was taken in records that showed high precipitation and was compared to movement rates.

## 3.2.2  Continuous monitoring

Only records from the continuous monitoring data that had registered measurements for a whole year was included in the results. Data records for the crackmeters are taken from 2009 to 2018 for crackmeter 1, 3, 4, 6, 7 and 10, from 2010 to 2018 for crackmeter 8, from 2011 to 2018 for crackmeter 2 and 5, and from 2011 to 2018 for crackmeter 9. Data records for the extensometers are taken from 2011 to 2018. Data records for the lasers are taken from 2009 to 2018 for laser 1, from 2014 to 2018 for laser 2 and from 2015 to 2018 for laser 3. Data records for the GPS's are taken from 2011 to 2020. For the extensometers and lasers average yearly compression, extension and movement was calculated. Yearly average movement was calculated for the crackmeters. For the GPS's yearly average N/S, E/W, height, horizontal and total movement was calculated, and additionally the dip and direction were found. There was also done an analysis looking at change in movement for the different instruments trying to link it with precipitation and temperature. In the following the different specifications for the instruments will be presented.

## 3.2.2.1  Crackmeter

Crackmeters are used to measure movement in cracks and joints. An anchor is installed on both sides of the crack, and a transducer is mounted on the anchors. If the crack/joint is opening or closing, it will cause a change in the frequency signal produced by the transducer. This signal is processed and calibrated relative to for example temperature, and then displayed in millimeters or inches. The first reading is used as datum, and subsequent readings are correlated to the datum for determining the magnitude, rate and acceleration of movement across the crack (Durham_Geo_Slope_Indicator, 2019). At Jettan 11 crackmeters from Durham Geo Slope Indicator (VW crackmeters) are installed, having a precision of 0.3 mm (Durham_Geo_Slope_Indicator, 2019). There is no official measurement of the installations orientation, so the orientation is based on the opening of the specific crack where the instrument is mounted.

### 3.2.2.2 Extensometer

Extensometers are used to measure change in distance between two rock surfaces. The extensometer is mounted on the two rock surfaces and measure the change in distance by sending a pulse through a rod and a movable magnet which will create a magnetic field. If the distance between the rock surfaces have changed, the magnet along the rod have shifted position resulting in a new signal. At Jettan three extensometers from MTS Temposonics (R-series analog extensometers) are installed, having a precision of 1.0 μm (Temposonics, 2019). There is no official measurement of the installations orientation, so the orientation is based on the opening of the specific crack where the instrument is mounted.

### 3.2.2.3 Laser

Lasers are used to measure change in distance between two specific locations. By mounting a laser and a reflector, the distance between these two could be measured by using the refection of a laser beam. The wavelength of the beam is known, and the time the beam uses to get reflected back is measured. At Jettan 3 lasers by Dimetix (Laser 1 Dimetix DLS-B, laser 2 Dimetix DLS-C and laser 3 Dimetix FLS-C) are installed, having a precision of ±1.5 mm for the DLS-B and DLS-C, and a precision of ±1.0 mm for the FLS-C (Dimetix, 2016a, 2016b, 2016c).

### 3.2.2.4 GPS

GPSs are used to measure change in position of the GPS. The GPS is mounted on a specific point and sends signals of its position to a satellite several times a day. The movement gets measured in E-W-direction, N-S-direction and vertical direction. At Jettan 11 GPS's by Trimble (Trimble NetR9 RTK/RTK GNSS) are installed, and has a precision on 3 mm (+ 0.5 ppm RMS) in the horizontal plane and 5 mm (+ 0.5 ppm RMS) in the vertical plane (Trimble, 2014).

## 3.2.3 Remote sensing

### 3.2.3.1 InSAR

Synthetic aperture radar (SAR) is an instrument imaging the earth from space. InSAR (Interferometric synthetic aperture radar) is a method which is used to discover surface displacement by radar data. The satellite orbits the earth from pole to pole. Traveling from N-S and looking down to the ENE is the ascending orbit, while traveling from S-N looking down to the WNW is the descending orbit (figure 41). When traveling in orbits it sends out and

receives radar beams in an angle to the earth surface (Line of Sight (LOS)). By recording the range and the azimuth direction, the position of the resolution cell could be found (figure 40). The range direction is found by measuring the return of the reflected radar beam. The azimuth direction is resolved by calculating by help of the Doppler spread method, which compares the reflected radar echo from objects in front of the satellite with objects behind the satellite (Rosen et al., 2000). The process geo-coding converts the radar coordinates obtained to map coordinates (Eriksen, 2013; Lauknes et al., 2010).

When a satellite records multiple signals for a specific area over time, it is possible to find surface displacement by comparing the different signals. The signal emitted have a certain wavelength and amplitude, so if the reflected signal has changed it may be due to surface displacement. However, the change could also be due to a change in the position of the satellites compared to an earlier flyover, turbulence or noise as a response of drift in frequency of the radar. To find the actual displacement change the factors mentioned above must be subtracted. The obtained displacement is only found for the LOS, therefore the displacement could be larger if movement occurs outside of the LOS vector (Eriksen, 2013).

For this project data from Sentinel-1 satellite was used, and the InSAR imagery acquired from InSAR Norge (NGU, 2020). The descending track is used since it has a LOS down towards WNW. This orientation fits well with the movement direction at Jettan. Three descending tracks containing data for the summer months from July 2016 to September 2019 make up the records.
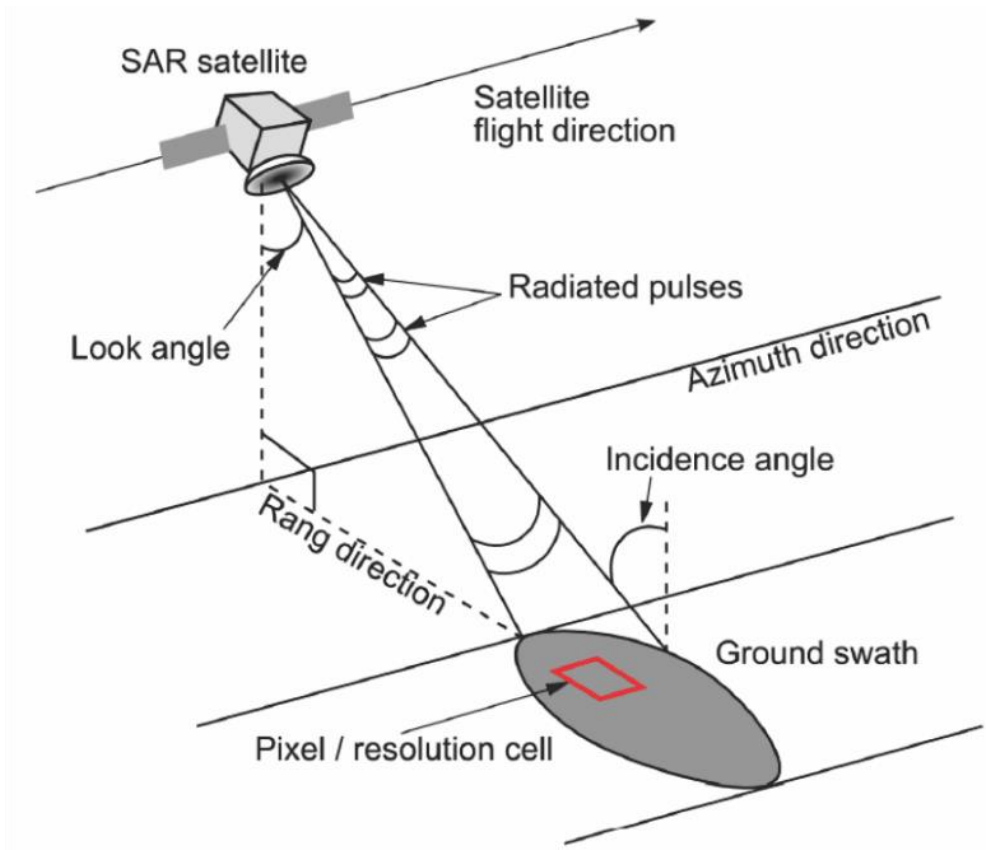
*Figure 40: Illustrative overview of the geometry for a SAR satellite. Modified from Eriksen (2013).*
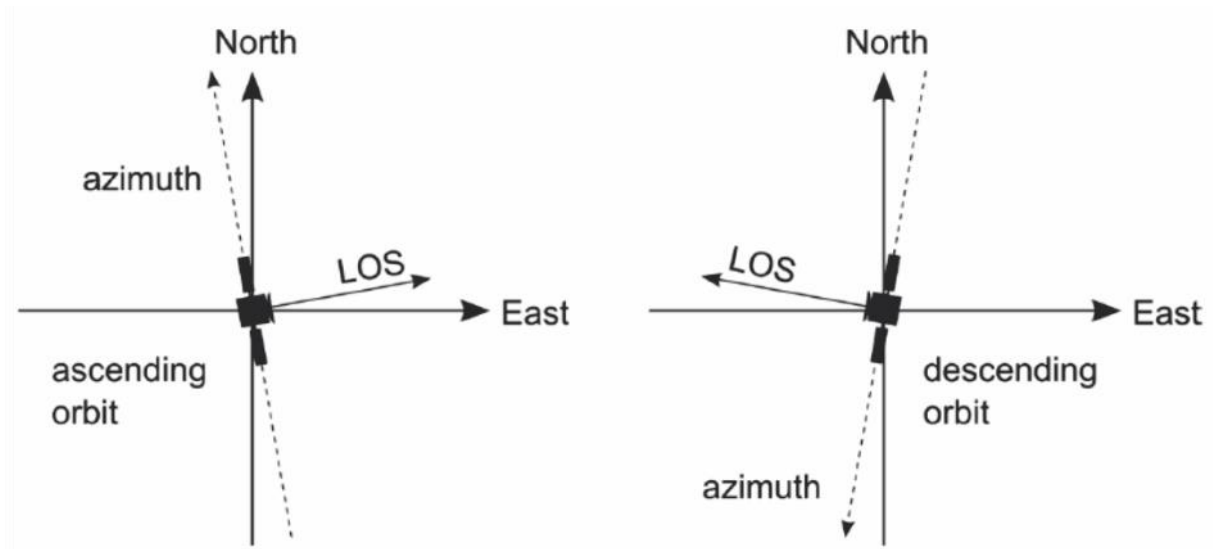


*Figure 41: Illustration showing LOS and azimuth for ascending and descending orbits. Modified from Lauknes (2011).*

## 3.3 3D modeling

For 3D modelling Leapfrog Works by Seequent was used. Leapfrog Works is a 3D implicit geological modelling solution for visualization and interpolation. It gives a complete solution for fast and dynamic modelling of the ground conditions, examinations of the cooperation with the engineering design and intuitive 3D visualization tools that allows communicating an easily understandable model (Seequent, 2020).

The software requires a topographic surface as the base for model building. DEMs from a combination of the Troms 2014 0.5 and Troms 2015 0.25 m lidar projects was used (Kartverket, 2016). Borehole data was inserted as csv files, a collar file determining the position and the depth of the different boreholes, interval file specifying segments down the borehole with identified values and foliation was added as planar structural data. Several interval files were made designating lithologies, crushed zones, core loss and faults. GIS data created for the site were inserted and modified, including the following; backscarps, minor scarps, depressions, tension cracks, sinking holes, moraine ridge, valleys, lobes, fault, displaced blocks, disintegrated blocks, fractured rock, talus, avalanche deposits, till cover and seepage points. A geological model was built based on these data sources.

Two different geological models were made in Leapfrog Works, one model for bedrock lithology and one model for the different failure scenarios. For creating a bedrock model, lithological boundaries are required. These lithological boundaries are based on the logged borehole lithologies and GIS lines marking lower and upper boundaries of different unites registered in field and by orthophoto investigations. The scenario-based model was built by including defining structures like scarps, depressions and cracks, and one or several sliding surfaces that was created from borehole data like crushed zones, core loss and faults. Scarps and sliding surfaces were made by creating planes with an average dip and dip direction for the specific site. For instance, a scarp was made by taking the average dip direction and average dip from all the measurements taken on the scarp in field. If necessary small adjustments were done to make it fit to the DEM.

# 4 Results

This chapter will present a description of the lithologies, geomorphology and geological features present in the area found during fieldwork. The different domains will be described. Displacement rates in the area will be presented and is taken from the continuous monitoring data and InSAR-data. Results from the 3D-modeling showing different cross-sections, domains and different possible failure scenarios will be produced. Precipitation and temperature will be presented and connected to movement found from the continuous monitoring.


## 4.1 Lithology

A bedrock map has been produced based on previous work (see chapter 2.1.2) and complimented by field investigations (figure 48). A larger calcite marble unit was found in the western area below the dolomite marble dome, and in the middle part of the URS, the calcite marble bands were fully mapped throughout the area. This lithology has historically been classified as a calcareous acidic gneiss (see chapter 2.2.2), but is here described as a calcite marble due to field investigations that accompanied this project.

### 4.1.1 Calcite marble

The rock has a light brown color and contains dark mica (biotite) as well as quartz, but is primarily composed of calcite (figure 42B). This brown color of the rock is rather a consequence weathering than a result of its mineralogy. Crystals are more or less equigranular (1 mm), with the exception of the biotite being smaller (<1mm). The intensiveness of the foliation varies from location to location, where in some places it is more distinctly developed than in others. Calcite coating were found at one location (northwestern valleys in domain 5, see figure 49), and is suggested to be dissolution of calcite of the host rock (figure 42D). The calcite marble is either interlayered together with garnet mica gneiss and quartz-rich lenses (figure 42A), or seen as massive calcite marble scarps (figure 42C) ranging up to several meters thickness. Since calcite marble is often interbedded with garnet mica gneiss and quartz-lenses, these three lithologies are handled as one unite. Calcite marble is the dominating rock in the interbedded sequences with layers up to 1-2 m thickness, while the gneiss layers often are less than 1 m. The quartz is either seen as lenses or layers that are only a few cm thick.
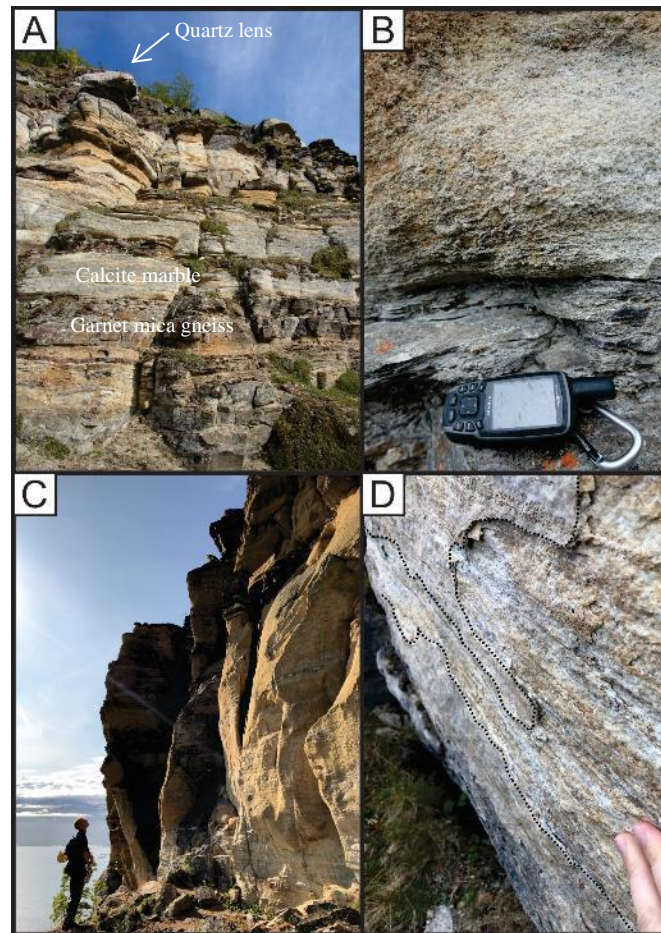
*Figure 42: Calcite marble. A) Interaction between the calcite marble and the garnet mica gneiss, on top a quartz lens. B) Photo of calcite marble showing its equigranular texture. C) Large subscarp of calcite marble in the lower part of the URS. D) Outer cover on the calcite marble.*

### 4.1.2 Dolomite marble

The color of the rock varies from light to dark grey, whereas the darker coloration likely stems from biotite. Mineralogically the marble is mainly composed of dolomite but also features calcite, quartz as well as tremolite and diopside (figure 43B and 43C). Crystals are unequal in size, were the tremolite is the largest and can be up to 2-3 cm long (figure 43A). The intensiveness of the foliation varies from not developed to poorly developed. Tremolite crystals found in the dolomite marble in domain 5 (figure 49), are observed in different quantities. In some locations, it looks like they show a preferred orientation along planes, whereas in other locations they display no such trend. The dolomite marble is also found as a lens in the lower northern area of domain 1 (figure 49), expressed in the backscarp, a displaced block below the backscarp and in the upper part of Jettankallen (figure 43D). The dolomite marble here contains diopside crystals.
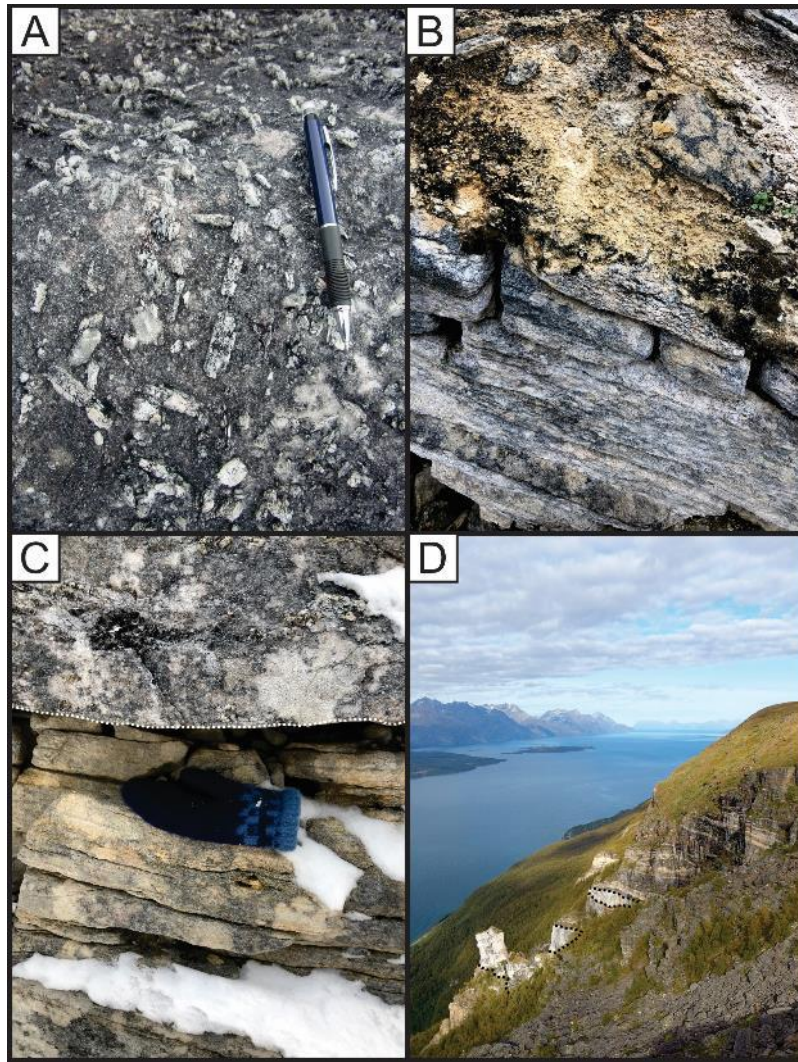
*Figure 43: A) Tremolite crystals in the dolomite marble. B) Weathering resulting in disintegration of a dolomite marble with some traces of foliation. C) Distinct boundary between dolomite marble on top and calcite marble in the bottom. D) Dolomite marble seen in the lower parts of Jettankallen, displaced block and as a lens in the backscarp.*

### 4.1.3 Garnet mica gneiss

The rock is banded and shows an alternation of dark and lighter colored layers. The garnet mica gneiss is the most abandoned rock in the area and contains different amounts of micas (biotite and muscovite), quartz and garnet (figure 44). A transition between a gneiss and a schist was observed, but no trend of where one or the other expresses were found. Iron coating was found in some outcrops where the rock was garnet rich (figure 44A). The iron coating is a result of oxidation of iron2+ to iron 3+.
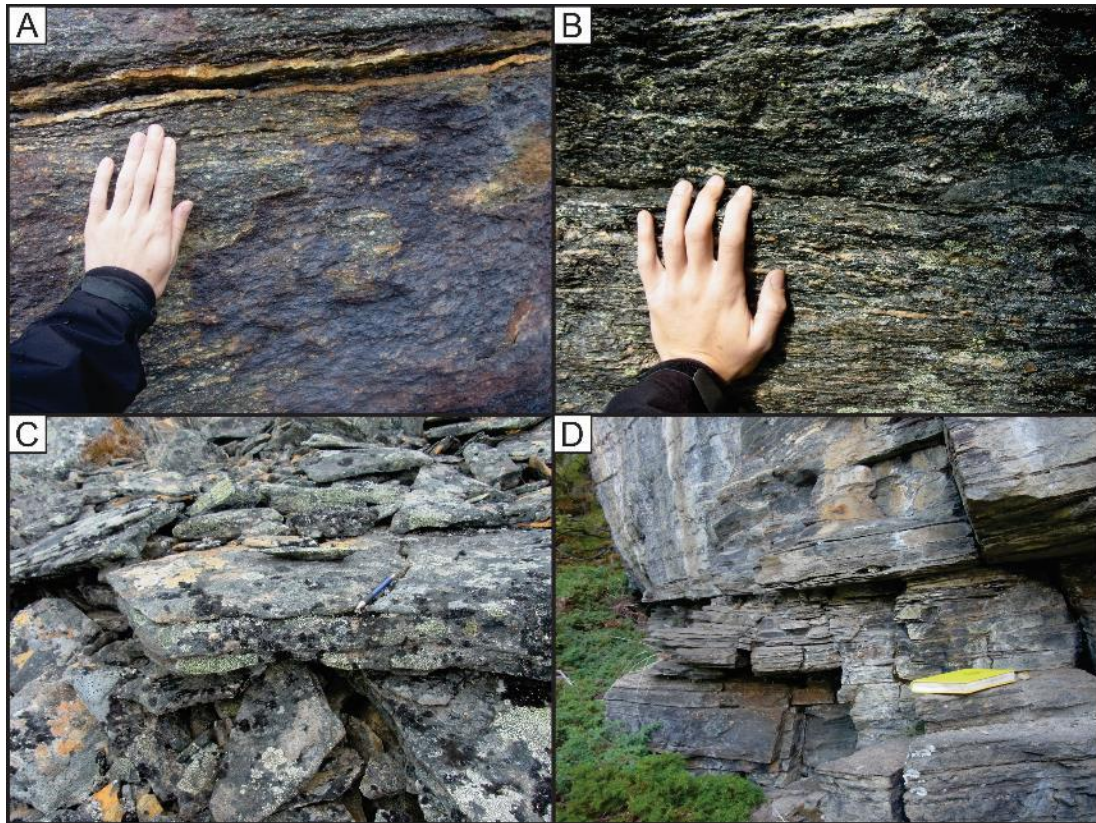
*Figure 44: A) Iron coating on the garnet quartz mica gneiss, most likely as a consequence of high garnet content. B) Garnet quartz mica gneiss. C) Smaller blocks of garnet mica gneiss split by the foliation. D) Zone with higher mica content showing fractures along mica planes (foliation).*

## 4.1.4 Lithological weak zones

Within the garnet mica gneiss, layers of sheared and preferentially weathered material of the same rock can be found (figure 45). These layers vary from a few centimeters to around one meter thickness, and are parallel to the foliation. They are seen as either incohesive yellow banded and foliated material (figure 45C and 45D), or as heavily deformed lithified ductile shear zones (figure 45A). The shear zones contain small pockets or lenses of residual soil (see chapter 4.1.5). Sigma clasts were found in the shear zones operating as a shear sense indicator. There were observed quartz veins inside the shear zones. Seepage is observed coming out on top or bottom of the weak zones, indicating that the weakness zones are contributing to the fluid flow of the URS (figure 45C).
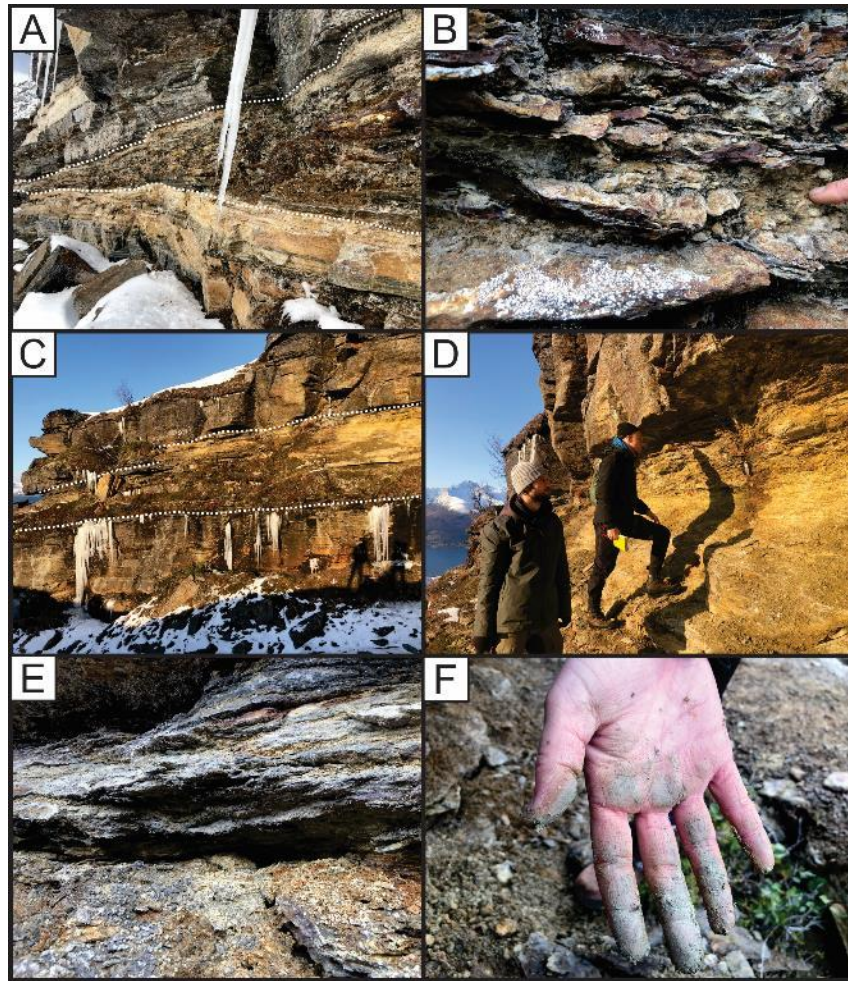
*Figure 45: Filed photographs of weakness zones at Jettan. A) Sheared zone within an outcrop of calcite marble overlying garnet mica gneiss. B) Sigma clasts acting as shear sense indicators. C) Weathered foliation-parallel zone within the garnet mica gneiss. Seepage is seen as icicles at the lower part of the layer. D) Close-up of layer from C), showing location of soil sample collection from reconsolidated/ring shear testing. E) Fine sandy silt and clay layer within the garnet mica gneiss (F).*

Three samples were taken for thin section analysis representing different zones of the weathered layers. NF1 was taken at a comparatively less affected portion of the shearing, NF2 was taken from the transition into the weaker shear zone and NF3 being synonymous with its center (figure 46A).

NF1 consists of quartz, biotite, garnet porphyroblasts, kyanite, plagioclase and K-feldspar. The foliation is a result of bands of quartz and biotite, which are deflected around the garnets (figure 46B and 46C). C'-type shear bands are observed in the quartz-mica layers (figure 46D). NF2 features amphibole and minor portions of muscovite compared to NF1 (figure 46F and 46G). The grains are strongly elongated. A more distinctive shape preferred orientation (SPO) is found in the quartz and signs of it in the garnet compared to NF1 (figure 46E). NF3 is

characterized by sharper and wavy grain boundaries, and the biotite and quartz grains look flattened and elongated (figure 46H). In NF3 a more distinct undulose extinction is found, whereas in NF1 the quartz grains feature less dislocation and bending of the crystal lattice. Increased weathering has produced cracks in the NF3 sample, resulting in a corroded appearance of the garnets that are seen in chaotic quartz-rich zones (figure 46I and 46J). NF3 also features a high amount of opaque minerals, possibly as a consequence of the increased degree of weathering in the sample.
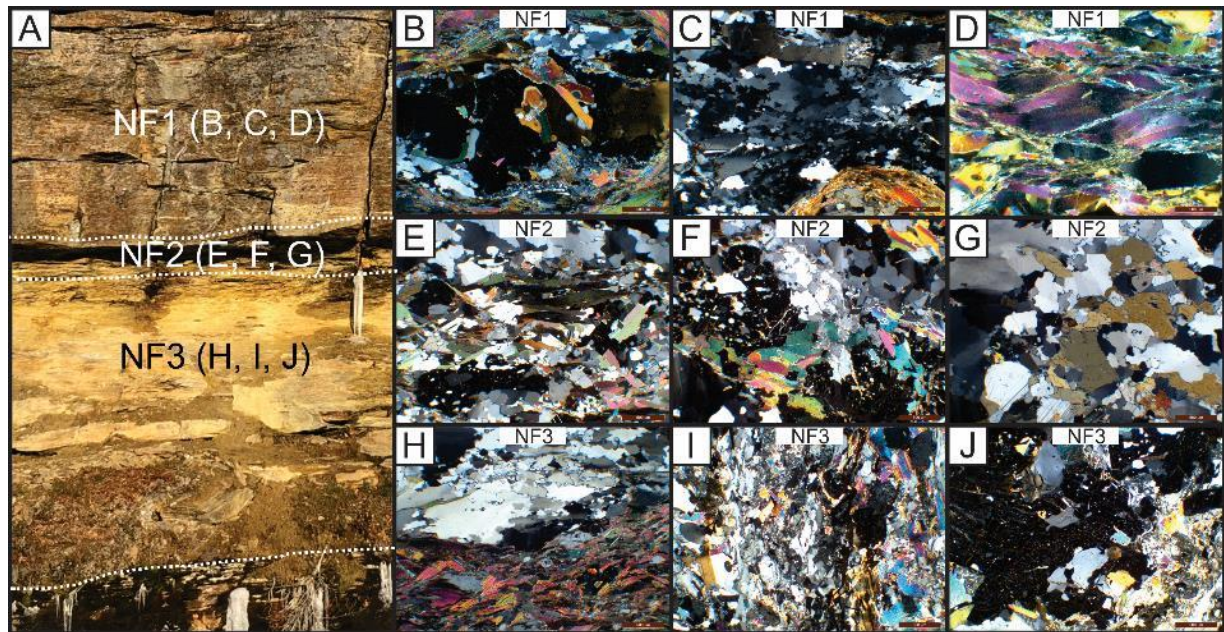


*Figure 46: Thin section photos from the Jettan weakness zone in the garnet mica gneiss. A) Relatively position where the different samples are taken from. B) Matrix in the form of biotite and quartz being deflected around the garnet. C) Foliation formed by bands of quartz and biotite. D) C'-type shear bands. E) Garnet showing signs of SPO (large black grain at the bottom). F) Muscovite and garnet displaying signs of weathering. G) Amphibole (brown) in the quartz. H) Sharper and wavier grain boundaries in quartz and biotite. I) Dirty-messy quartz rich zones. J) Garnet seemingly affected by the increased weathering of the rock, "eaten up" appearance. All photos were taken under crossed polarizers.*

### 4.1.5 Soil horizons

Soil was found inside the lithological weak zones seen either as a horizon or as pockets in the shear zones. The soil horizons have a grayish yellow color and accommodate fine sandy silt with minor portions of clay. At the time of field work (August, September and October) the soil was moist and it is therefore considered to be representative for the whole year. Furthermore, the soil displayed a thinly laminated undulating fabric and is easily intended by thumb (figure 45D, 45E and 45F). They are thought to be residual soils as they are weathered in situ and has

not been transported. The contact between the residual soil and the host rock (garnet mica gneiss) is either abrupt or gradual up to a meter. Results from the ring shear testing of the soil showed a residual shear strength of 17-18.5°.

## 4.1.6  Rock mass units

From field investigations a rock mass unite table was made for describing different unites present at Jettan (table 1). The rock mass units are described regarding strength, weathering, degree of fracturing, defect properties and geological strength index (GSI).

| Lithology | Rock mass unit | Description | Photo | Typical intact strength | Weathering (INC, 2005) | Degree of fracturing (INC, 2005) | Defect spacing (INC, 2005) | GSI (Marinos et al., 2000) | Defect persistence | Roughness (NGI, 2015) |
|---|---|---|---|---|---|---|---|---|---|---|
| Dolomite marble | Massive dolomite marble | Whitish-grey massive reactive marble with infrequent joints. Joints contain large crystals | A | 190 MPa (Xie et al., 2011) | Fresh to slightly weathered- no discolouration | Massive with widely spaced defects. | Bedding >1m thick. Defects 0.5-2m spacing. | 90 | >2m | Undulating rough |
| Dolomite marble | Bedded dolomite marble | Whitish-grey bedded reactive marble with infrequent joints. Joints contain large crystals | B | 190 MPa (Xie et al., 2011) | Fresh to slightly weathered- no discolouration, some decomposition | Moderately thickly bedded and widely spaced defects. | Bedding 0.2-0.6 m thick. Defects 0.5-2m spacing. | 70 | >2m | Undulating rough |
| Dolomite marble | Blocky/transported dolomite marble | Large blocks (>1m diameter) of above, transported via rockfall, rock glacier and rockslide activity | C | 190 MPa (Xie et al., 2011) | N.A. | N.A. | N.A. | N.A. | N.A. | N.A. |
| Calcite marble | Calcite marble | White-yellow bedded coarse grained. Non-reactive. | D | 88 - 107 MPa (Nystad, 2014) | Fresh to slightly weathered, some discolouration. | Thinly laminated to thickly bedded | Bedding ranges from laminated to >2m | 85 | 0.5 – 2m | Undulating smooth |
| Garnet quartz mica gneiss | Gneiss | Dark blueish grey foliated gneiss. | F & H | 107 - 240 MPa (Nystad, 2014) | Fresh to slightly weathered, some oxidization and calcite coating on defect surfaces. | Moderately widely spaced joints. Very thinly spaced foliation. | Joints 0.2 to 0.6 m. Foliation 6 to 20 mm. | 55 | >8m | Stepped smooth and planar smooth |
| Garnet quartz mica gneiss | Shear zone | Brown-yellow and grey heavily deformed and fragmented shear zone containing pockets of soil. | G | N.A. | Moderately to highly weathered. | Very to extremely closely spaced | <20 – 60 mm | 15-25 | N.A. | N.A. |
| Garnet quartz mica gneiss | Disintegrated shear zone | Brown-yellow decomposed shear zone. | E | N.A. | Completely weathered | N.A. | N.A. | N.A. | N.A. | N.A. |
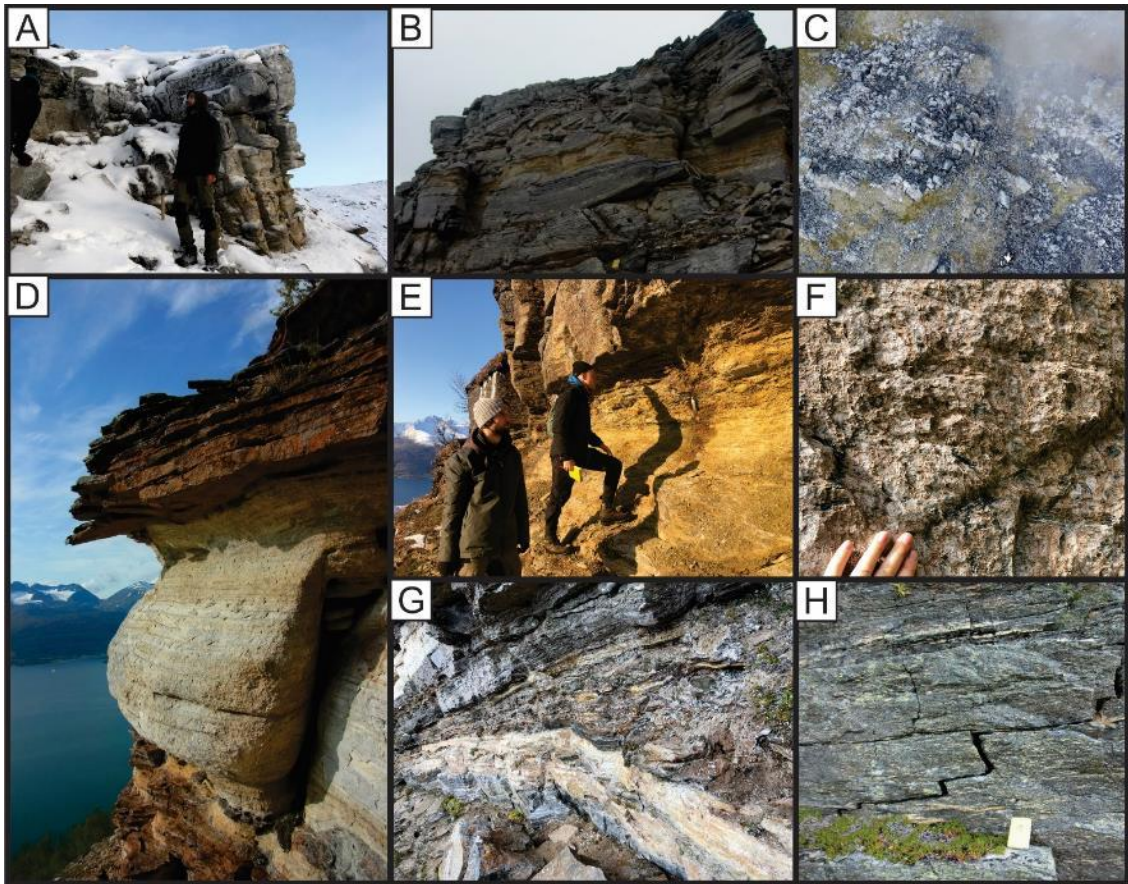
*Figure 47: Rock mass units. A) Massive dolomite marble on top of interbedded calcite marble. B) Bedded dolomite marble. C) Blocky and transported dolomite marble seen from drone photography. D) Calcite marble. E) Decomposed shear zone of garnet quartz mica gneiss. F) Calcite coating on the garnet quartz mica gneiss. G) Shear zone with fragmented and deformed garnet quartz mica gneiss. H) Garnet quartz mica gneiss with stepped defect*

### 4.1.7 Bedrock map

The bedrock map (figure 48) shows the location of the different lithologies described in the sections above. The map includes the NE-SW striking normal fault and the nappe boundary between the upper Normannvik nappe and the lower Kåfjorden. The nappe boundary is taken from NGU's N250 bedrock map (NGU, 2019c).
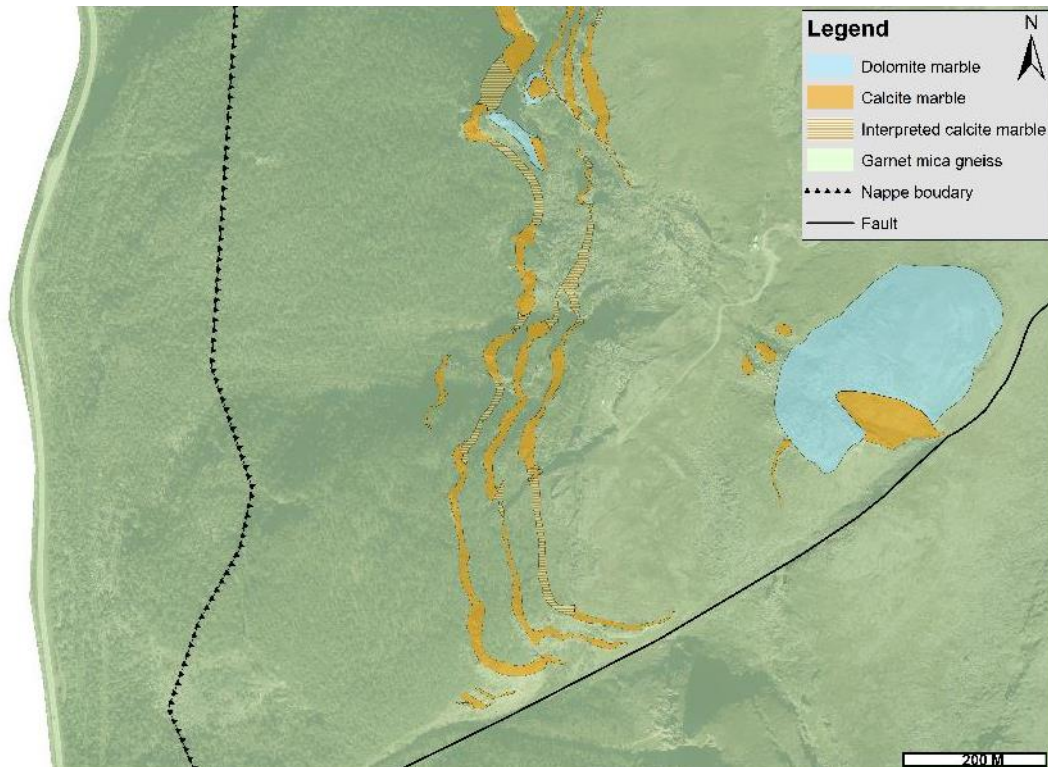


*Figure 48: Bedrock map including fault and nappe boundary.*

## 4.2 Geomorphology

Based on previous work (Eriksen et al., 2017b; Skrede, 2013) Jettan has been divided into seven different domains (1-7), mainly established from movement and geomorphology (figure 49). In the following a description of the geomorphology of each domain accordingly.

*Figure* 49*: Domains at Jettan.*

Slope and hillshade maps are also presented for a better understanding of Jettan, and in connection to geomorphological features (figure 50 and 51). The following geomorphological features were mapped: backscarps, scarps, tension cracks, depressions, valleys, front of avalanche deposit, fault, moraine ridge, dislocated blocks, fractured rock and rock fall deposits (figure 52).
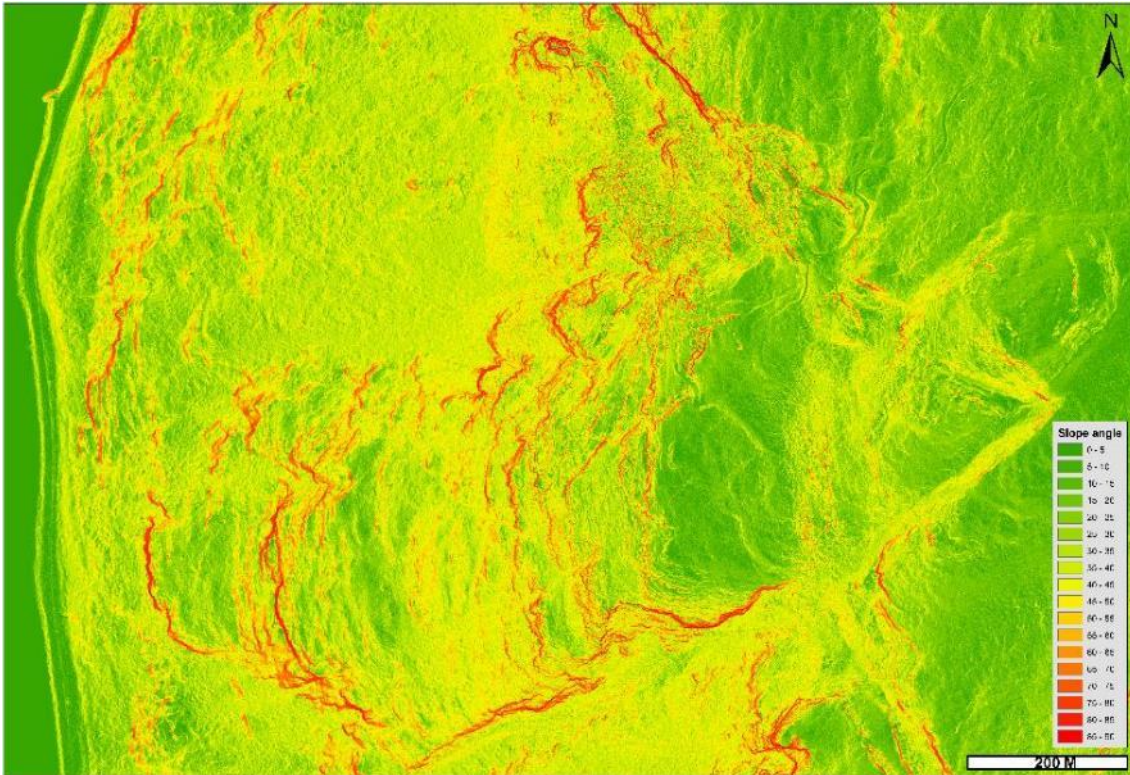
*Figure 50: Slope dip map of Jettan.*
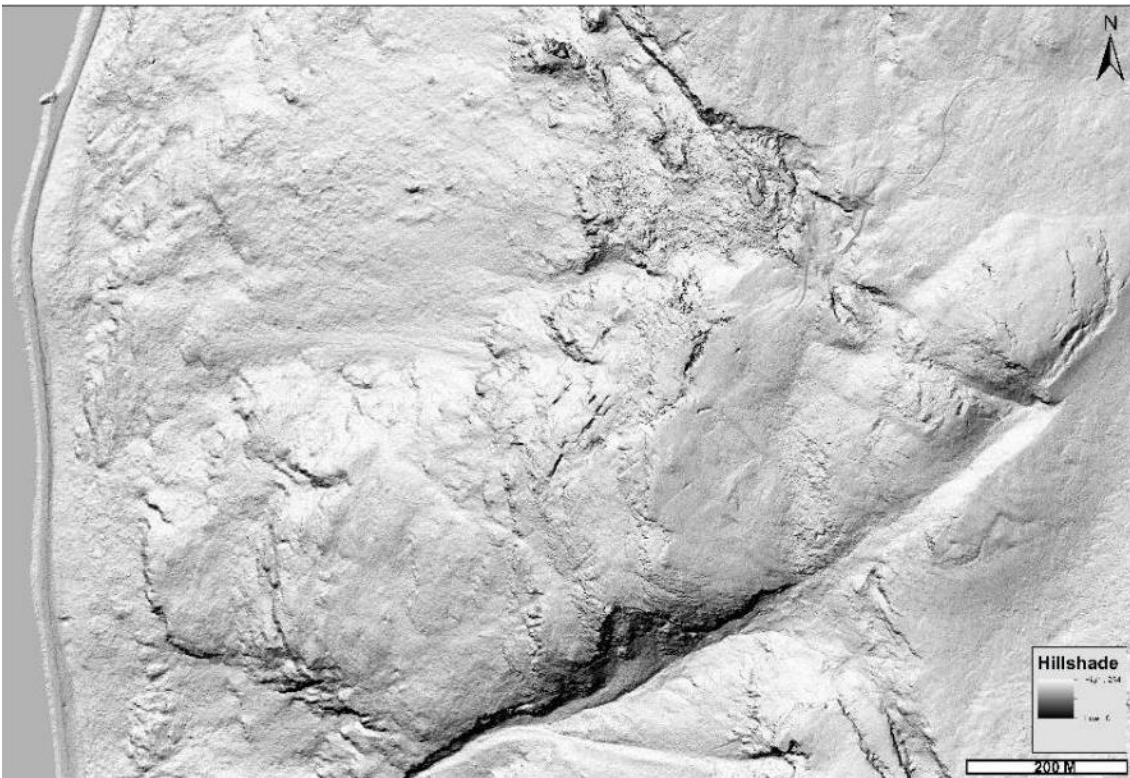


*Figure 51: Hill shade map of Jettan.*
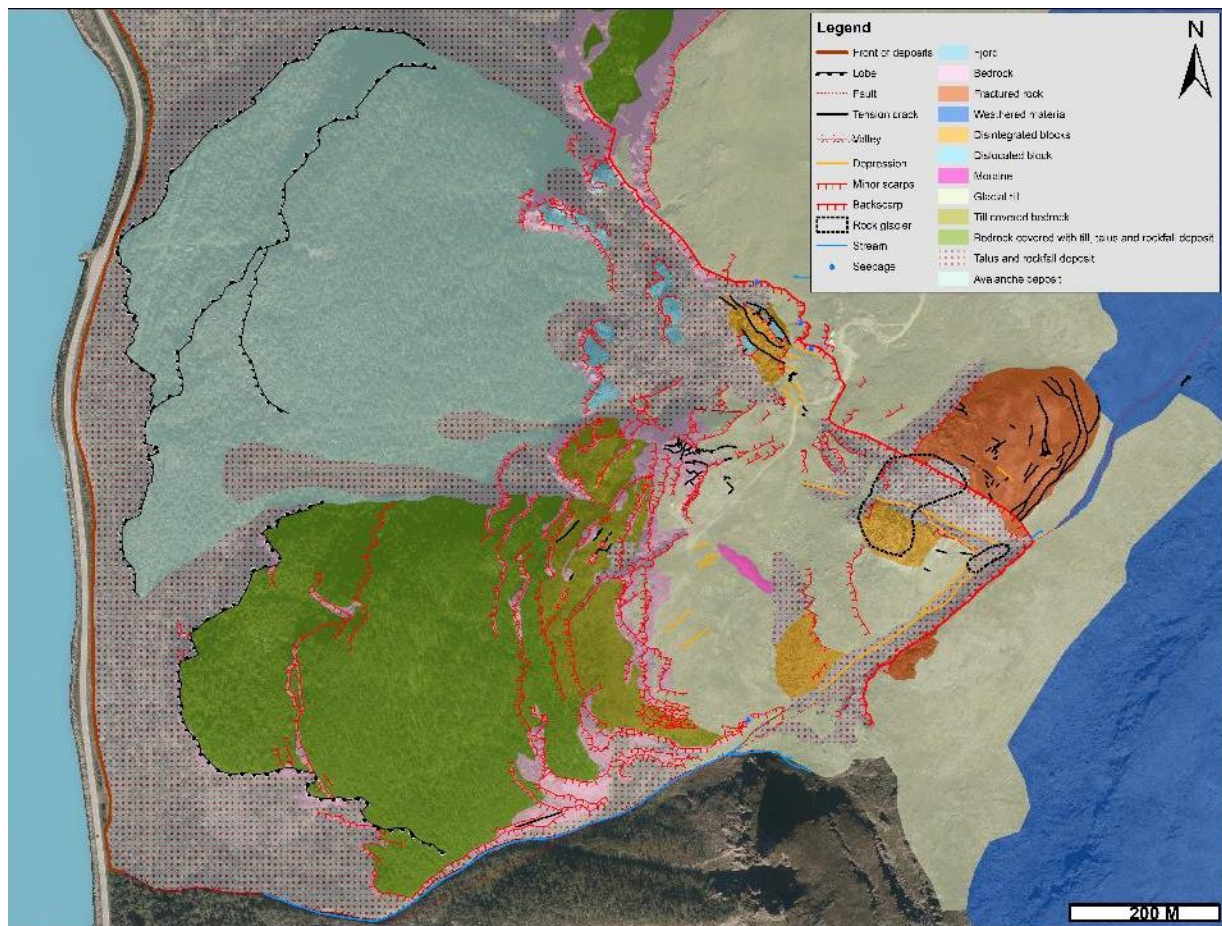
*Figure 52: Geomorphological map over Jettan.*

## 4.2.1 Domain 1

Domain 1 encompasses the northernmost section of the unstable slope, and is characterized by a mass of dislocated blocks and an area with rock fall deposits in combination with scarps. It has been mapped as the fastest moving surface area of the URS (Eriksen et al., 2017a; Eriksen et al., 2017b; Henderson et al., 2010).

At the rear of the domain, the NW-SE trending backscarp delineates the unstable area from the stable area. The overall strike of the backscarp is disrupted by a small retrogression, which matches well with the inner block (block 1) (figure 52, 53A and 53B). East of the inner block orthogonal joints striking NW-SE and NE-SW build up a zigzag pattern on the backscarp. Several seepages points have been observed on the backscarp (figure 53D). Further to the northwest the backscarp straights and is increasingly vertically expressed, up to 100 m high at the highest point.

The large displaced block measures approximately 30 m long, between 10-12 m wide and 10 m high. Deep open cracks are seen on the paleo surface of the block. To the northwest and west are more dislocated blocks separated by areas of disintegrated blocks filling the space. The disintegrated blocks form a ridge and trench geometry (figure 53A and 53C), with the same orientation as the blocks.

The outermost block (block 2) of this area has the same orientation as the innermost block (block 1) and marks a boundary to a steeper area below. This block is between 24 and 28 m long and between 9 and 15 m wide. On top of this block is the collar of borehole 3, a GPS and a laser receiver.

Below the outer displaced block (block 2) talus material and disintegrated blocks dominates. The talus material consists of large blocks often with a flat surface along mica layers. Several larger displaced blocks are located in between the talus material including Jettankallen (figure 53B). To the north the area is cut by the backscarp and to the south by a scarp and or a depression in the terrain marking the transition to domain 3. Below the domain old avalanche deposits are found and are now vegetated (domain 6).
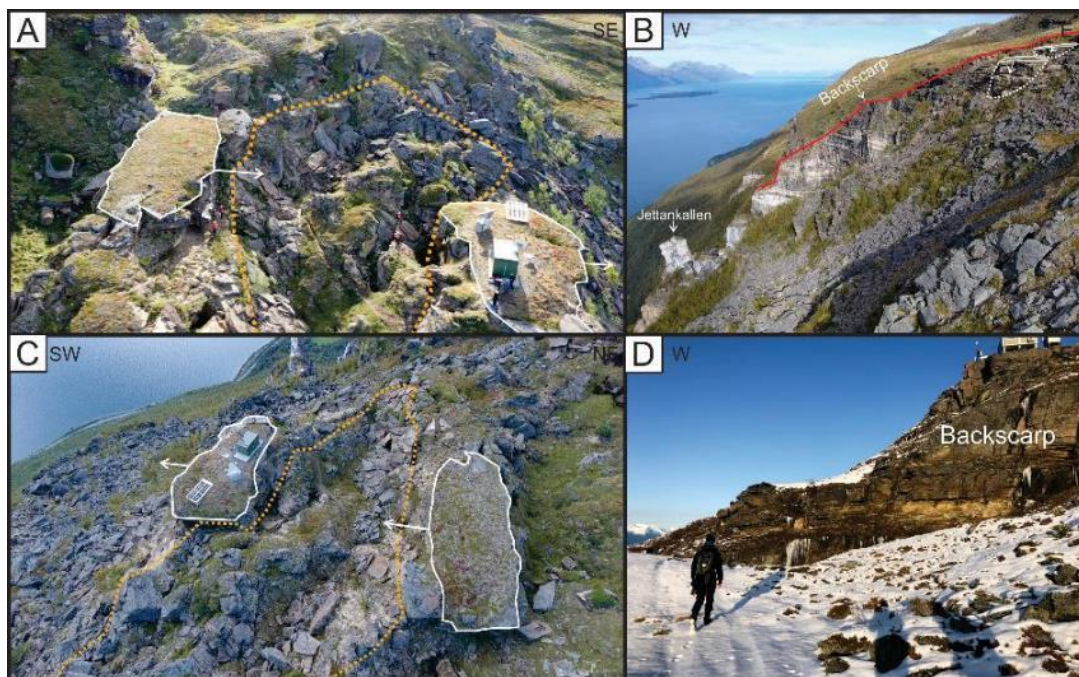


Figure 53: Domain 1. A) Drone photograph showing the two displaced blocks (white polygons) and the disintegrated blocks in between (orange dashed polygon). B) Drone photo illustrating the backscarp, Jettankallen, talus and rock fall material and the two displaced blocks. C) Drone photograph showing the two displaced blocks (white polygons) and the disintegrated blocks inn between (orange dashed polygon). D) Filed photograph of the upper part of the backscarp and seepage seen as ice.

### 4.2.2 Domain 2

Domain 2 is the center of the URS, the domain is predominantly a plateau covered in an unsorted, broad ranging size of sediments (mostly till). Below the backscarp in the north end the plateau is cross cut by morphological depressions and sink holes (figure 54A). These are formed by till draped over open fractures. The depressions are generally oriented NW-SE sand have small ridges between them. They are up to 3 m deep. The sinkholes often appear in connection with the depressions, seen at the ends of the depressions, and often where fractures intersect each other. A scarp in the northwest striking NE-SW marks the outer limit and the transition to domain 1 (figure 53A).

In the middle part of the domain, a NW-SE striking scarp including a displaced block (figure 54A) aligns well with block 2 in domain 1 and the northwestern valleys found in domain 5 (see chapter 4.3.6). Below the scarp, the plateau has a gentle dip towards southwest and is characterized by several smaller scarps striking NE-SW. The scarps are draped by a till cover and present a height difference in the terrain of up to one meter (figure 54B). The westernmost scarp mark the outer boundary of the domain and a transition to a steeper slope area, with a dip from 40 to 50°. The southernmost part of the plateau has a low dip towards the west, dominated by till cover and a transition to a steeper dip marking the boundary to domain 5, towards the east.
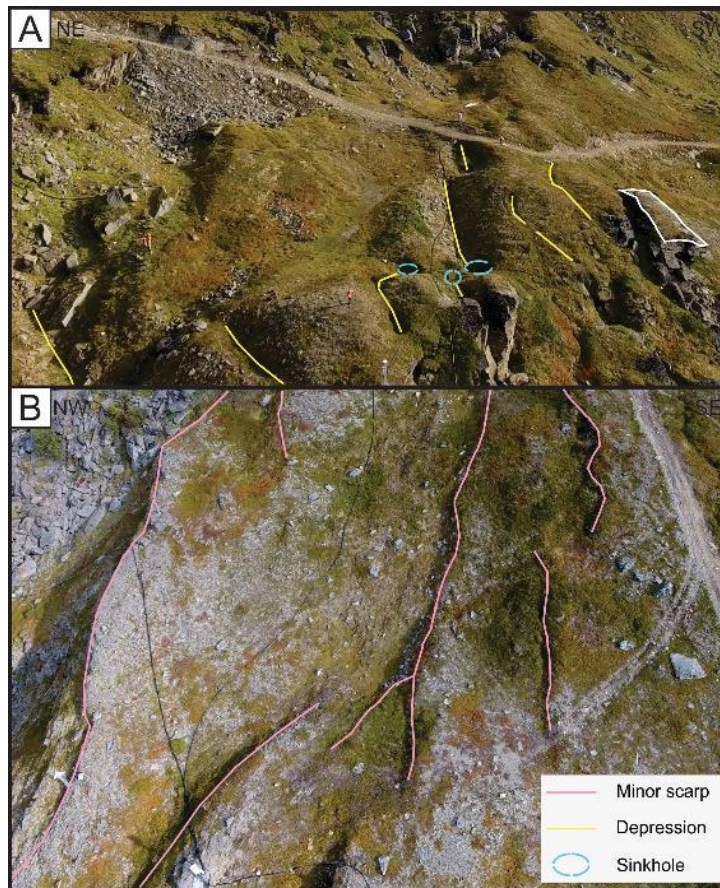
*Figure 54: Domain 2. A) Drone photograph illustrating depressions and sinkholes at the northern terrace. White polygon shows a displaced block.  B) Drone photograph of the southern terrace with smaller scarps and the western outer scarp.*

### 4.2.3  Domain 3

Domain 3 is characterized by a large open crack (crack 1) in the upper part and a scarp-terrace-scarp morphology downslope. The domain has been mapped as the second fastest moving area of the URS and includes both borehole 1 and borehole 3 (Eriksen et al., 2017a; Eriksen et al., 2017b; Henderson et al., 2010).

East of crack 1 is relatively undisturbed plateau. A tension crack (crack 2) is found oriented parallel with crack 1 here (figure 55A).

Crack 1 is the dominating feature in domain 3 as it controls the movement of the area. It has a main orientation striking NNE-SSW and is built up by the NW-SE and NE-SW oriented orthogonal joint sets. Ice is found in the crack all year around and the crack is at least 20 meters deep (see chapter 2.5). The crack becomes progressively wider towards the south (figure 55A

and 55B). The largest opening is around 10 m and the crack progressively decreases in width with depth.

North of crack 1 a heavily fractured area with tension cracks is present. The tension cracks are mainly oriented NW-SE and NE-SW, and the area is the outer part of the domain bound by a scarp to talus material in domain 1 below (figure 55A).

To the west of crack 1, a series of scarps and terraces are present (figure 55A). The scarps are oriented NNE-SSW in the upper most part and have a more NE-SW orientation further down. They also show a greater height towards the south, for the scarp below borehole 1 the height goes from 11 m in the north to 23 m in the south. The scarps both show a rounded and zig zagging surface shape. A greater width is seen in the southern ends of the terraces compared to the northern end. In the northern end, the terraces could "die out" in the meeting of two scarps, while they in the south measures up to 25 m in width. Bedrock with till-cover and rock fall deposits overlie the top of terraces. The largest terrace has open cracks aligned with the orientation of the scarps, and some tension cracks either parallel with these or oriented perpendicular (figure 55D). In the lowest reaches of the domain, scarps with a high vertical elevation difference mark a transition to talus and forest/vegetation below. The southern boundary of domain 3 is a NE-SW trending scarp which marks the transition to domain 4 (figure 55C). The scarp is dipping around 60 degrees towards NW.
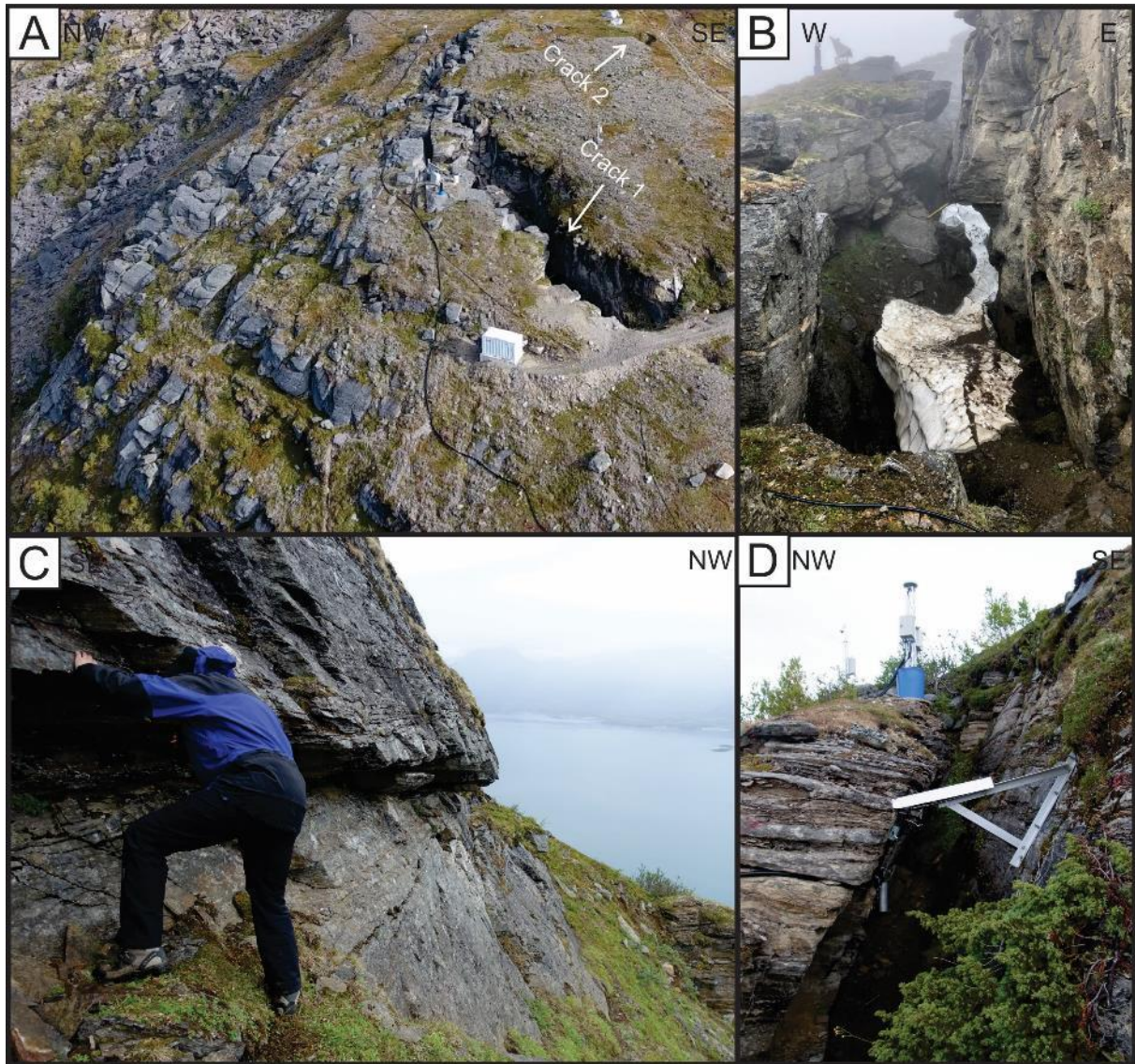
*Figure 55: Domain 3. A) Drone photograph of crack 1 and sub scarps. B) Field photograph showing the snow inside crack 1. C) Field photograph of the southern boundary sub scarp of the domain and movement seen on the foliation. D) Field photograph of an open crack between two terraces in the lower part of the domain.*

### 4.2.4  Domain 4

Domain 4 is the southernmost domain and is characterized by a large terrace at the top with subsequent scarps and terraces below. The movement rates recorded for the domain are not particular high and therefore no great interest has been taken in the domain in the past (Eriksen et al., 2017b).

The large terrace extends approximately 250 m in the N-S direction and around 150 m in the W-E direction (figure 56A). The terrace is covered by till and some rock fall deposits, and a

number of depressions (till-draped fractures) were found striking NE-SW (figure 56B). A small ridge in the north of the terrace has been interpreted as a moraine ridge with an orientation NW-SE (figure 56A) (Blikra & Christiansen, 2014). However, it is also possible that the ridge is a morphostructural feature, formed by uplift of a longitudinal structure under the till.

There is a distinct break between the relative flat terrace and the underlying scarp-terrace-scarp morphology. The dominating orientation of the scarps is N-S. The upper most scarps have a dominating zigzag pattern with joints orientated NW-SE and NE-SW, and have a smoothed surface with striae (could be either sliding or glacial processes) (figure 56C). Scarps further down show a larger height in the northern and southern end of the terraces, whereas in the middle part smaller scarps and till and talus covered bedrock is dominating. The lowermost scarps express the largest elevation drop and are the boundary to a shallower area in domain 7.

A large 150 m high NE-SW-oriented wall marks the outer limit of the URS to the south (figure 56D). It is aligned with the gully seen in connection to the NE-SW fault. At the time when the field investigation was done, no water was seen in the valley, but imbrication of loose material and erosional features gave signs of seasonal drainage. The southern section of the large wall branches into several sets of large scarps, bending to strike NW-SE. Beneath the wall, rock fall deposits fill the valley. Seepage was found in the upper eastern part of the wall, leaking out from a weaker layer in the garnet mica gneiss. This weak layer was interpreted as a lithological weak zone (see chapter 4.1.4) as it was foliation parallel and preferentially weathered (figure 57A and B). Calcite coating was observed on several joint surfaces in the large wall. It was seen to be connected with calcite marble layers in the top portion of the wall (figure 57C).
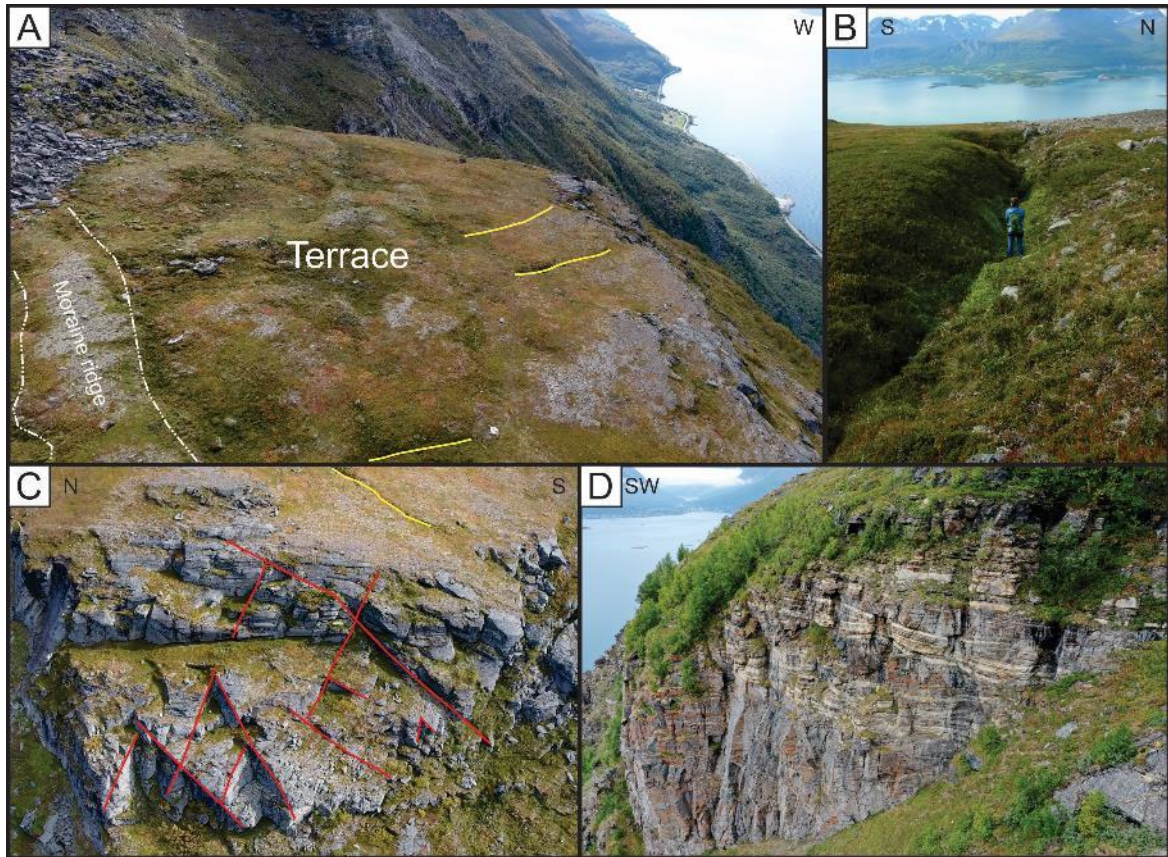
*Figure 56: A) Drone photograph showing the upper large terrace, the moraine ridge and depressions. B) Field photograph illustrating one of the depressions found on the large terrace. C) Drone photograph of the uppermost minor scarp with zigzag pattern from orthogonal joint sets. D) Drone photograph of the large wall towards the south, marking the outer limit of the URS.*



*Figure 57: Seepage found in the upper eastern part of the wall and calcite coating found on joint surface. A) Seepage here seen as frozen, coming out of the weaker zone (white stippled lines). B) Perpendicular display of the weaker zone (white stippled lines), which was traced to the seepage point. C) Calcite marble coating on a joint surface in the lower portions of the wall.*

### 4.2.5 Domain 5

Domain 5 is the upper most part of the URS. It is characterized by the V-shaped intersection of the NW-SE and NE-SW oriented backscarps (figure 58). It is also characterized by a large domed marble protrusion in the topography. High movement rates are found within a concentrated area of the domain, interpreted to be a rock glacier (Eriksen et al., 2017b).

The marble dome is the highest area of the URS, lying between 750 – 800 m. asl (figure 48 and 58A). The area is heavily fractured with gradually wider open fractures to the SE, closer to the fault trace. The larger fractures mark depressions in the terrain and the orientation of the depressions are bending north further to the NE. The big depressions are filled with till material and blocks, and smaller scarps is found as outer boundaries (figure 58B). In the south the fractures are largest, ranging up to 30 m in width and 3-4 m deep. Following the fracture traces north they gradually become smaller until they are seen as hairline fractures in the surface. In the central section of the dome, tension cracks oriented NW-SE and NE-SW are several meters deep, but they do not show openings as large as those found to the east (figure 58D).

Below the backscarps, broken dolomite and gneiss talus material dominates, and a parallel depression is found beneath both backscarps (58C). At the upper part of the backscarps smaller outcrops of bedrock are exposed. The scarps have a close to vertical dip whilst the overall slope has a dip between 45-55°. The area in between the two backscarps appear to have been moved down towards W/WNW. From NW to SE the NW-SE striking backscarp starts in a morphological depression formed by two smaller scarps, advances through the talus dominated area and ends up in the meeting of the other backscarp in a smaller scarp with calcite marble (figure 53).

The NW-SW trending backscarp has been interpreted as a fault, from findings of slickenslides on outcrops, as there was both found a lithological offset in field and seen on NGU's bedrock map (figure 4), and from the fact that other liniments in the area with same orientation has been interpreted as faults. The fault is interpreted to crosscut the entire Nordnes Mountain. From where it meets the other backscarp it continues straight towards SW for 300 m before the scarp bends striking perpendicular to the fault. At this point the backscarp proceeds south into Midtre Nordnes (figure 53). The fault is thought to continue SW. In the intersection of Jettan and Midtre Nordnes a large scarp with a zig zagging appearance (joints oriented NW-SE and NE-SW) is present having a drop of approximately 18 m. Beneath the scarp a large open fracture

filled with rock fall deposits and disintegrated blocks is found. In front of the fracture four columns arises seen in connection to the opening of the large fracture between the scarp and the columns. White coating of calcite was found on the joint surface in the large scarp.

The large rock glacier to the NW is mainly built up by dolomite marble blocks. No typical lobe morphology is expressed, and the rock glacier is essentially interpreted as on because of movement rates (see chapter 2.8). A second smaller rock glacier was found below the fault backscarp. The rock glacier has been interpreted from morphological ridges oriented orthogonal to the movement direction (figure 58C and 59). In the northwest of the domain two morphological depressions form two small NW-SE striking valleys with scarps on each side. To the west, minor scarps striking N-S, aproned by talus material below, form a distinct change into to the plateau of domain 2 and 4.
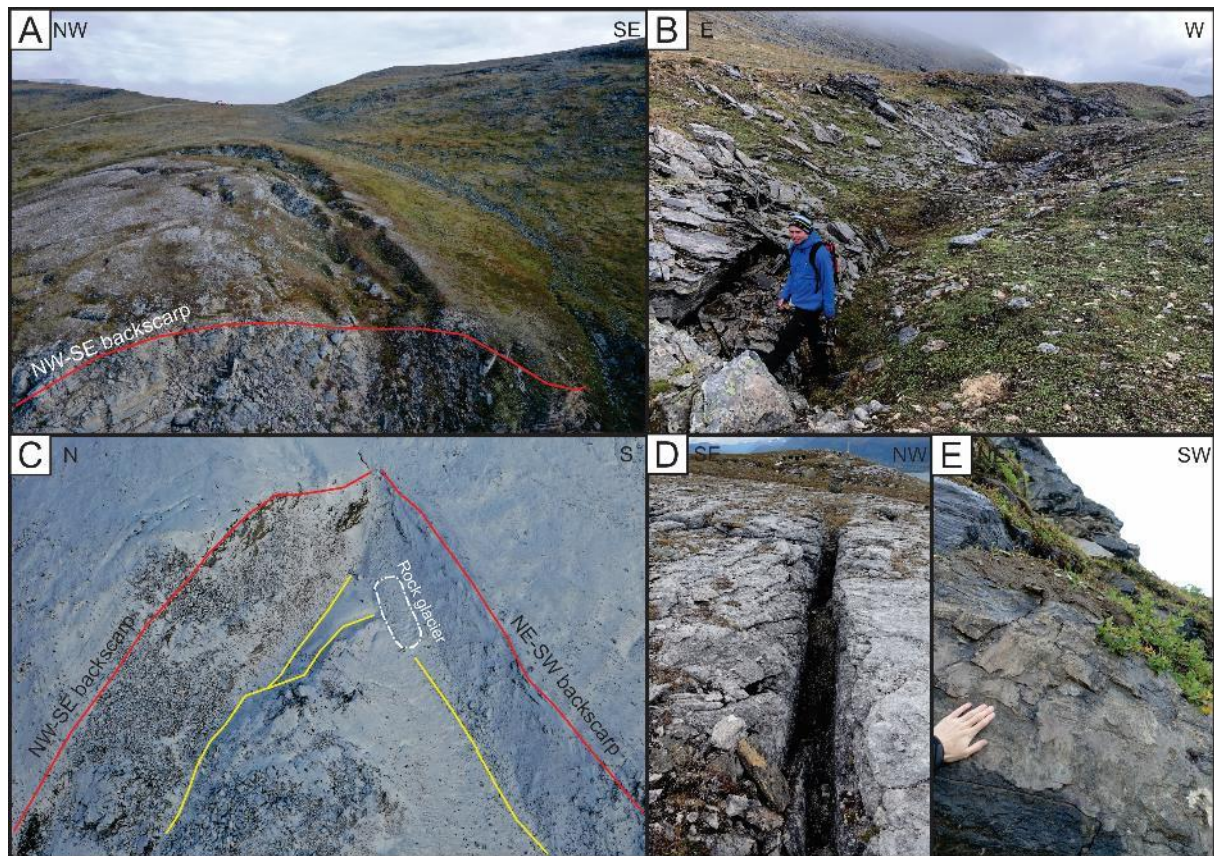


*Figure 58: Domain 5. A) Drone photograph of the upper most area of the URS. Depressions and tension cracks. B) Filed photograph illustrating the outer most depression. C) Drone photograph showing the meeting of the two backscarp making a V-shape. Depressions is marked as yellow lines, and the rock glacier is marked with white polygon. D) Field photograph of a tension crack in the middle upper part. E) Field photograph of slickensides on the fault plain.*

*Figure 59: Drone photograph of the rock glacier with dotted lines along the ridges.*

### 4.2.6 Domain 6

Domain 6 includes the lower northernmost parts of the URS, an area characterized by historic avalanche and rockfall deposits (figure 60). The domain stretches from between 400 - 450 m asl to toe level. There are no observable intact displaced blocks or scarps. From the hillshade map (figure 51), it is clear that the domain is dominated by deposits, supporting the theory that this is an old avalanche deposit. On top of the avalanche deposit several rock fall deposit paths could be traced downslope (figure 60). In the lower western parts of the domain, large scarps interpreted as frontal lobes of the old avalanche deposit are found. The height of the frontal lobes was observed to have been a maximum height of 45 m. The lobes expressed higher elevation drop in the north and a gradually lower drop towards south.

*Figure 60: Domain 6. Drone photograph of talus and avalanche deposits (lobe marked with white dotted lines).*

### 4.2.7  Domain 7

Domain 7 encompasses the southwestern lower area of the URS, and it is characterized by two larger terraces covered in rockfall and talus material and some larger scarps.

The upper most terrace is approximately 300 m long and 260 m wide, and the dip gets gradually more gentle down slope from 40° to 23° until it reaches a larger scarp (figure 61A). The large scarp has a height of between 20 and 60 m, with the largest elevation in the middle of the domain. Below the larger scarp, talus material is found in the south and a new terrace in the north. The lowermost terrace is 150 m long and 115 m wide, with a surface dip of around 25°. A 40 m high scarp marks the lower boundary of the terrace and a talus covered area below. In the scarps sub vertical tension cracks were observed, thought to follow the foliation or lithological weak zones as sliding planes at the base (figure 61B). No lithological weak zones were observed at the surface however. Calcite coating on the joint surfaces were found in several locations, but no calcite marble was observed in domain 7, suggesting that some fluid flow from higher areas exits from the foliation or joints in the lower areas (figure 61C).
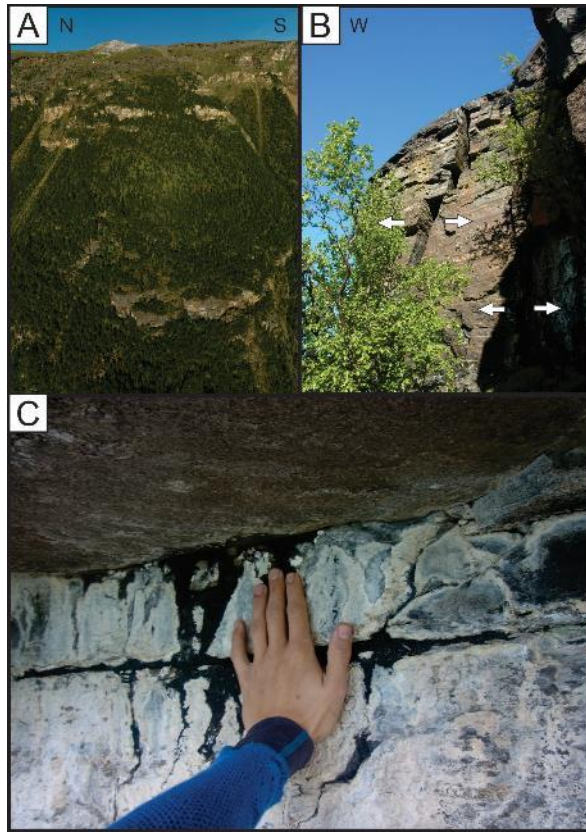
*Figure 61: Domain 7. A) Uppermost terrace and the large scarp below. B) Field photograph of vertical tension cracks opening towards the fjord. C) Field photograph illustrating calcite coating on joint surface. (Reference picture A)*

## 4.3  Movement

In the following chapter, an overview of movement measured by the various instruments installed at Jettan will be presented. In a later section of the chapter, the weather and climate records will be discussed in relation to the movement found from the continuous monitoring.

## 4.3.1 Continuous monitoring data
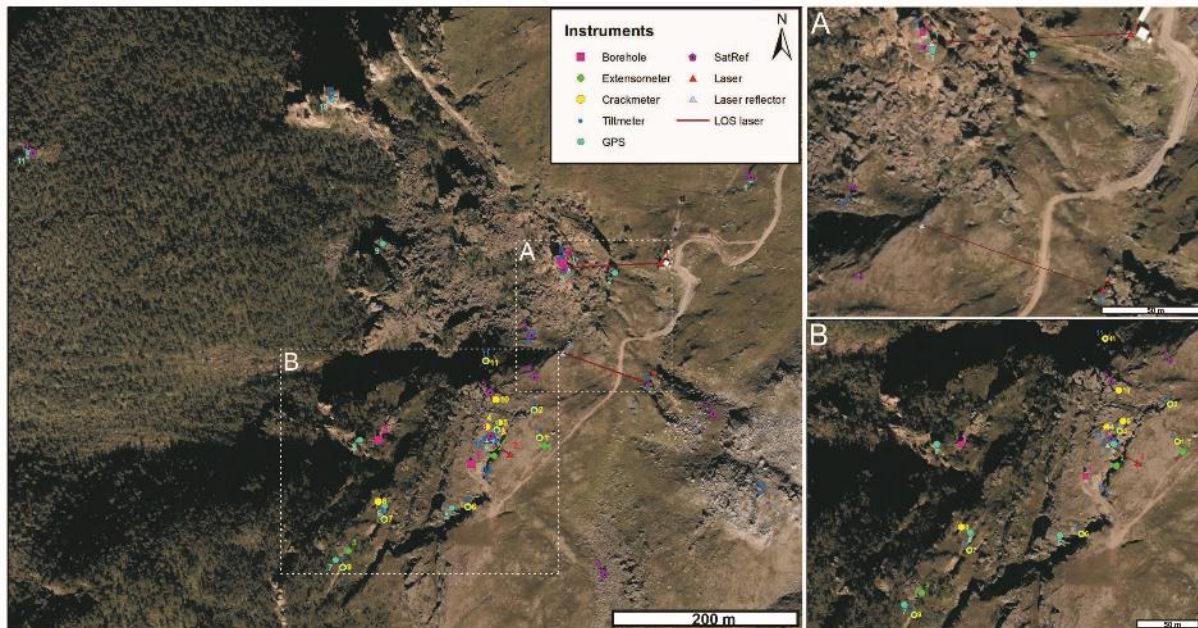


*Figure 62: Position of the different continuous monitoring instruments at Jettan. Number indicates which instrument. Insets A and B are located in the left panel. LOS is referred to as line of sight for the lasers and SatRef is referred to as satellite reference (NVE, 2019).*
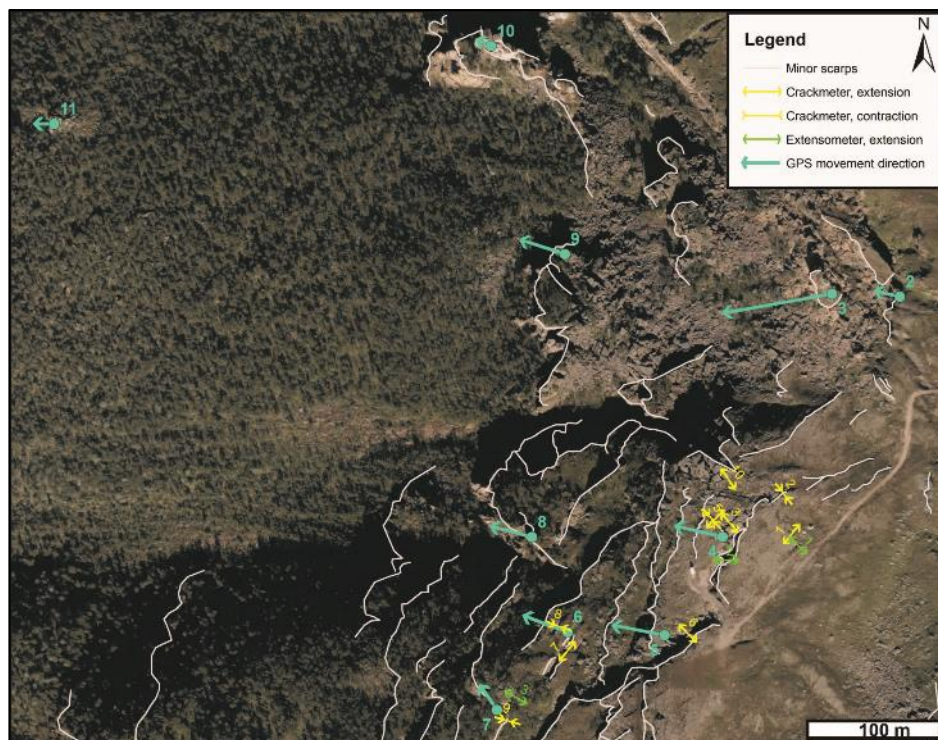


*Figure 63: Overview of movement vectors for GPS's and orientation of extensometers and crackmeters showing contraction or extension. Movement vector express average mm/year.*

### 4.3.1.1 Extensometers

The location of the extensometers is shown in figure 62. In table 7 an average of the yearly compression, extension and movement is present from 2011-2018. All three extensometers show variation in movement linked with seasonal variations (figure 64).

*Table 6: Registered average compression, extension, movement and direction (NVE, 2019).*

| Extensometer | Average compression (mm/yr) | Average extension (mm/yr) | Average movement (mm/yr) | Movement direction |
|---:|---:|---:|---:|---|
| 1 | 2,11 | 4,13 | 2,03 | ~NW-SE |
| 2 | 4,40 | 18,86 | 14,83 | ~W-E |
| 3 | 1,56 | 2,36 | 0,80 | ~W-E |

Extensometer 1 has an extensional phase from around September to May/June, from May/June compression occurs until the start of August, and from August to September records show little or no movement. Extensometer 2 has small variations in movement rates with a steady high extension and no compression until 2015. From 2015 a yearly compression phase is seen in winter around January (figure 64). This is the extensometer at Jettan with the highest movement values. Extensometer 3 is recorded to have extension from around mid-July to April/May, with highest values in the first months before it decreases. From April/May compression lasts until the middle of July.
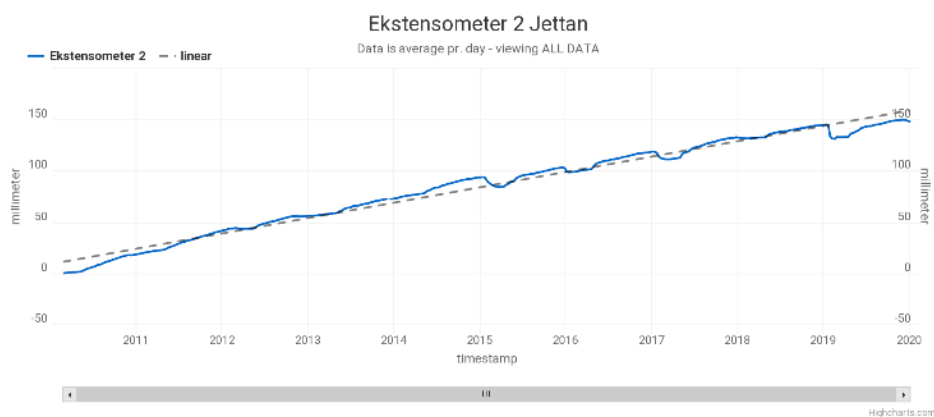


*Figure 64: Registered movement for extensometer 2 and linear trend (NVE, 2019).*

### 4.3.1.2 Lasers

The location of the lasers and laser reflectors are found in figure 62. Laser 1 measures the distance between the stable area at the field station to a dislocated block (block 2) in domain 1 (figure 65). Laser 2 measures the opening of crack 1 in domain 3 and laser 3 measures from the lower northern part of domain and across the middle plateau in domain 2. Laser 1 has the largest average movement of almost 40 mm a year (table 8). Laser 3 shows the lowest average movement of only 6 mm a year.

*Table 7: Average compression, extension and movement for the laser at Jettan.*

| Laser | Average compression (mm/yr) | Average extension (mm/yr) | Average movement (mm/yr) |
|---|---|---|---|
| 1 | 9.67 | 49.31 | 39.64 |
| 2 | 15.16 | 25.18 | 10.02 |
| 3 | 15.17 | 21.27 | 6.10 |
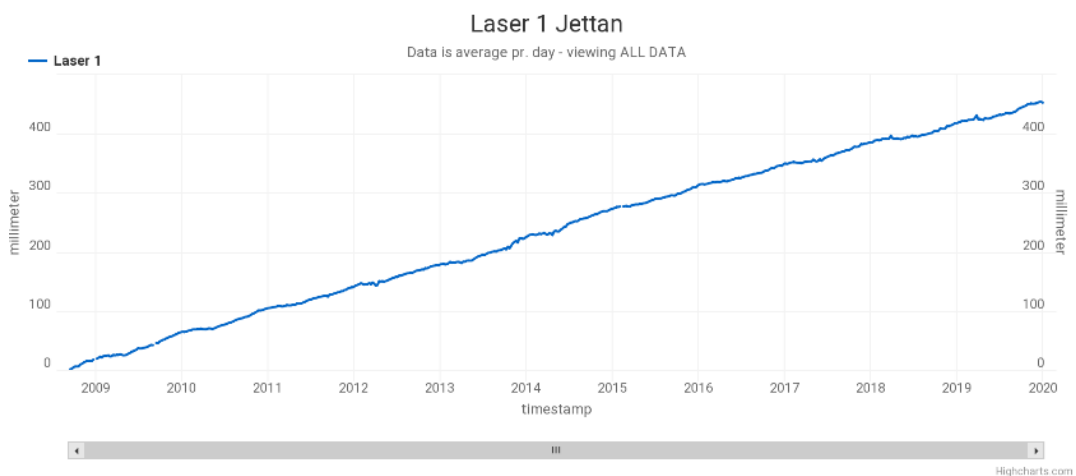


*Figure 65: Registered movement for laser 1 (NVE, 2019).*

### 4.3.1.3 Crackmeters

The location of the crackmeters is shown in figure 62. Crackmeter 1, 3, 4, 6, 7, 10 and 11- show a positive average yearly movement (table 9), meaning that the crack is opening (extension). The highest extension is seen at crackmeter 3, showing an average of 6 mm/yr. Crackmeter 2,

5, 8 and 9- show a negative average yearly movement (table 9); meaning that the crack is contracting (compression). The highest compression is seen at crackmeter 9 with a value of -1,74 mm/yr. The movement direction is based on the orientation of the crack where it is mounted, however this may deviate if the crackmeter is not mounted perpendicular to the crack.

*Table 8: Yearly average movement for the different crackmeters at Jettan. Data from (NVE, 2019)*

| Crackmeter | Average movement (mm/yr) | Movement direction |
|---|---|---|
| 1 | 0.47 | ~SW-NE |
| 2 | -0.84 | ~NW-SE |
| 3 | 6.00 | ~NW-SE |
| 4 | 0.35 | ~SW-NE |
| 5 | -0.03 | ~NW-SE |
| 6 | 1.17 | ~NW-SE |
| 7 | 0.71 | ~NNE-SSW |
| 8 | -0.28 | ~NW-SE |
| 9 | -1.74 | ~WNW-ESE |
| 10 | 2.77 | ~NNW-SSE |
| 11 | 7.60 | - |

Seasonal variations are seen in all of the crackmeters; periods with extension, compression or periods with little or no movement. Extension is starting in the autumn lasting into early to midwinter where it shows no or little movement. In the spring, a compressional phase is initiated lasting until late summer/autumn.

### 4.3.1.4 GPS

Location of the GPSs is found in figure 62 and movement vector in figure 63. The movement of the GPSs is seen in table 10, showing the average annual movement. In the N/S direction, positive values express movement towards N, in the E/W direction negative values express

movement towards W and negative movement for the height means downward movement. GPS 3 stands out from the others by showing the largest displacement and being the only GPS moving towards south (WSW) (table 10). All the rest of the GPSs show a movement towards WNW.

Table 9: GPS movement at Jettan, showing yearly average movement in N/S, E/W, height direction, dip and dip direction, horizontal movement and total movement (NVE, 2019).

| GPS | N/S movement (mm/yr) | E/W movement (mm/yr) | Height movement (mm/yr) | Dip | Direction | Horizontal movement (mm/yr) | Total movement (mm/yr) |
|-----|-----|-----|-----|-----|-----|-----|-----|
| 2 | 1,75 | -7,02 | -3,47 | 26 | 283 | 6,83 | 7,37 |
| 3 | -7,53 | -37,05 | -14,91 | 21 | 260 | 36,48 | 39,05 |
| 4 | 2,78 | -12,77 | -10,56 | 38 | 283 | 12,33 | 15,91 |
| 5 | 2,23 | -11,25 | -14,16 | 50 | 281 | 10,68 | 17,46 |
| 6 | 3,73 | -8,81 | -12,29 | 52 | 290 | 8,81 | 15,29 |
| 7 | 3,07 | -2,45 | -6,74 | 51 | 325 | 3,77 | 8,76 |
| 8 | 3,84 | -11,91 | -6,25 | 24 | 285 | 11,97 | 13,58 |
| 9 | 3,82 | -10,00 | -10,35 | 41 | 288 | 10,11 | 15,15 |
| 10 | 1,90 | -2,21 | -2,33 | 34 | 294 | 2,77 | 3,50 |
| 11 | 0,22 | -0,78 | -3,56 | 53 | 270 | 0,70 | 5,18 |

### 4.3.2 InSAR

InSAR point data at Jettan is presented in map view together with backscarps, displaced blocks and the different domain divisions (Figure 66). Displacement is shown in LOS in mm per year. Therefore, downward displacement is expressed as negative values (red colors) and upwards displacement is expressed as positive values (blue colors).

The highest velocities are seen in domains 1 and 3. In domain 1 the displacement rates are measured to be up to -29 mm/yr, while the average lies from -17 to -25 mm/yr (figure 66). High negative displacement rates are also found west of the displaced blocks of domain 1, in the talus area, where the average is -12.4 mm/yr. In domain 3 the largest displacement rates are seen west of crack 1, with different movement rates delineated by terrace edges. Domain 4 shows little movement, with -1.2 mm/yr on the plateau. One area of higher deformation is seen in domain 5, which displays a downward displacement of -7.1 mm/yr (seen as the orange color in the middle part of domain 5). These different areas with higher displacement rates correspond well with what was found by Eriksen et al. (2017b).
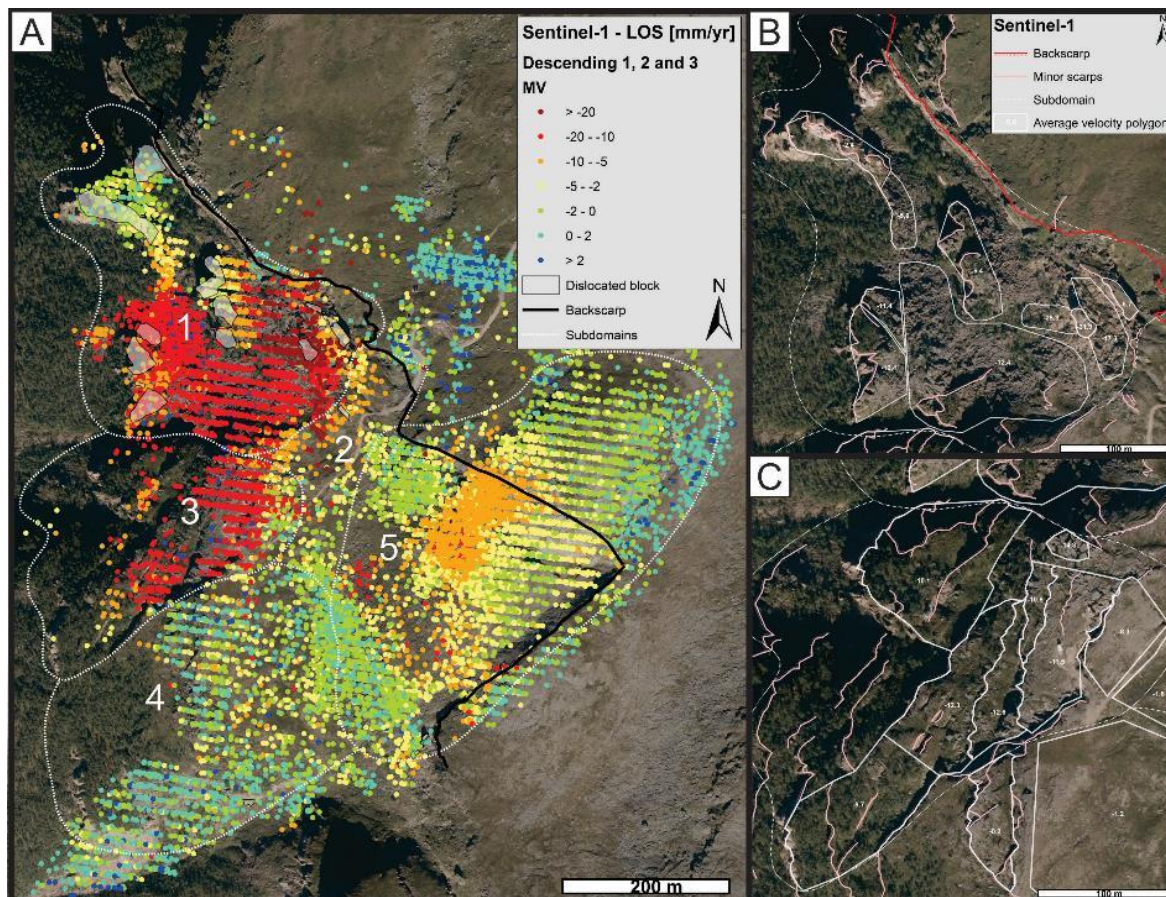
*Figure 66: Displacement measured by the Sentinel-1 satellite. A) Showing the displacement for the whole area at Jettan with the different domains marked along with the backscarp and displaced blocks. B) Polygons in domain 1 showing average displacement per year. C) Polygons in domain 3 and 4 showing average displacement per year (NGU, 2020).*

## 4.4  3D model

In the following chapter the inputs to the 3D model will be presented followed by the bedrock and the failure scenario model. Cross-sections together with an overview picture will give a great insight of the 3D models. In the appendix a free software and a link to download the model is attached for a better visualization of the 3D models.

### 4.4.1  Borehole inputs to the model

The borehole logs were recomposed to table 11, 12 and 13 to present the following characteristics: weathering, crushed zones, core loss, faults, foliation and joint zones. This data was gathered based on reports by Elvebakk (2013), Elvebakk (2014), Ganerød (2013) and

Ganerød (2014). The "m" in the tables refer to meters below ground level. The "from" and "to" columns are intervals based on the lithology in the different boreholes, the "lithology" column refers to logging by Ganerød (2013) and Ganerød (2014). The "leapfrog lithology" column refers to mapping from this thesis and used in the 3D model. Lithologies in Leapfrog have been simplified for an easier modelling. The lithological sequences combining marble and mica schist from Ganerød (2013) and Ganerød (2014) logging is similar to what seen as the calcite marble sequences in the field, with interbedded calcite marble and garnet mica gneiss, and is therefore put as marble in Leapfrog. The "Foliation" column describes sections where foliation was encountered dipping above 31° (chapter 2.9, friction angle), and the dip direction is out of the slope (between 180-360°). The "Joint zones" column is where joints or zones of joints have a dip out of the slope (190-360°).

### 4.4.1.1 Borehole 1

Table 10: Lithologies in borehole 1 with weathering, crushed zones, core loss, fault, foliation and joint zones.

| From [m] | To [m] | Lithology | Leapfrog lithology | Weathering | Crushed zones | Core loss | Fault | Foliation | Joint zones |
|---|---|---|---|---|---|---|---|---|---|
| 0 | 41.6 | BGMS | GMG | - | CCR+CR=27-41.6m(13 zones) | 0-1.35m (1.35m) | - | - | FPJ~20-40m(~20/270) |
| 41.6 | 53 | MGMS | CM | IM=43.6m | CR=41.8-44.4m(3 zones) PC=42.8m | - | 45.2-45.5m | 41.8m(38/281) 44.3-45.6m(~49/281) | ~45m(~35-60/270-285) |
| 53 | 65 | BGMSM | CM | IM=61.8m | - | - | - | 53.9m(41/340) 55.4m(31/313) 57.7m(31/303) | - |
| 65 | 77 | BGMS | GMG | IM=65m, 68.4m, 72.4m | - | - | - | - | - |
| 77 | 80.5 | BMSM | GMG | IM=79.7m | - | - | - | - | - |
| 80.5 | 89.3 | BGMS | GMG | WR+IM=82m, 88.2m, 88.6m | CCR=81m(10cm) | - | - | - | - |
| 89.3 | 100.8 | MSM | CM | - | - | - | - | - | - |
| 100.8 | 103.75 | BGMS | CM | - | - | - | - | - | - |
| 103.75 | 115.3 | MSM | CM | WR+IM=105.7m | CR=111.5m(15cm) HCR=115.1m(25cm) | - | - | - | - |
| 115.3 | 125 | BGMS | GMG | - | - | - | - | - | - |
| 125 | 128.8 | MGMS | GMG | - | - | - | - | - | - |
| 128.8 | 156.8 | M | CM | WR+IM=148.5m, 151.5m, 156.8m WR=154.3m | CR=130.5m(10cm) CCR=150.1m(10cm) | - | - | - | - |

| From [m] | To [m] | Lithology | Leapfrog lithology | Weathering | Crushed zones | Core loss | Fault | Foliation | Joint zones |
|---|---|---|---|---|---|---|---|---|---|
| | | | | | CCR=151m(80cm) PC=151.5m | | | | |
| 156.8 | 180 | MSM | CM | WR+IM=170.7m WR=174.2m | CCR+CR=157.3-165.9m(8 zones) CCR=173.3m(20cm), 177.6-179.5m(3 zones) PC=161.4m | - | - | 164.9m(38/219) 173.6-173.8m (~32/289.5) | 165m(~40/270) 175m(~35/280) |
| 180 | 191.6 | MMS | CM | IM=190.4m | CCR=180.7m(50cm) | - | - | - | - |
| 191.6 | 198.8 | M | CM | - | - | - | - | - | - |

*Lithology: BGMS = Banded Garnetiferous Mica Schist, MGMS = Marble with layers of Garnetiferous Mica Schist, BGMSM = Banded Garnetiferous Mica Schist with layers of Marble, BMSM = Banded Mica Schist with layers of Marble, MSM = Mica Schist with layers of Marble, MMS = Marble with layers of Mica Schist, IMMS = Interbedded Marble and Mica Schist, MS = Marble with layers of Schist, M = Marble, GMG = Garnet Mica Gneiss, CM =Calcite marble.* **Weathering:** *WR = Weathered Rock, HWR = Highly Weathered Rock, IM = Iron Mineralization.* **Crushed zones:** *CCR = Coarsely Crushed Rock, CR = Crushed Rock, HCR = Highly Crushed Rock, FCR = Finely Crushed Rock, C = Clay, PC = Possibly Clay.* **Joint zones:** *FPJ = Foliation Parallel Joints.*

In borehole 1, a number of zones show characteristics implying that they could reduce the stability of the URS. Firstly, foliation parallel joints at 20-40 m bgl dipping towards west around 20°, plus coarsely to crushed rock in 13 zones at 27-41.6m bgl. Secondly, a fault at 45.2-45.5 m bgl, foliation dipping towards the fjord (281°) at 49°, and a joints zone dipping from 35-60° towards the fjord (270-285°). Third, highly crushed rock at 115.1 m bgl with a thickness of 25cm. Fourth, coarsely crushed rock at 151 m bgl which is weathered and contains iron mineralization plus possibly clay. Fifth, foliation dipping 38° towards SSW (219), and a joint zone dipping ~40° towards west at 165m bgl. Sixth, coarsely crushed rock at 173.3m (20cm) and foliation at 173.6-173.8 dipping 32° towards west (290).

### 4.4.1.2 Borehole 2
*Table 11: Lithologies in borehole 2 with weathering, crushed zones, core loss, fault, foliation and joint zones.*

| From [m] | To [m] | Lithology | Leapfrog lithology | Weathering | Crushed zones | Core loss | Fault | Foliation | Joint zones |
|---|---|---|---|---|---|---|---|---|---|
| 0 | 3.5 | BGMS | GMG | WR+IM=2.6-3.0m | CCR=2.3m(8cm) HCR=2.6-3.4m | 0-0.46m (46cm) | - | - | - |
| 3.5 | 4.1 | M | CM | HWR=3.6m(8cm) | - | - | - | - | - |
| 4.1 | 67.5 | BGMS | GMG | IM=22 locations WR=7.8m, 20.4m, 21.4m, 35.6m | CCR=24.5-27.2m(5 zones) 56.5-57m(30cm), 61.4m(10cm) CCR+CR=38-53m(20 zones) FCR=46.7m, 52.8m(20cm) C=44.7m(1cm), 45.7m(6cm), | 24.6-27m (87cm), 36.6-50.7m (4.33m) | - | 27.5-27.8m(~37/212) 29.7-30m(~35/210) 30.2m(35/222) 30.5-52.4m(~46/244) 56.4m(32/270) | 24.4-25.3m(47/319) 39.9-40m(81/275) 42.3-44.4m(38/276) |

| | | | | | 52m(5cm), 52.8m(20cm) 53m(11cm) | | | | |
|---|---|---|---|---|---|---|---|---|---|
| 67.5 | 68.2 | M | CM | - | - | - | - | - | - |
| 68.2 | 73.5 | BGMS | GMG | IM=72.5m, 73.5m | - | - | - | - | - |
| 73.5 | 74.7 | M | CM | - | - | - | - | - | - |
| 74.7 | 75.4 | BGMS | GMG | IM=75.3m | - | - | - | - | - |
| 75.4 | 76.3 | M | CM | - | CCR=75.4m(12cm) FCR=75.5m(13cm) | - | - | 76m(36/225) | - |
| 76.3 | 79.7 | BHMS | GMG | IM=79.2m | - | - | - | - | - |
| 79.7 | 83.9 | MS | CM | IM=81.8m, 82.1m, 82.2m, 83.2m, 83.3m | - | - | - | 80.2m(31/213) 82.8m(32/273) | - |
| 83.9 | 98.08 | BMSM | CM | IM=12 locations | FCR=89.9m(10cm), 90.3m(13cm) CCR=90.4m(20cm), 92.9-93m | - | ~90m (30cm) | 96.5m(~38/274) | 89.5-90.5m(65/305) |

*Lithology: BGMS = Banded Garnetiferous Mica Schist, MGMS = Marble with layers of Garnetiferous Mica Schist, BGMSM = Banded Garnetiferous Mica Schist with layers of Marble, BMSM = Banded Mica Schist with layers of Marble, MSM = Mica Schist with layers of Marble, MMS = Marble with layers of Mica Schist, IMMS = Interbedded Marble and Mica Schist MS = Marble with layers of Schist, M = Marble, GMG = Garnet Mica Gneiss, CM =Calcite marble. Weathering: WR = Weathered Rock, HWR = Highly Weathered Rock, IM = Iron Mineralization. Crushed zones: CCR = Coarsely Crushed Rock, CR = Crushed Rock, HCR = Highly Crushed Rock, FCR = Finely Crushed Rock, C = Clay, PC = Possibly Clay. Joint zones: FPJ = Foliation Parallel Joints.*

In borehole 2, a number of zones show characteristics implying that they could reduce the stability of the URS. Firstly, coarsely crushed rock and core loss at 24.5-27.2m bgl. Secondly, a large zone of coarsely crushed rock to finely crushed rock (FCR= 46.7m and 52,8m) at 36.6-53m bgl, including zones of core loss and clay. Foliation in this zone has an average dip on 49° with an average dip direction towards WSW. There are also joint zones with favorable orientation at 39.9-40 m bgl (81/275) and 42.3-44.4m bgl (38/276). Third, finely crushed rock at 75.5 m bgl (13 cm thick) and foliation dipping 36° towards southwest (225°) at 76 m bgl (close to the finely crushed rock zone). Fourth, finely crushed rock at 89.9 m bgl (10 cm thick) above, old fault at ~89.95-90.40 m bgl (~30 cm thick) middle, and a finely crushed rock at 90.3 m bgl (13 cm thick) below.

### 4.4.1.3 Borehole 3
*Table 12: Lithologies in borehole 3 with weathering, crushed zones, core loss, fault, foliation and joint zones.*

| From [m] | To [m] | Lithology | Leapfrog lithology | Weathering | Crushed zones | Core loss | Fault | Foliation | Joint zones |
|---|---|---|---|---|---|---|---|---|---|
| 0 | 5.5 | MSM | CM | IM=3.3m, 3.6m | - | 0-2.5m(2.5m), 4m(45cm) | - | - | - |

| From (m) | To (m) | Lithology | | Weathering | Crushed zones | | | | Joint zones |
|---|---|---|---|---|---|---|---|---|---|
| 5.5 | 8.4 | BGMS | GMG | - | CCR=5.5m(10cm) | - | - | - | - |
| 8.4 | 9.4 | M | CM | IM=8.5m | - | - | - | - | - |
| 9.4 | 10.7 | BGMS | GMG | - | CCR=9.5m(10cm) | - | - | - | - |
| 10.7 | 11.5 | M | CM | - | - | - | - | - | - |
| 11.5 | 12 | BGMS | GMG | - | CCR=11.9m(5cm) | - | - | - | - |
| 12 | 17.4 | IMMS | CM | IM=15.5m | CCR=12.5m(10cm), 15.4m(8cm), 15.9m(15cm) | 12-12-5m(45cm) | - | - | - |
| 17.4 | 43.4 | BGMS | GMG | IM=29.1m(5cm), 32.5m(20cm), 35.6m(10cm), 38.2m(30cm) + 6 locations | CCR+CR=24-26.1m (4 zones) CCR=27.4-36m(5 zones) CCR+CR=36-43m(8 zones) | 24.8-26.7m(50cm) 30m(22cm) 42.3-42.7m(40cm) | - | - | 24.1-24.4m(31/220) 29.8-31m(49/256) 36-36.15m(30/278) |
| 43.4 | 45.2 | M | CM | IM=44.5m | CCR+CR=43.4-45.2m (66cm) | - | - | - | - |
| 45.2 | 46.5 | BGMS | GMG | - | CCR=45.2-46m(50cm) | - | - | - | - |
| 46.5 | 72 | M | CM | IM= 7 locations | - | - | - | - | 50.1-50.2m(60/345) 69.8-71.2m(54/336) 71.2-72.6m(42/352) |
| 72 | 74.4 | MMS | CM | - | CCR=72m(10cm), 72.4m(20cm) | - | ~72.1-72.3m | - | - |
| 74.4 | 83.4 | BGMS | GMG | - | CCR=74.8-77.3m(5 zones), 79.3-82.6m(4 zones) FCR=80.8-81.1m PC=80.8-81.1m(30cm) C=81.2m | 76.3-76.6m(30cm) | - | - | 78.7-79m(34/330) |
| 83.4 | 86.2 | M | CM | IM=85.6m | - | - | - | - | - |
| 86.2 | 90.9 | BGMS | GMG | - | - | - | - | - | - |
| 90.9 | 100.94 | MMS | CM | - | CCR=91.7m | - | - | - | - |

*Lithology: BGMS = Banded Garnetiferous Mica Schist, MGMS = Marble with layers of Garnetiferous Mica Schist, BGMSM = Banded Garnetiferous Mica Schist with layers of Marble, BMSM = Banded Mica Schist with layers of Marble, MSM = Mica Schist with layers of Marble, MMS = Marble with layers of Mica Schist, IMMS = Interbedded Marble and Mica Schist MS = Marble with layers of Schist, M = Marble GMG = Garnet Mica Gneiss, CM =Calcite marble. Weathering: WR = Weathered Rock, HWR = Highly Weathered Rock, IM = Iron Mineralization. Crushed zones: CCR = Coarsely Crushed Rock, CR = Crushed Rock, HCR = Highly Crushed Rock, FCR = Finely Crushed Rock, C = Clay, PC = Possibly Clay. Joint zones: FPJ = Foliation Parallel Joints.*

In borehole 3, a number of zones show characteristics implying that they could reduce the stability of the URS. Firstly, coarsely to crushed rock at 24-26.7 m bgl with two zones of core loss (50 cm combined), and additionally a joint zone at 24.1-24.4m (31/220). Secondly, core loss at 42.3-42.7m bgl with coarsely to crushed rock below down to 46 m bgl. Third, old fault at ~72.1-72.3m with coarsely crushed rock above and below. Fourth, finely crushed rock at 80.8-81.1m bgl with possibly clay inside, and a small clay lens plus a coarsely crushed rock below.

## 4.4.2 Results from 3D modeling

### 4.4.2.1 Lithology model

The lithology model is shown in figure 67 and cross sections through the boreholes in figure 68, 69 and 70. The borehole lithologies could be seen in figure 71. The bedrock map suggests that the different lithological units are seen as bands through the whole area. This matches with the layers of boreholes 1 and 3, while domain 1, 6 and outside the unstable area show poor correlation compared to field investigations (see chapter 4.1.7). Cross-section DD' shows how the dolomite marble is expressed both in the dome (domain 5) and in Jettankallen (domain 1). Limitations of the model is a wrong offset of the lithologies when the fault was activated (figure 70), and that the model have garnet mica gneiss in the large fractures in the dolomite marble dome which was not observed in field (figure 69).
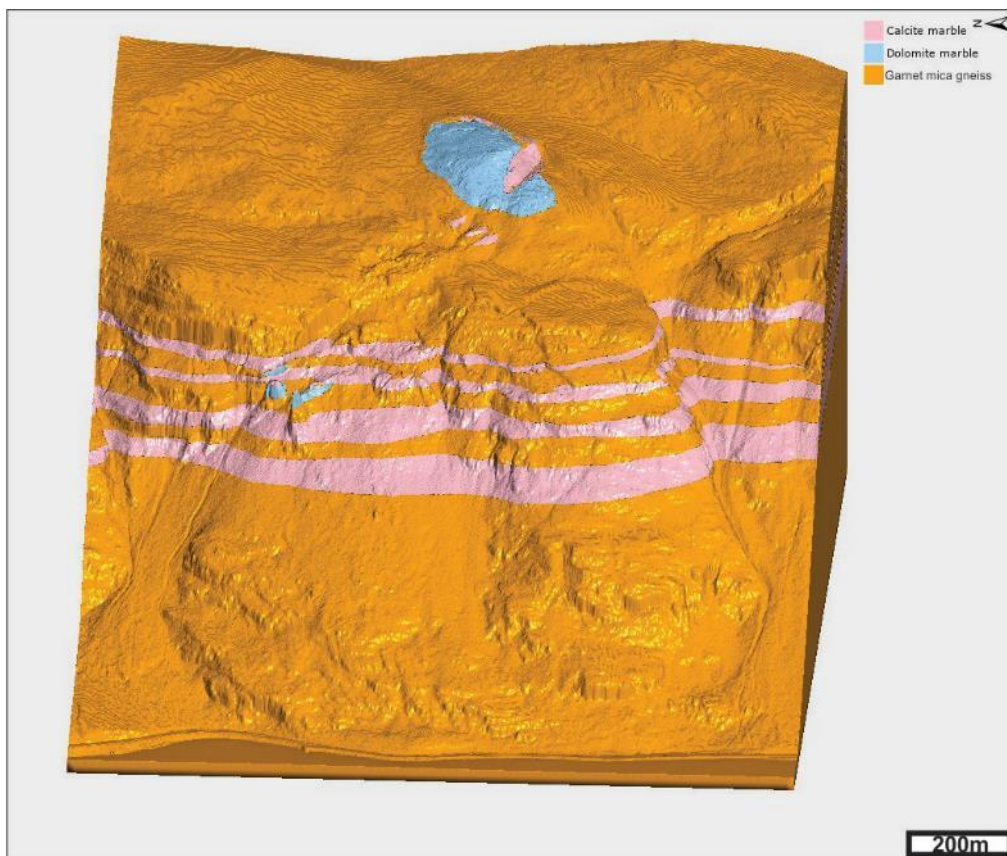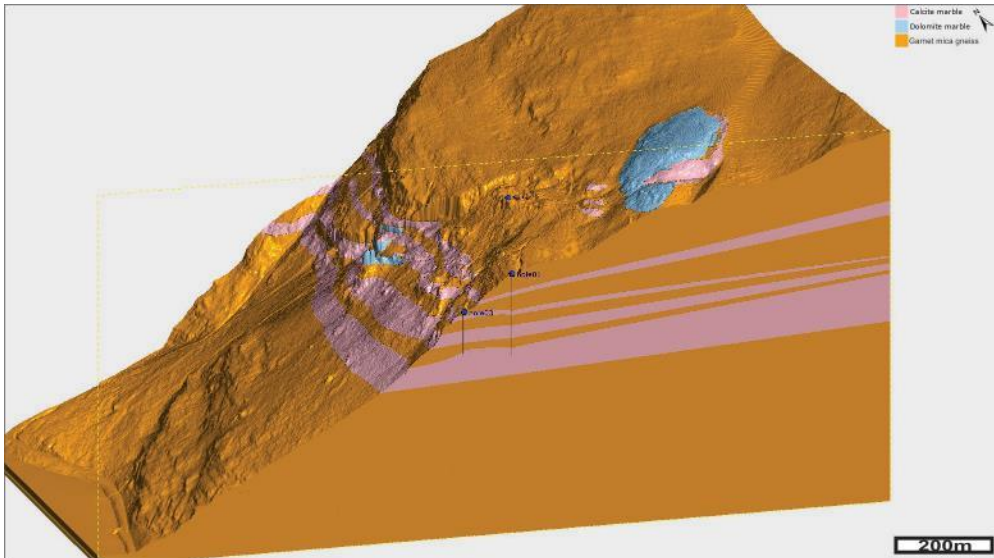


*Figure 67: Lithology model of Jettan.*

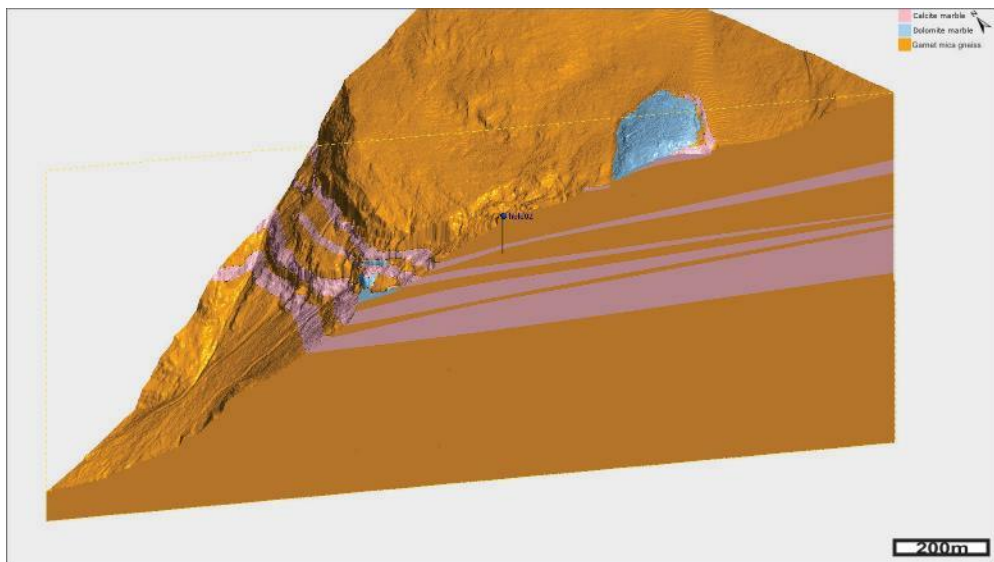*Figure 68: Cross-section of lithology model cutting borehole 1 and borehole 3.*



*Figure 69: Cross-section of lithology model cutting dolomite marble dome, borehole 2 and Jettankallen.*
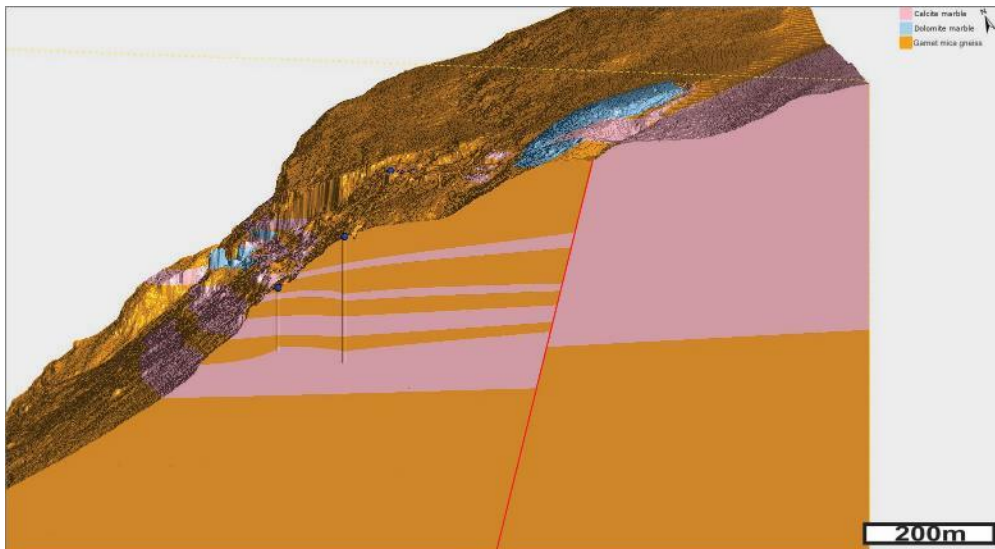
*Figure 70: Cross-section of lithology model including fault (red line) cutting borehole 1 and borehole 3.*



*Figure 71: The different lithologies in the boreholes at Jettan.*

### 4.4.2.2 Sliding surfaces

From table 11, 12 and 13 boreholes were made including core loss, crushed zones and faults (figure 72). Sliding surfaces were based on these weaker zones including the dip and dip direction for foliation, joint and faults at the specific depth, and from this a plane was made. All outcrops where structural measurements were taken from was put in the model as plains. The sliding planes combined with outcrop planes made a skeleton for different sliding surfaces.
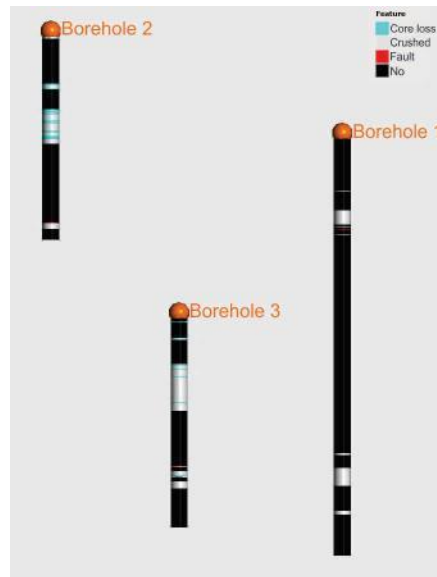
*Figure 72: Borehole 1, 2 and 3 showing core loss (blue), crushed zones (grey), fault (red) and relatively intact rock (black).*

In borehole 2 three main weaker zones gave the design of at least 3 possible sliding surfaces. Including that there were found variable dip for a crushed zone and a possibility of a larger extent of the sliding planes, there were in total made 6 possible sliding surfaces going through borehole 2 in domain 1 (figure 73). Although they are all going through the borehole in the three main weaker zones.



*Figure 73: Sliding surfaces in domain 1 going through borehole 2.*

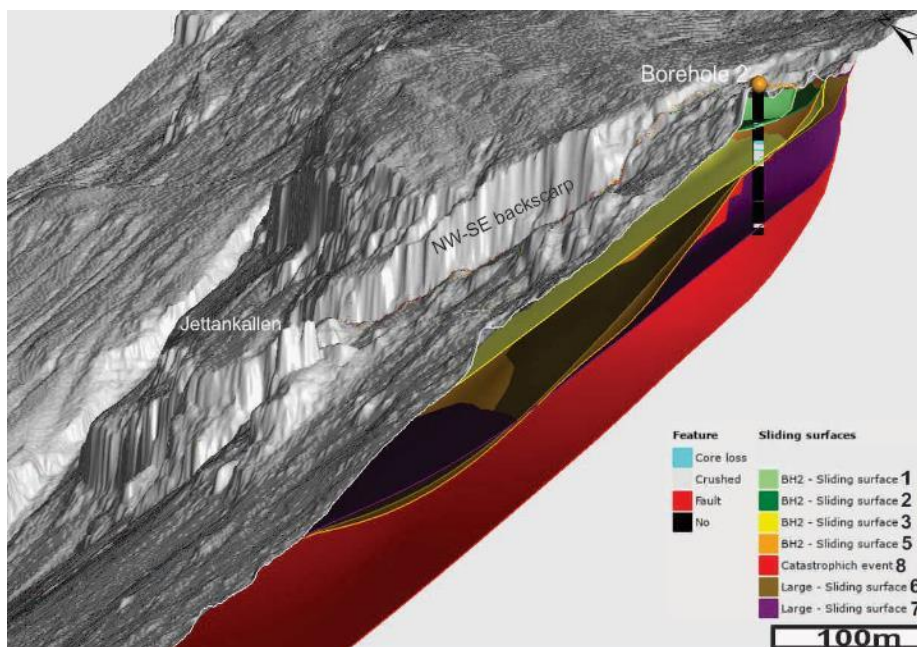In borehole 1 two main weaker zones gave the design of two predominant passages for the sliding surfaces. In borehole 3 two weaker zones gave the design of at least 2 possible sliding surfaces. Combined 4 possible sliding surfaces were made going through borehole 1 and borehole 3 in domain 3 (figure 74).
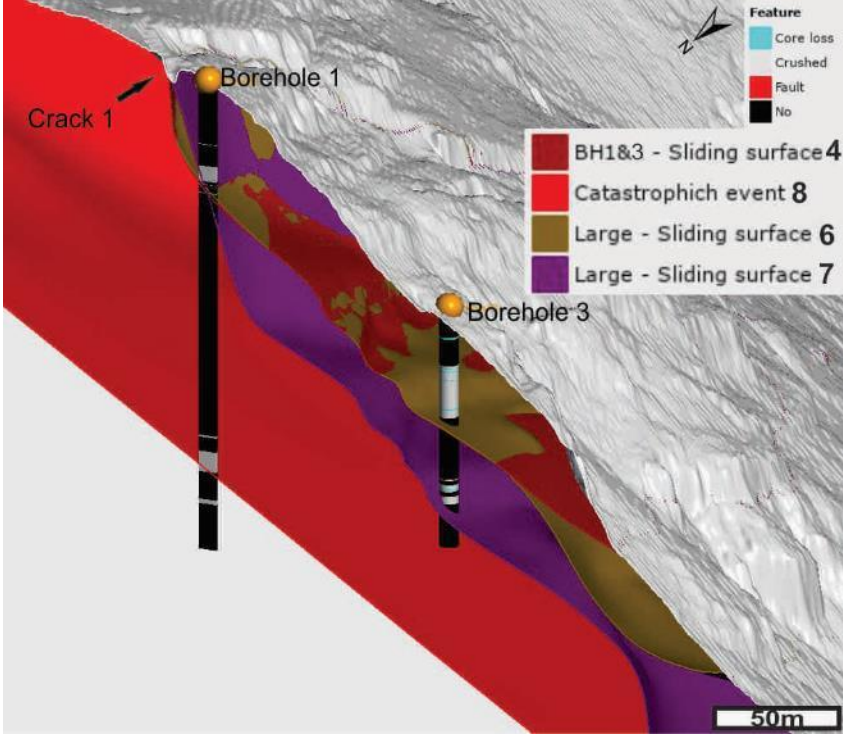


*Figure 74: Sliding surfaces in domain 3 going through borehole 1 and borehole 3.*

### 4.4.2.3 Failure scenario model

In total 9 different sliding surfaces with different dip, depth and extent were made. For the different sliding surfaces volumes for the different failure events were calculated in Leapfrog. In table 14 the different parameters for each sliding surface and possible volume are presented. The extent of the different scenarios is shown in figure 75.

| Sliding surface | Domain (Figure 49) | Borehole nr and depth | Dip | Volume [m³] |
|---|---|---|---|---|
| **1** | 1 | BH2 = 27.2 m bgl | 14° | 62 817 |
| **2** | 1 | BH2 = 27.2 m bgl | Top = 43°, bottom = 14° | 113 555 |
| **3** | 1 | BH2 = 50 m bgl | 32° | 987 385 |
| **4.1** | 3 | BH1 = 45.4 m bgl BH2 = 40 m bgl | Top = 40°, bottom = 30° | 1 644 000 |
| **4.2** | 3 | BH1 = 45.4 m bgl BH2 = 40 m bgl | Stepped sliding surface | 1 692 900 |
| **5** | 1 | BH2 = 52 m bgl | Top = 32°, bottom = 43° | 4 647 285 |
| **6** | 1, 2 and 3 | BH1 = 45.4 m bgl BH2 = 50 m bgl BH3 = 40 m bgl | Sub1: top = 31°, bottom = 43° Sub2: top = 31° Sub3: top = 40°, bottom = 30° | 7 873 585 |
| **7** | 1, 2 and 3 | BH1 = 45.4 m bgl BH2 = 91 m bgl BH3 = 81 m bgl | 34° | 10 446 185 |
| **8** | 1, 2 3, 4 and 5 | BH1 = 156 m bgl | 34° | 80 831 185 |

The volumes found are ranging from 62,817 m² to 80 Mm². Scenario 1 includes the outer displaced block in domain 1 and follows a crack between the two displaced blocks and in the upper most crushed zone in borehole 2. Scenario 2 includes the inner displaced block in domain 1, as well as scenario 1. Scenario 3 includes scenario 2, but follows a deeper sliding surface (50 m bgl) and daylights in the slope below a displaced block in the talus material where GPS 9 is located. Scenario 4.1 is a failure of domain 3, starting from crack 1 and going through the fault zone in borehole 1, the upper most crushed zone in borehole 3 and daylights in the lower parts of the domain. Scenario 4.2 is the same as scenario 4.1, but has a stepped sliding surface made from scarps. Scenario 5 includes scenario 3, but has a steeper dip in the lower parts and daylights below Jettankallen. Scenario 6 inclues domain 1, domain 3 and a large portion of domain 2. Scenario 7 includes scenario 6 but follows crushed zones that are located deeper in

the boreholes. The last scenario is a "worst case scenario" following the NE-SW striking fault, the NW-SE striking backscarp and the lower most crushed zone in borehole 1.
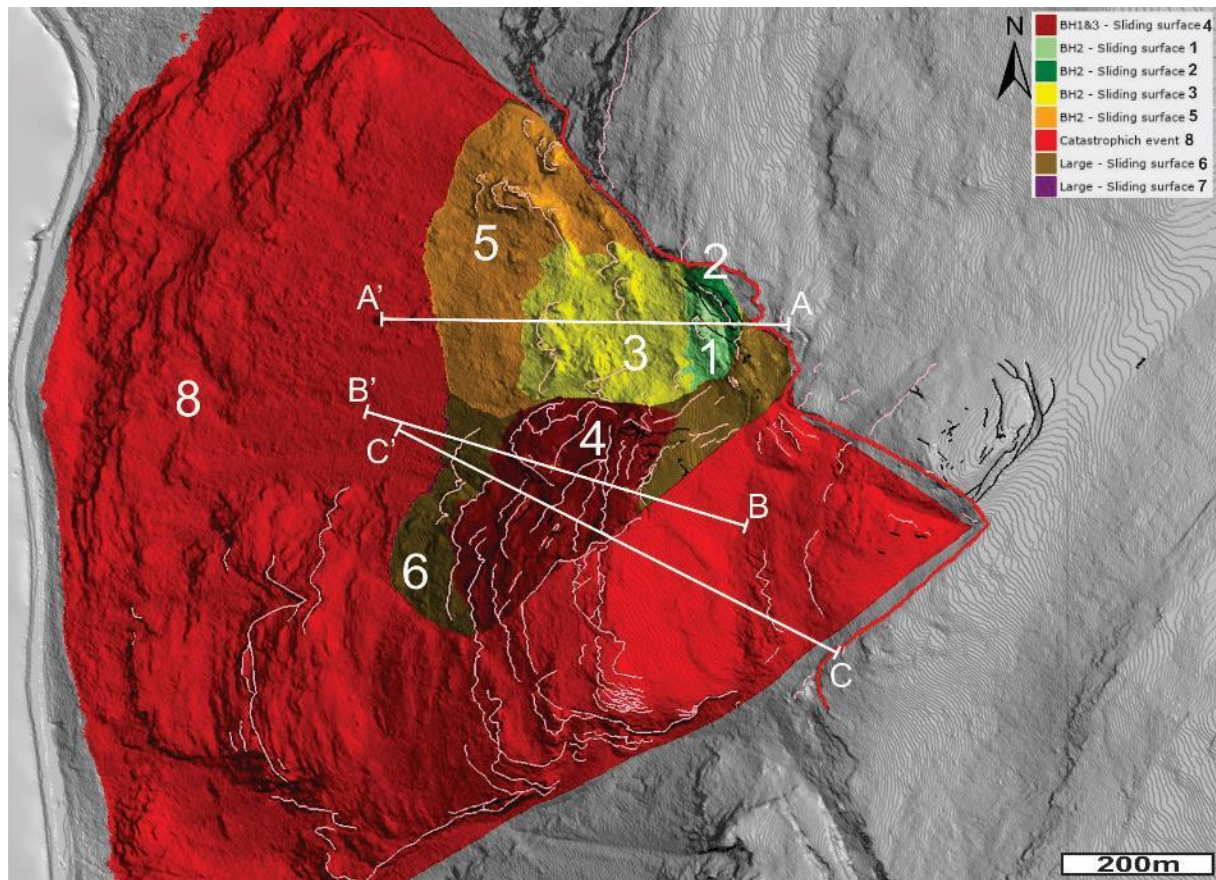


*Figure 75: Possible failure scenarios (marked with numbers) and location for the different cross-section. Failure scenario 7 is not seen at the surface as it daylight in the slope matching scenario 6. Backscarp (red line), scarps (pink lines) and tension cracks (black lines) are marked.*

Cross-sections from domain 1 and domain 2 is present in figure 76 to figure 79. The cross-sections show the different volumes for the failure scenarios, how they proceed at depth and how they interact with each other. Cross-section AA' starts at the field station, cutting borehole 2 and ends in domain 6 (figure 75 and 76). Cross-section BB' starts on the plateau in domain 2, cutting borehole 1 and borehole 3 and ends in domain 6 (figure 75, 77 and 78). Cross-section CC' streches from the fault in the south, cutting the large terrace in domain 4, slicing domain 3 and ends in domain 6 (figure 75 and 79). Scarps and fractures were added to the cross section for a better vizualization of their impact on the sliding surface (figure 78 and 79).
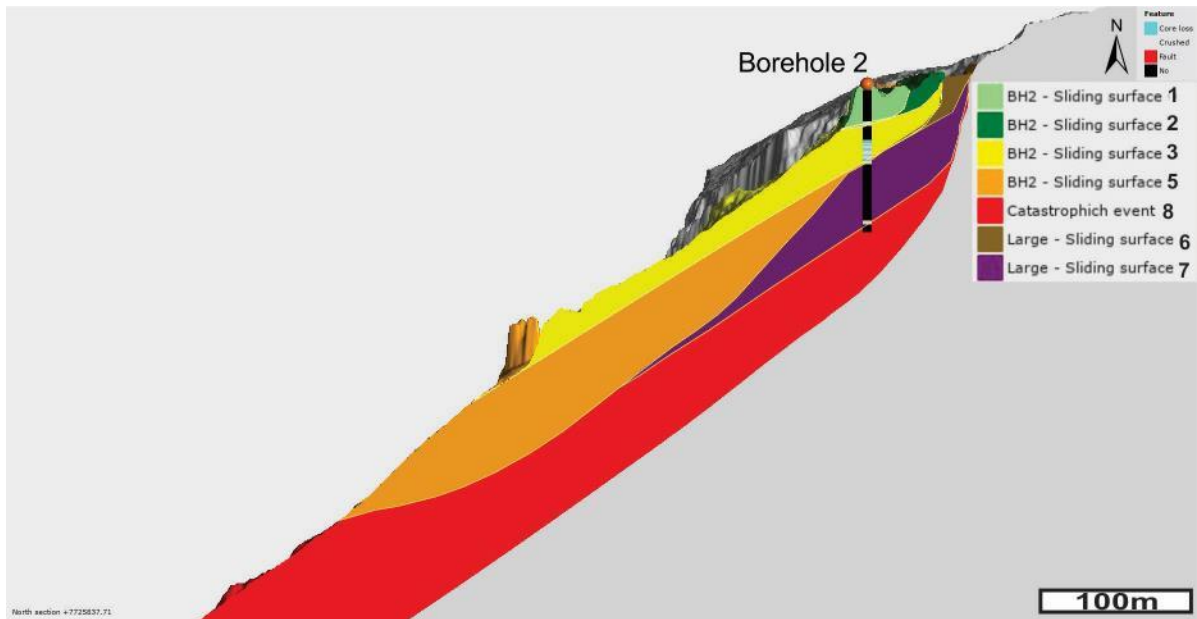
*Figure 76: Cross-section AA' showing different failure scenarios. Borehole 2 displays core loss (blue), crushed rock (grey) and fault (red). Sliding surfaces are marked with yellow lines.*
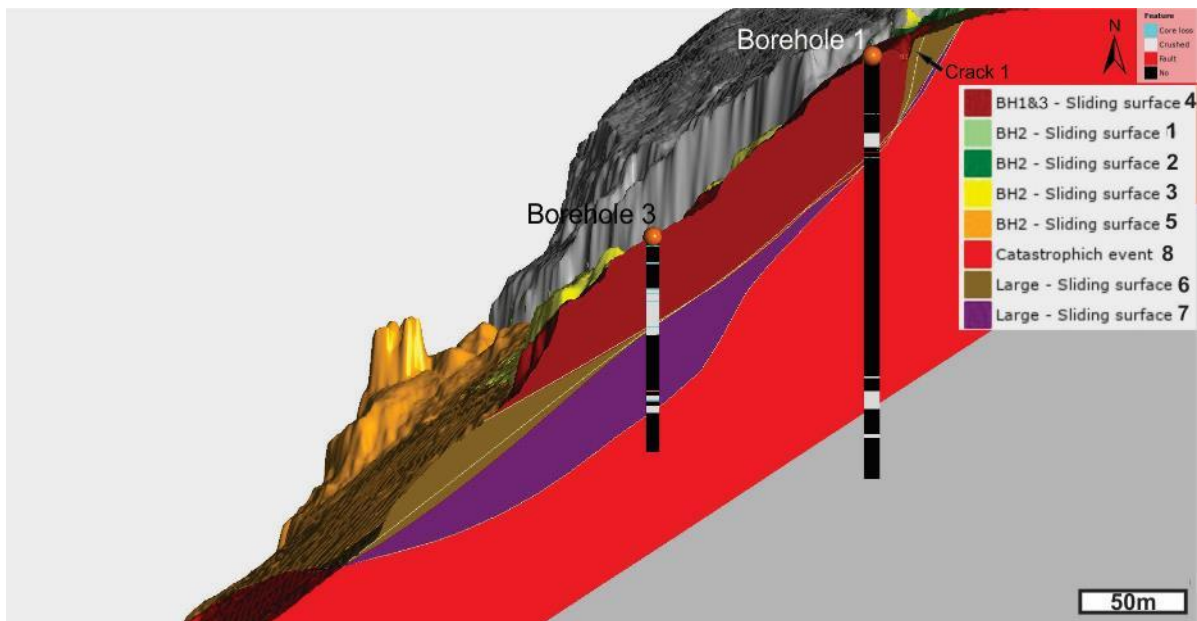


*Figure 77: Cross-section BB' showing different failure scenarios. Borehole 1 and 3 displays core loss (blue), crushed rock (grey) and fault (red). Sliding surfaces are marked with yellow lines.*
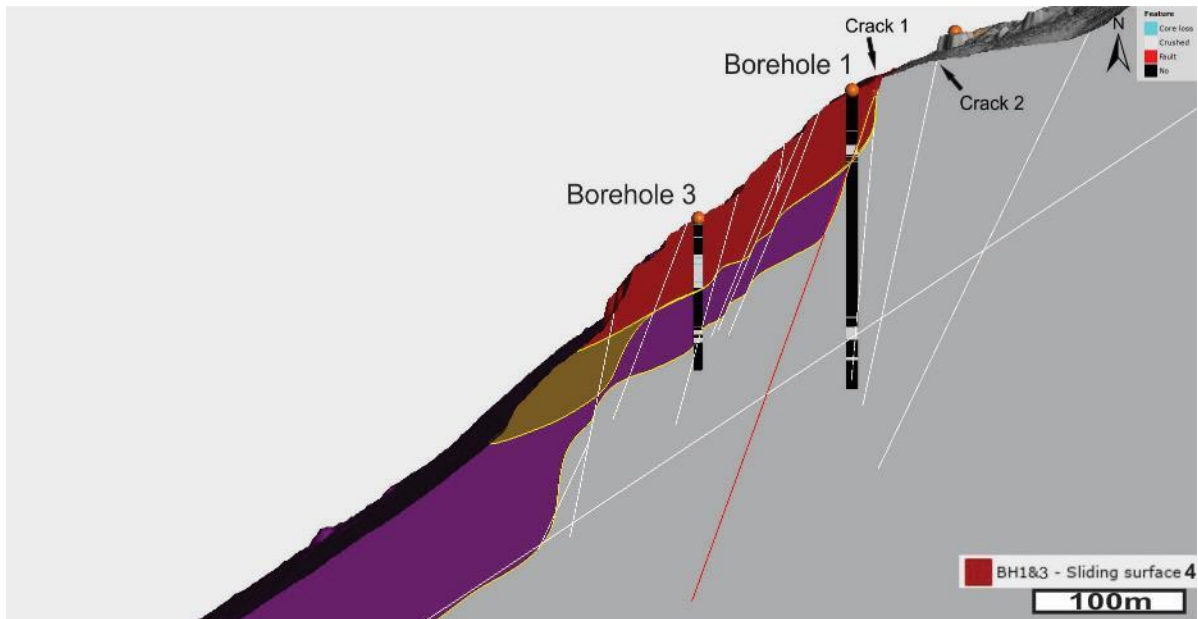
*Figure 78: Cross-section BB' showing failure scenario 4.2 including suggestions of lower sliding planes. Borehole 1 and 3 displays core loss (blue), crushed rock (grey) and fault (red). Sliding surfaces (yellow lines), scarps and fractures projected at depth (white lines) and the fault logged in borehole 1 (red line) are included.*



*Figure 79: Cross-section CC' showing failure scenario 4.2 including suggestions of lower sliding planes. Sliding surfaces (yellow lines), scarps and fractures projected at depth (white lines) and the NE-SW striking fault (red line) are included.*

## 4.5  Weather and climate

### 4.5.1  Precipitation and temperature

Precipitation at Jettan has been recorded since January 2012 and is displayed in figure 80. In the months 06/2012, 12/2012 to 06/2013, 08/2013 to 11/2013 and 03/2015 no records for precipitation was available. Average precipitatio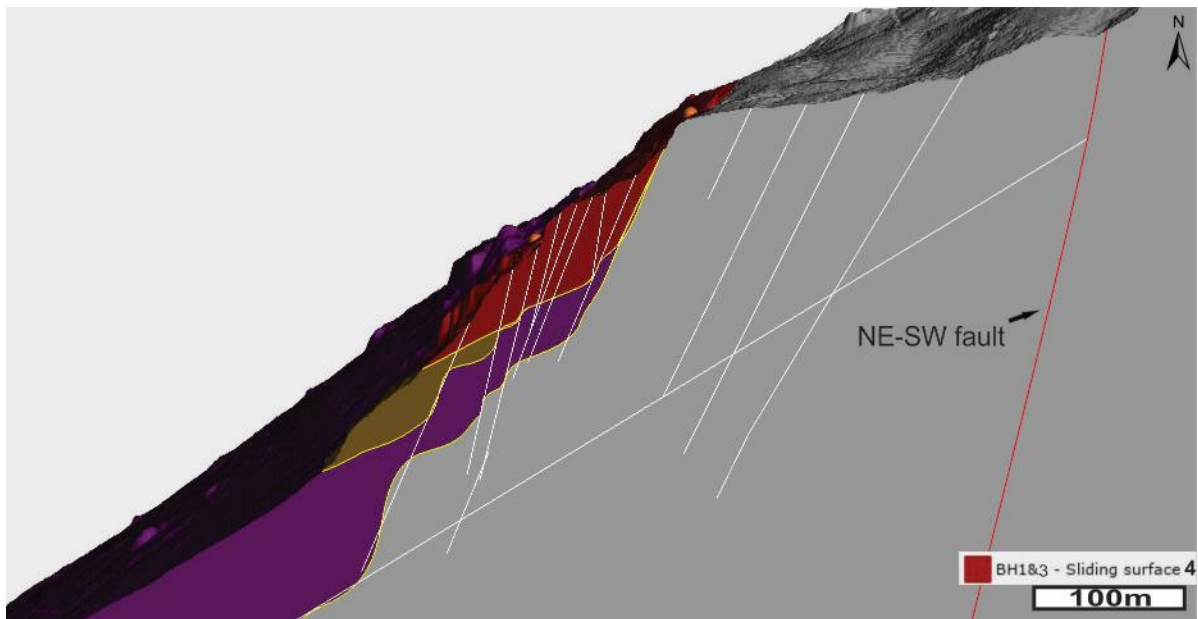n for a year at Jettan is around 350 mm (data from 2013 excluded), and around half of the precipitation occurs in the summer months June, July and August. From the records, two months with a high volume of precipitation stands out, the first event being August 2014 with 117 mm, and the second event being July 2017 with 119 mm (figure 80). Only one month in the record logged less than 5 mm precipitation, February 2018 with 0.4 mm.

The average monthly precipitation for the length of the data records (7 years) (figure 81) shows that the highest precipitation is in the summer and autumn months, while in the winter the precipitation is low (figure 81). June to September has a value above 40 mm and August has the highest average at 63 mm. January, February, March, April, November and December have precipitation just above 20 mm or lower, and is thought to come as snow since temperatures recorded in these months are around 0 °C or lower.

Temperature records also began in January 2012. The temperatures at Jettan reach a maximum around July and a minimum around January (figure 80). The highest temperatures recorded in this period was 27.6 °C in July 2018, and the lowest was -26.2 °C in February 2012. The average mean air temperature shows that positive temperatures occur from May through September (figure 81). June (4.8°C) to September has a value above 5 °C and July has the highest average at 10.1 °C. January records the lowest average air temperature at -7.35 °C.
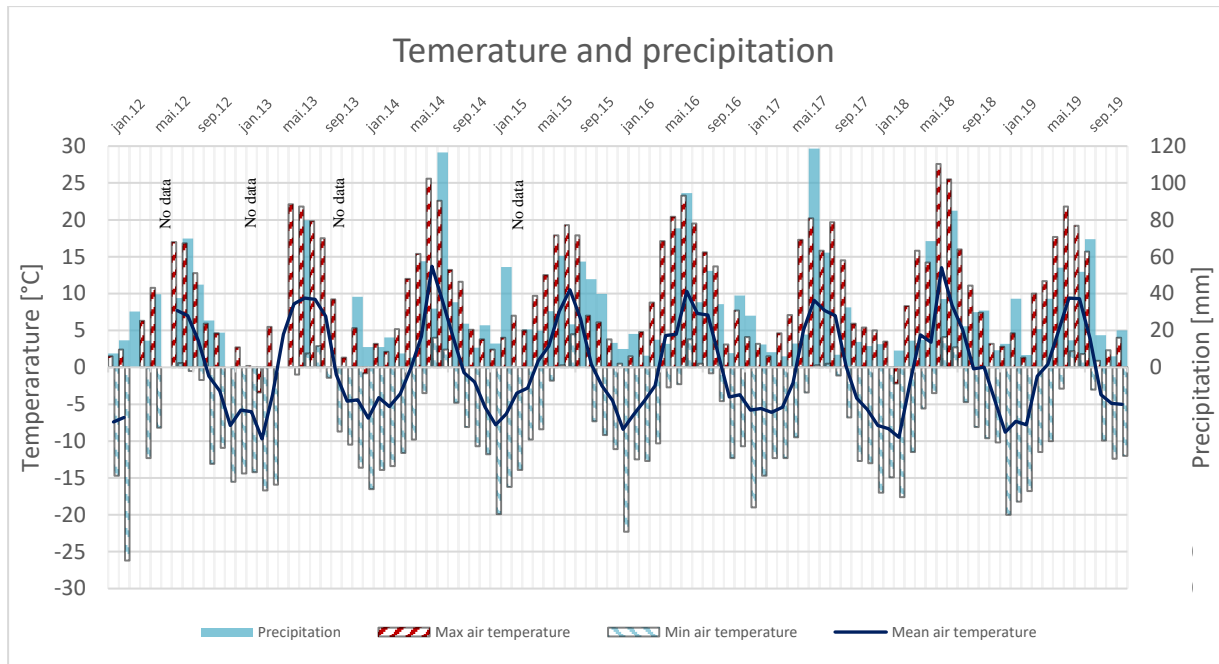
*Figure 80: Maximum, minimum and mean temperature combined with precipitation. Data is recorded from January 2012 to December 2019. "No data" marks lack of records of precipitation (Norsk_Klimaservicesenter et al., 2020; NVE, 2019).*
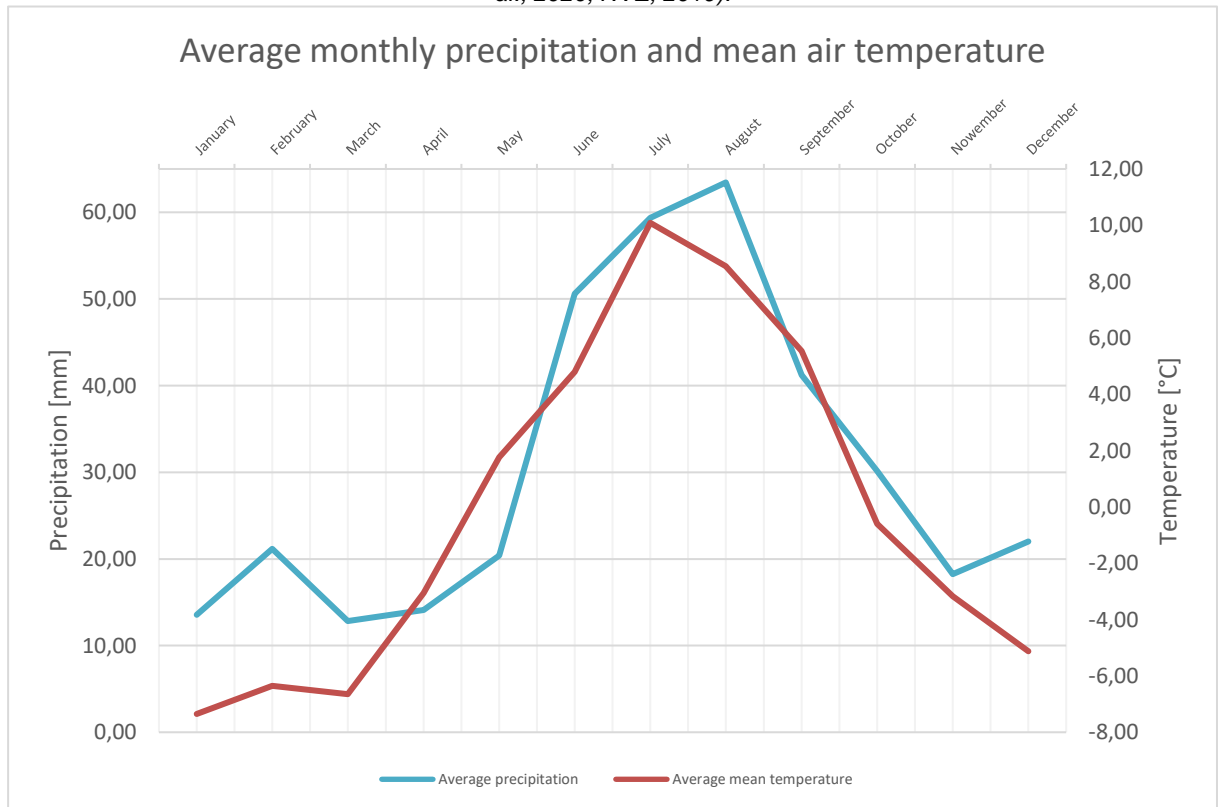


*Figure 81: Average precipitation and average mean air temperature for each month at Jettan (Norsk_Klimaservicesenter et al., 2020).*

## 4.6 Comparison between weather and climate to change in movement

In this chapter, a comparison between precipitation, temperature and movement recorded by the GPSs, extensometers and lasers will be presented. Precipitation data from January 2014 to October 2019 has been used. In 2014 the precipitation records became more detailed than the previous years. GPS total movement is used rather than movement in a specific axis, to neutralize effects such as "rock breathing". Instruments location could be found in figure 62.

### 4.6.1 GPS's vs Precipitation and temperature

The largest positive and negative changes in total surface movement is recorded during the period were the highest amount of precipitation is recorded every year (figure 82). All GPSs total movement show small changes during winter, and a summer to autumn period with larger changes. In the summer, a large negative change in movement is seen one month before a large positive change. The large positive change occurs within the same month or one month after the largest yearly precipitation, usually in July or August (figure 82). GPS 3 differs from the rest of the GPSs, by showing only positive changes in movement and no clear trend to pinpoint when the largest positive change occurs.
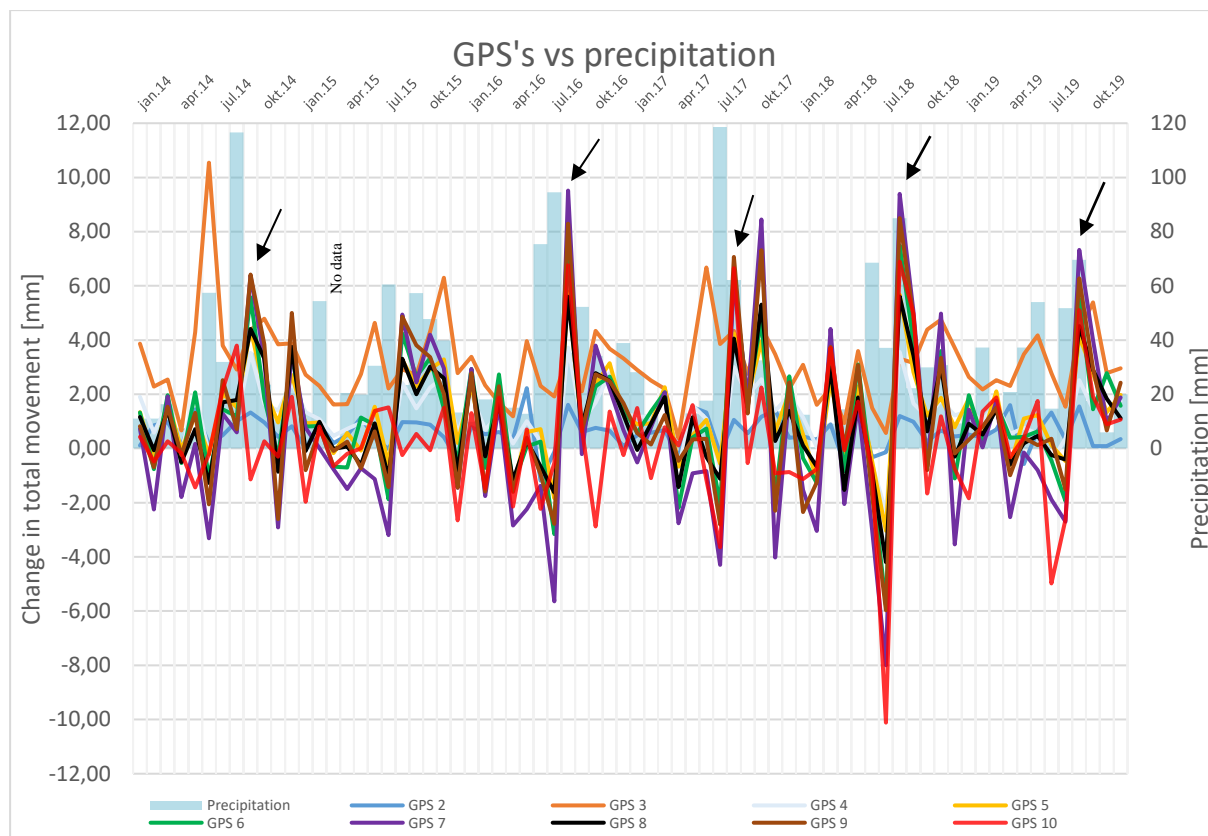
*Figure 82: Change in total movement in comparison with precipitation. "No data" marks a lack of records of precipitation. Large positive change the same month or one month after large precipitation is marked with arrows.* (Norsk_Klimaservicesenter et al., 2020; NVE, 2019)*.*

A similar trend is seen for the GPS vs temperature records. Less changes in movement are recorded in the winter period, however soon after the temperatures rises above 0 °C larger changes in movement are recorded. The largest positive change in total movement occurs one or two months after the highest maximum temperature (figure 83). 2015 recorded a low positive change in movement compared to other summers and was a summer with relatively low maximum temperature values (below 20 °C). In 2017, two months with high maximum temperatures were recorded over summer and two large positive change peaks followed. 2018 recorded the highest maximum summer temperatures, and the highest positive and negative changes in movement.
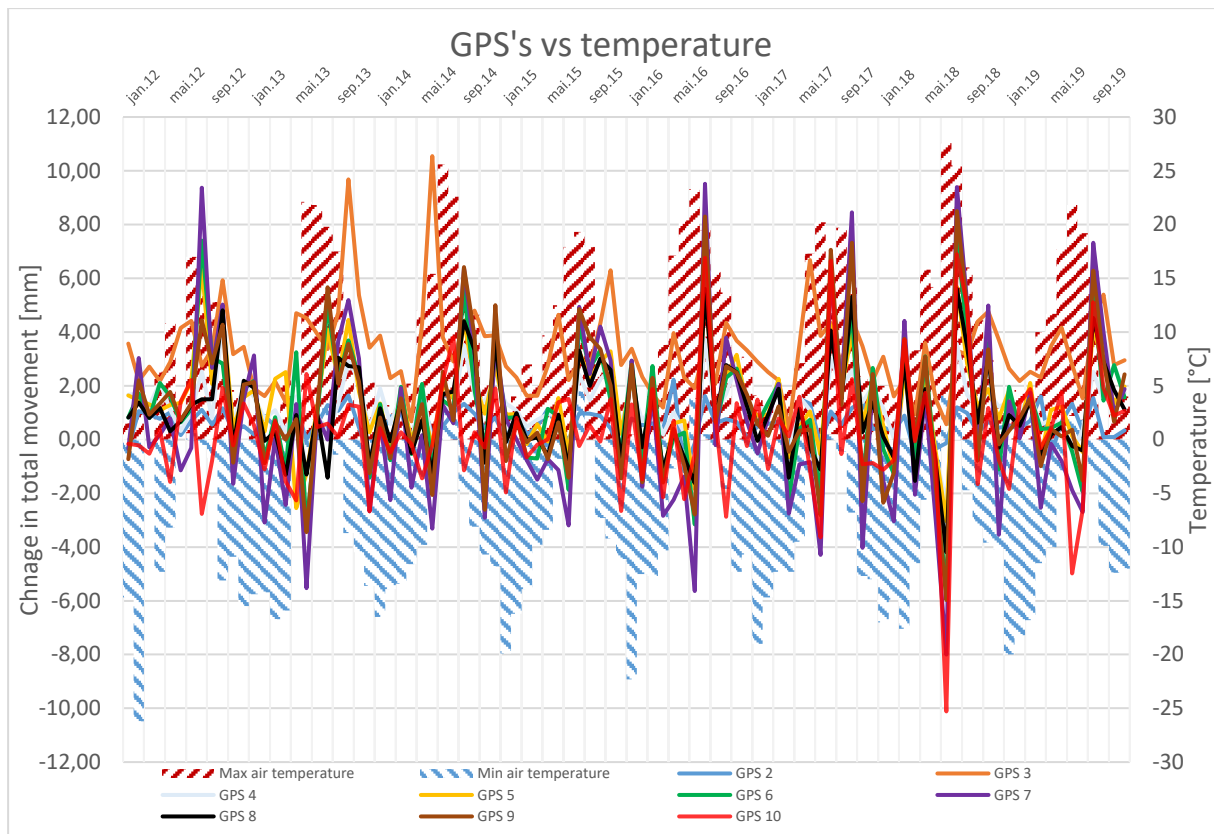
*Figure 83: Change in total movement compared to maximum and minimum temperatures.*

## 4.6.2 Extensometers vs precipitation and temperature

Positive change recorded by an extensometer represents an opening of the crack it is installed in, while negative change is a closing of the crack. Change in opening for the different extensometers show that extensometer 2 is the one with largest fluctuation from 3-6 mm (positive) and between 1-11 mm (negative) (figure 84). Negative change occurs over a two to three period, with one large negative change happening in January or February, and the large positive change occurring in the late spring/early summer. Extensometer 1 and 3 have change in opening of less than 2 mm (positive and negative). The largest negative change occurs in extensometer 1 during the early summer, around the period of heavy precipitation, and usually one month earlier than for extensometer 3. Extensometer 1 and 2 have a positive change in opening throughout the rest of the year.
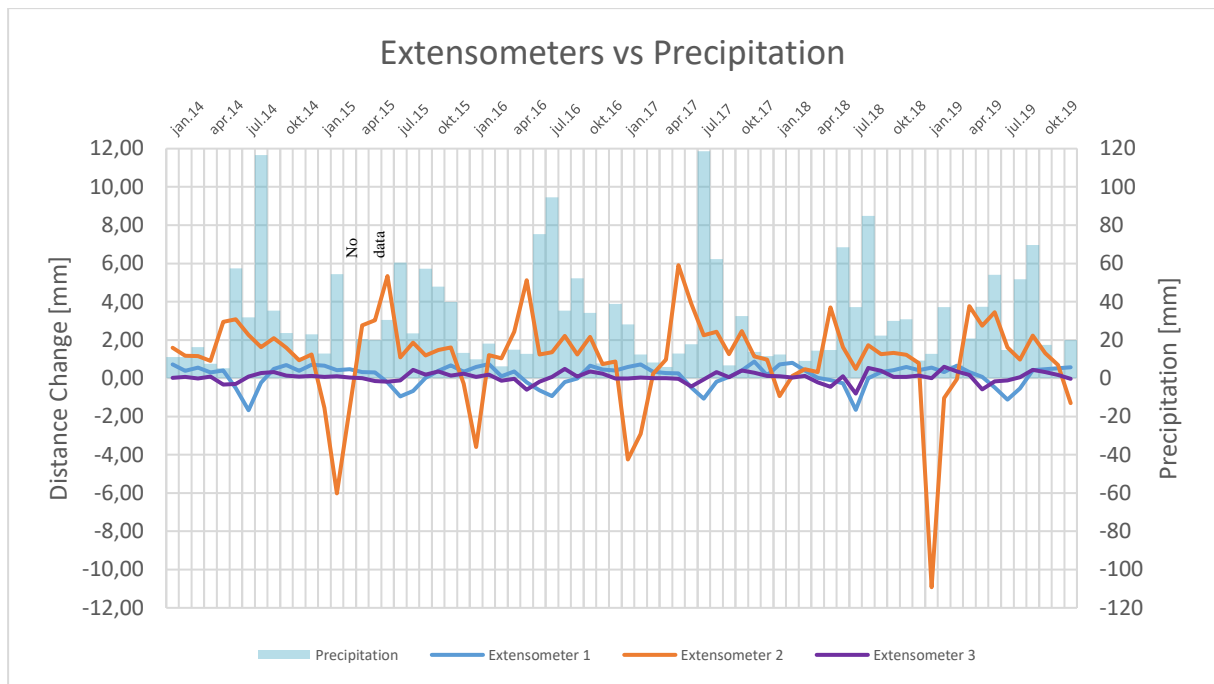
*Figure 84: Change in opening for the different extensometers in comparison to precipitation. "No data" marks lack of records from precipitation (Norsk_Klimaservicesenter et al., 2020; NVE, 2019).*

A comparison of extensometer movement to temperature shows a relatively good correlation (figure 85). Extensometer 2 has its largest negative change the same month (January) or the month after the minimum air temperature is reached. The largest positive change is seen two to three months before the highest maximum air temperature, in the period when the mean air temperature switches from negative to positive temperatures. For extensometer 1 and 2 the largest negative change in opening occurs when the maximum air temperature is at its highest or one to two months before that. In 2014 and 2018 the highest maximum air temperature was recorded at 25.6 °C and 27.6 °C and subsequently the largest negative change in opening for extensometer 1 was recorded.
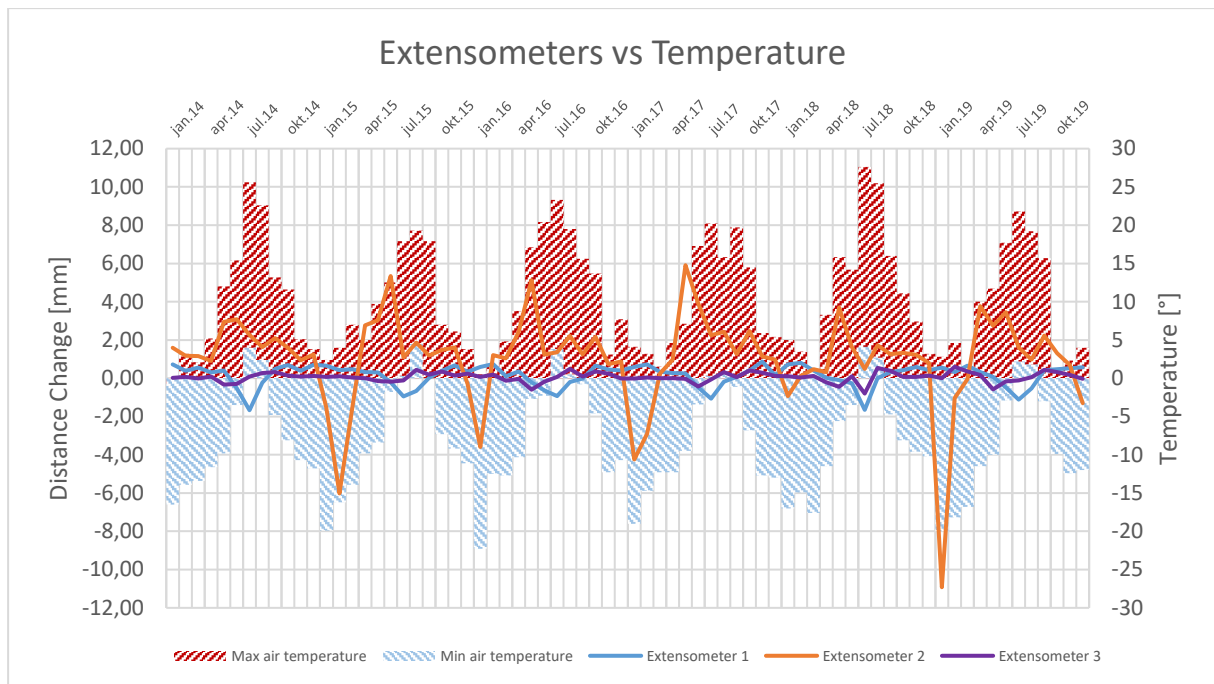
*Figure 85: Change in opening for the different extensometer in comparison with temperature (Norsk_Klimaservicesenter et al., 2020; NVE, 2019).*

### 4.6.3 Lasers vs precipitation and temperature

The lasers recorded positive values when the distance between the laser platform and receiver is increased, and negative when decreased. Laser 1 recorded mainly positive values with rare negative values, and it is recorded both large positive changes in the summer and the winter period (figure 86). Laser 2 has the largest negative change of the lasers, happening in the spring (figure 86). This is then followed by a sharp peak into positive values in the summer. Another large positive peak generally follows in the autumn. Laser 3 follows a similar pattern to laser 2, on a lower amplification.
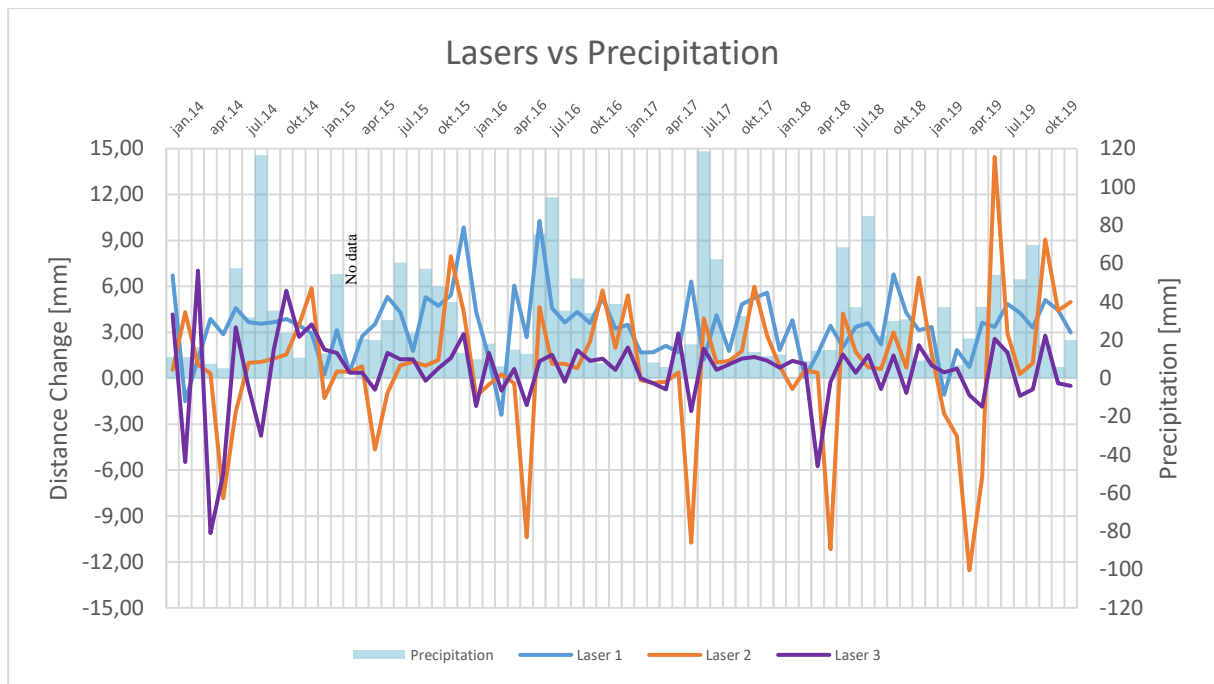
*Figure 86: Change in distance between laser and reflector for laser 1, 2 and 3 in comparison to precipitation. "No data" marks lack of records from precipitation (Norsk_Klimaservicesenter et al., 2020; NVE, 2019).*

For laser 2 and laser 3 the largest negative changes in distance was recorded around the month when the mean air temperature begun to switch between negative to positive at the end of the winter (figure 87). This negative spike follows a sharp positive spike in mean annual air temperature, with half a month delay.

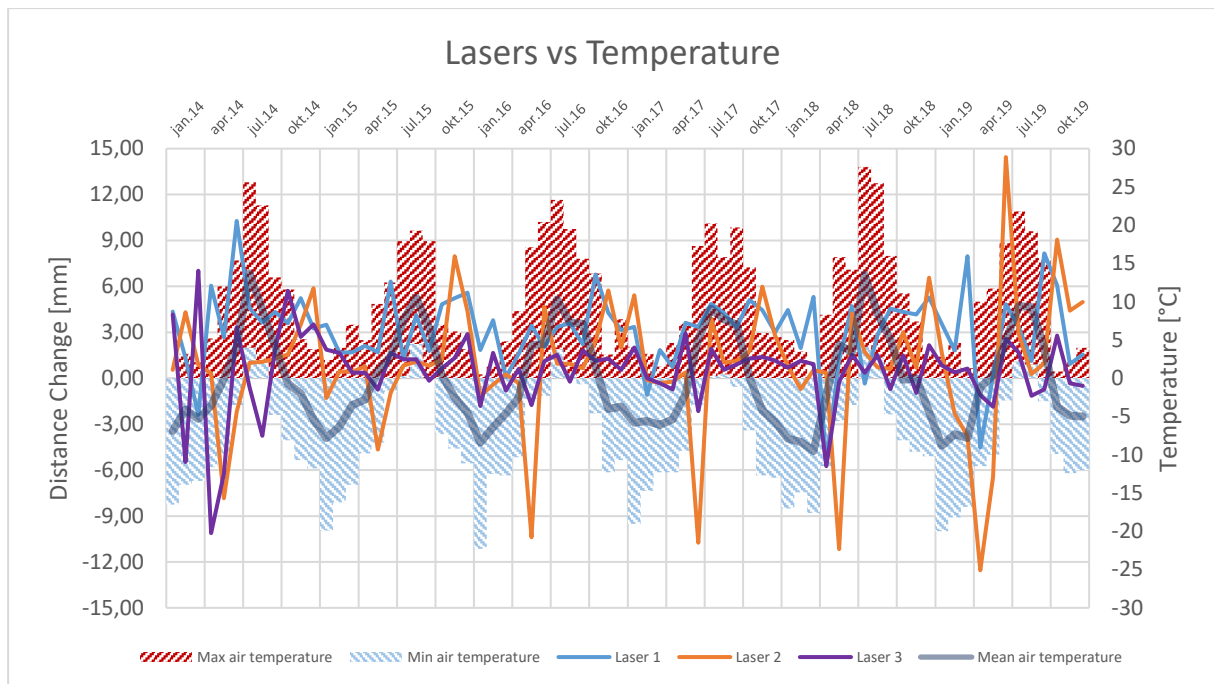*Figure 87: Change in distance between laser and reflector for laser 1, 2 and 3 in comparison to temperature (Norsk_Klimaservicesenter et al., 2020; NVE, 2019).*

# 5 Discussion

In the following, key results from this study will be discussed to gain a greater understanding of the driving mechanisms of the URS. The main goals of the study have been to fill in gaps from previous studies of the site and construct a 3D model for a better understanding of the URS.

## 5.1 Development of the rockslide

Movement at Jettan was initiated somewhere after 11-10 ka (Younger Dryas) and 9.9-9.8 ka ± 150 years (Ørnes event) as the mountain was uncapped from the glacier (Corner, 1980). The glacier acted as a buttress for the URS. When the glacier melted a removal of buttressing lead to a stress release of the slope. Deformation of the till cover within the URS supports that the movement is postglacial. Cosmogenic surface exposure dating of the fault backscarp identified that the lower part of the slope started moving before the rear (domain 5) as it gave an age of 6520 ± 335 years BP (see chapter 2.7) (Blikra & Christiansen, 2014).

At Jettan historical avalanche deposits are found in the lower part of the slope (domain 6). The deposit is vegetated and just minor rock fall material is found on top. This lead to the interpretation that the avalanche occurred short time after deglaciation. From the fact that talus material and some dislocated blocks dominated the lower part of the domain 1, the avalanche originated from here. The avalanche made a free space and removed buttressing material for subsequent areas start to move. In domain 1 this is expressed with the two displaced blocks (block 1 and block 2) and the chaotic blocky field between. The morphology in domain 3 could also be linked to the removal of buttressing material after the avalanche occurred. Along with the free space, the cracks could open up and allow movement. The scarp-terrace-scarp morphology could be seen as a consequence of this. Block 2 has a recorded movement towards WSW and domain 3 show a movement towards WNW, indicating that movement is oriented towards the free space and the assumption that the removal of buttressing material influences the deformation.

As the unstable areas continues to move material downslope, less toe support is acting on the areas behind it and a retrogressive development of the slope is forming. In subdomain 3 crack 2 supports that the slope is developing retrogressively. Crack 2 is considered a tension crack as it is mapped on a relatively flat surface absent of deformation features, parallel to crack 1 and

record slower movement rates compared to the area in front of crack 1. The areas behind crack 1 have become less constrained and the development of crack 2 could take place. Crack 1 is seen as part of the backscarp for domain 3, with further development of or a failure of domain 3, crack 2 could develop to be the new backscarp of domain 3. On the large upper terrace of domain 4 several depressions (tension cracks draped with till material) are connected to the retrogressive development. The tension cracks have the same orientation as the NE-SW boundary scarp between domain 3 and 4, and are found in a more stable area behind the scarp. A retrogressive movement towards SE is suggested by these tension cracks.

In domain 5 movement along the fault and the NW-SE backscarp started $6520 \pm 335$ years PB and has moved the area in front down 20 to 50 m towards the fjord (W/WNW). As a consequence, large fractures are found in the dolomite marble behind. InSAR data show very small movement rates and a slight increase in movement from E to W (figure 66). From the study by Eriksen et al. (2017b) a movement towards west was found for the marble dome, which contributes to the understanding of the development of the fractures. A movement towards W would lead to extension in the back and compression in the front, forming wide tension fractures at the rear, as seen on the dome. The open fractures are then recognized as tension cracks. A bending of the tension cracks towards the north could be connected to the movement towards west, but also that the dolomite marble deforms in another fashion than the surrounding garnet mica gneiss.

The landslide has disconnected from the mountain along the intersection between the fault plane and joints. The fault separates the deforming and moving area from a more stable area behind, and the NW-SE trending backscarp is controlled by the different joint sets represented in the URS. Scarps, tension cracks, morphological depressions and ridges present in the URS follows the joint sets. The scarps display a zig zagging trend constructed by the orthogonal joints and tension cracks open along joint surfaces. The smaller scarps found in domain 2, the boundary scarp between domain 3 and 4, morphological depressions found on the large terrace in domain 4 and J3 are all parallel to the fault plane implying that the fault has a large control of the slope. At Jettan, three dominating joint sets are present; J1 striking NE-SW, J2 striking ESE-WNW and J3 striking NW-SE. The orientation of the joint sets matches well with post-Caledonian faults mapped in the region by Indrevær et al. (2013) (see chapter 2.1.2). This correlation suggests that pre-existing bedrock structures influence the deformation of the slope.

## 5.2 Weakness zones

At Jettan numerous weakness zones were mapped in field. They were found in the garnet mica gneiss and are either seen as highly weathered, very weak foliated material or as a heavily deformed ductile shear zone. Additionally, the zones are foliation-parallel and include pockets of clayey silt soil. They have a gradual or distinct boundary to the host rock. Seepage was observed exiting the weakness zones, indicating that groundwater and fluid flow prefers flowing along the zone. This has contributed to an increased weathering along these weaker zones. From a historical point of view, these weaker zones at Jettan could be seen in connection with the history of the rock. Under the formation of the Caledonian orogeny thrust faults were formed between the different nappe sequence in Troms and Finnmark (Zwaan, 1988). One of these thrust faults is mapped at Nordnesfjellet between the Kåfjord nappe and Nordmannvik nappe (figure 4). The orogeny further led to the formation of foliation and ductile shear zones having a gentle dip towards W-NW (Zwaan, 1988). These shear zones are therefore thought to be equivalent to what found at Jettan, where the deformation has concentrated in these zones making a weak lithological zone.

Signs of deformation were observed in thin sections of the shear zones, as the quartz and biotite grains appear flatter and elongated, and a more distinct undulose extinction is present (indication of deformation). In addition, cracks, corroded appearance of the garnets and high amount of opaque minerals could be linked to a higher degree of weathering in the sample (figure 46). Nystad (2014) found friction angles for the different lithologies at Jettan. In the garnet mica gneiss, referred to as garnet mica schist or mica schist by Nystad (2014), a friction angle of 34.1° and 31.1° respectively were found (see chapter 2.11). In the weaker zones there was also found pockets or lenses of residual soil, which had a residual shear strength of 17-18.5°. This is a dramatic reduction of the friction angle found in the unaltered garnet mica gneiss.

Considering that the weakness zones show high degree of weathering both at the surface and in thin sections, the large reduction from a friction angle of 34.1° to a residual shear strength of ~17° and the history of the rock, it is likely that these weakness zones contribute to a significant reduction in the stability for the URS. The zones have been mapped as repeating in outcrop, so it is likely that they also repeat at depth, not only lowering the overall strength of the rock mass but providing feasible foliation-parallel sliding surfaces.

As the foliation dip of the slope is relatively low, rarely above 20°, and the joints having a dominating planar trend with a high dip (do not daylight in the slope), a stepped sliding surface between foliation and joint surfaces have been suggested by several studies (Eriksen et al., 2017a; Nordvik et al., 2010; Skrede, 2013). This stepped geometry and the possibility of the repetition of the weakness zone at depth, propose that there could be several sliding surfaces controlling the deformation.

## 5.3 Movement vs precipitation and temperature

Seasonal patterns in movement at Jettan have been discussed in several contributions (Blikra & Christiansen, 2014; Nordvik et al., 2010). In this thesis more recent movement data has been analyzed, including precipitation and temperature.

Change in total movement for GPSs showed that small changes occurred in the winter while large changes started to occur when the temperature rises above 0° in the spring (figure 83), which could be linked to the snow melt. The largest volume of precipitation occurs the summer and autumn months. The highest temperatures are recorded in July and the lowest around January. A large negative change in movement is recorded for most of the GPSs in the middle of the summer, and could be due to melting of ice in the fractures leading to compression (figure 83). Rainfall causes large positive changes up to a month after rainfall, suggesting dilation of the cracks for a time after rainfall. Two maximum temperature peaks were recorded in 2017 along with two large positive change in movement, suggesting that higher temperatures are leading to more water along the sliding plane.

GPS 3 (located on block 2) did not show a good comparison to precipitation or temperature as recorded in the other GPSs, and therefore it is thought that additional factors control the deformation of the block. The change in movement continues during the autumn and when the temperatures go below 0° for all of the GPSs, supporting the theory that an additional factor such as permafrost processes contribute to the overall deformation of the slope suggested by Blikra and Christiansen (2014).

Extensometer 2 (in crack 1; figure 62) opens during the spring in the melting season and closes in the winter. When extensometer 2 is opening, extensometer 1 (in crack 2; figure 62) records negative change in opening around a month after. This could be due to a push towards crack 2 as crack 1 opens leading to a compression in crack 2 and a negative change recorded. In 2014

and 2018 the highest maximum air temperatures were recorded and subsequently the largest negative change in opening for extensometer 1 was recorded. This is thought to be as a consequence of thermal expansion of the rock due to the high temperatures measured. The opening of extensometer 2 in the spring is seen as large movement rates in the upper part of domain 3 leading to compression in the lower part seen in records for extensometer 3 (figure 62). Extensometer 2 shows a particular good correlation to minimum air temperature as it records a large negative change in opening (e.g. 11 mm in 2019) the same month as the lowest air temperature is recorded (January; figure 85).

Laser 2 (figure 62) had a negative change in distance when the mean air temperature went from negative to positive in the spring. This is opposite as measured for extensometer 2 which measures movement of the same crack. Laser 1 (figure 62) did not show any good correlation to precipitation and temperature, like GPS 3 which measures movement of the same block (block 2). This confirms that block 2 is controlled by additional factors to precipitation and temperature.

The findings from the change in movement compared to precipitation and temperature support previous studies suggesting that movement at Jettan is influenced by seasonal variations (Blikra & Christiansen, 2014; Skrede, 2013). When the temperatures is high in the spring and summer months snow and ice melting, as well as precipitation lead to higher deformation rates. In addition, the continuing change in movement in the autumn support the suggestion of permafrost processes in the slope.

Although beyond the scope of this thesis, it is important that movement rate in response to rainfall and temperature fluctuations is quantified. For example, figure 88 below indicates styles of rock mass response to water infiltration. Direct hydromechanical relationships include changes in stress prompting changes in pore pressure (Type 1), and changes in pore pressure prompting changes in volume (Type 2). Indirect hydromechanical relationships include changes in stress prompting a change in hydraulic conductivity and storage (Type 3), or changes in pore pressure resulting in other mechanical changes (e.g. strength parameters; Type 4).

It is likely that during pore pressure changes, a change in volume occurs and a dilation of the rock mass is recorded by GPS and other instruments during and for a while after rainfall and snowmelt periods. This would indicate that Jettan displays a Type 2 hydromechanical

relationship, although it is likely that strength properties deteriorate overtime with pore pressure events (Type 4). For example, weathering/fluid flow along 'weakness zones' has contributed to a lower shear strength of the material.
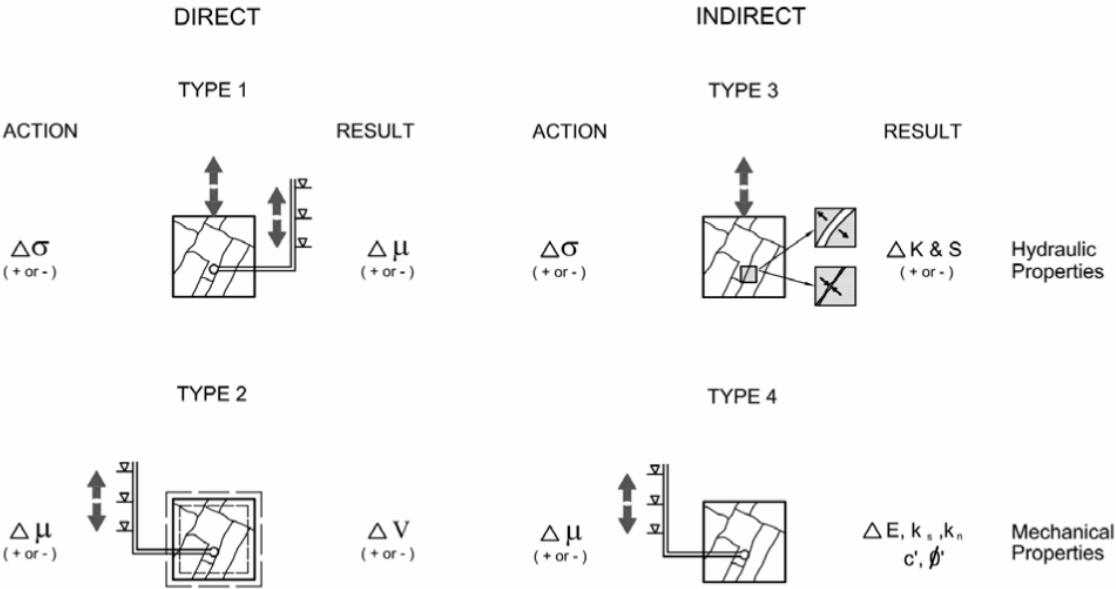


*Figure 88: Forms of hydromechanical coupling (Sullivan, 2007). Δσ is a change in stress, Δμ is a change in pore pressure, ΔV is a change in volume, K is hydraulic conductivity, S is storage, E is modulus of elasticity, ks is shear stiffness, kn is normal stiffness, c is cohesion and Φ is angle of friction.*

## 5.4 Groundwater

Groundwater flow is an important aspect when it comes to the stability of a slope as it diminishes the shear strength of potential failure surfaces (Wyllie et al., 2004).

At Jettan no groundwater was registered for borehole 1, in borehole 2 water was found around 90 m bgl, and in borehole 3 water was found around 90 m bgl and were interpreted to be a hanging water table as no water was found in borehole 1 (Nystad, 2014). This could indicate that the high amount of fractured rock together with limited water flowing into the URS has lowered the groundwater table in certain areas of the slope. No streams were observed flowing directly into the URS, only evidence of seasonal drainage north of the field station and below the large wall in domain 3 was found. Some seepage was seen entering the URS north of the field station (figure 52), in connection to the dried stream. Melting of snow in the spring and precipitation in the catchment area is therefore viewed as the main contributor to the

groundwater. Observations of seepage in field revealed that it followed joint surfaces and foliation and exited through the foliation or weakness zones (e.g. beneath filed station; figure 45CB). Due to the fractured character of the rock mass and little water observed at the surface, the water is thought to follow fractured rock and discontinuities through the unstable area. In the lower scarps in domain 7 calcite coating were present on joint surfaces. As calcite marble is only observed at higher elevations in the slope some groundwater flow is exiting in the lower parts of the URS, supporting the proposal of water following fractured rock and discontinuities through the slope.

The continuing deformation of the slope through the autumn is believed to be connected to permafrost processes (see chapter 2.5) (Blikra & Christiansen, 2014). When water freezes in fractures it could lead to a block for the ground water drainage and further lower the stability by increasing the pore pressure (Wyllie & Mah, 2004). Another process leading to a reduction in stability and movement is the formation of ice wedges. The increase in volume of the ice in the fractures when groundwater freezes, will enlarge the fracture and break rock bridges.

As water is present in the slope and found following discontinuities it will affect the stability of the slope by lowering the effective stress and increase the pore pressure (Wyllie & Mah, 2004). Together with freezing and thawing processes the groundwater contributes to a lowering of the stability of the slope. Water is therefore seen as one of the controlling factors for the deformation at Jettan.

The continuing deformation of the slope through the autumn is believed to be connected to permafrost processes (see chapter 2.5) (Blikra & Christiansen, 2014). When water freezes in fractures it could lead to a block for the ground water drainage and further lower the stability by increasing the pore pressure (Wyllie & Mah, 2004). Another process leading to a reduction in stability and movement is the formation of ice wedges. The increase in volume of the ice in the fractures when groundwater freezes, will enlarge the fracture and break rock bridges.

As water is present in the slope and found following discontinuities it will affect the stability of the slope by lowering the effective stress and increase the pore pressure (Wyllie & Mah, 2004). Together with freezing and thawing processes the groundwater contributes to a lowering of the stability of the slope.

## 5.5 3D model

### 5.5.1 Validation of the 3D model

#### 5.5.1.1 Lithological model

The intention of the bedrock model was to gain a greater understanding of how the lithological units develop in the interior of the slide and for visualization purposes.

The lithological model was not considered valid to express the different lithologies prevalence. Considering that the area has been subject to movement at different magnitudes for different areas it was challenging to create a realistic model. Nevertheless, in domain 3 the logged borehole lithologies matched well with mapped outcrops and the correlation is good in this area. Additionally, the dolomite lenses in the lower part of domain 1 corresponds well with fieldwork. Another aspect influencing the validation of the model is the persistence of the different lithological units. The calcite marble expressed change in greatness across the slope and were affected by lenses making various dip. In the model the different surfaces separating the lithological unites were planar and based on the foliation measured in the boreholes, suggesting that the persistence of the different lithological units could differ substantially from the actual slope.

In the building of the bedrock model in Leapfrog it was not taken into account that this area has been subject to movement. This is the main reason to deviation between the model and fieldwork. More time could have been dedicated to the lithological model, but as the failure scenario model was considered more relevant to gain a better understanding of the deformation in the URS, more work was put into this.

#### 5.5.1.2 Failure scenario model

The intention of the failure scenario model was to get a greater understanding of the controlling structures at Jettan in depth by interpolating surface and borehole data.

Bounding features like scarps and depressions in the model were made based on an average of field measurements and adjustments to the DEM for a better match. The bounding features were not including the zig zagging pattern found in the scarps and were representing a general trend in the model. This could produce deviations in the model from what is actually happening. But

as features are represented by the overall orientation, the bounding features was considered reasonable.

In addition, the joints at Jettan show both planar and listric persistence at depth, with the planar joints as most dominating. In the model the scarps were put as listric and the sliding surfaces as planar for most of the scenarios. For subdomain 3 an additional model was made with persistent scarps offsetting the sliding plane in a stepped matter downslope (based on the morphology; figure 78 and 79). Based on the joints' persistence and the morphology both listric and persistent scarps are possible, suggesting that the sliding surfaces in the model could deviate from the authentic sliding surfaces. The sliding planes are based on the borehole data and where it is most likely to daylight the slope. One or two planes combine with constant dip and dip direction to create a planar sliding surface (except for 4.2). The borehole gives insight of the rock mass at a specific column in the slope, how the possible sliding planes are externally evolving is needed to be interpreted based on the morphology. A planar or stepped sliding surface could both be possible, but large deviation of the sliding planes could occur.

Comparing the 3D model to others interpretations of the sliding surfaces shows a good correlation between most of the models for domain 3. Eriksen et al. (2017a) suggested several stepped sliding surfaces and Nystad (2014) concluded that the sliding surfaces at Jettan included several surfaces (see chapter 2.9). While in domain 1 Eriksen et al. (2017a) has suggested a stepped sliding surface, in the 3D model a planar and listric surface was made.

Scenario 1, 4.2, 5 and 6 are viewed as the most realistic failure scenarios. Scenario 1 is a failure of block 2 and some of the disintegrated rock mass behind. This is seen as a possible scenario, because the block records the largest movement rates at Jettan and it lies on a break of the terrain. As it lies on a break of the terrain, express a love movement dip (table 10) and the present of J1, a toppling failure is regarded as more realistic compared to a planar sliding suggested in the model. Scenario 2 is regarded less possible as the sliding plane record 14°, and therefore a deeper going structure including a larger area is thought to contain this portion of the slope. Scenario 3 cuts displaced blocks in domain 1 and do not include Jettankallen. It is therefore not considered as less feasible. Scenario 4.2 is seen as a realistic scenario as domain 3 show the second highest movement rates, the subsequent areas record less movement, the sliding surface cut the boreholes in the most deforming zones and the area is dominated by

morphological deforming features. As the slope show a scarp-terrace-scarp morphology a stepped sliding surface is most likely for the failure scenario. This suggests that scenario 4.2 is more realistic than scenario 4.1. Scenario 5 is seen as realistic as it includes domain 1 with high movement rates, the sliding surface goes through borehole 2 in a highly crushed zone and exits beneath the lower displaced blocks of domain 1 showing less movement. Scenario 6 is seen as realistic as it includes the high deforming areas domain 1 and domain 3, the sliding surface goes through the main weakness zones in the boreholes and earlier studies has suggested this as a possible scenario (see chapter 5.5.2). Scenario 7 has the same surface extent as scenario 6 but cuts borehole 2 and 3 at a greater depth in considerably less fractures zones including a large volume, and is therefore considered as less possible. Scenario 8 is a worst-case scenario including the entire unstable rock slope. The sliding surface cuts in the lower most fractured zone in borehole 1, including a large volume. As the slope is considered to be retrogressive and only smaller movement velocities are recorded in the upper part, the scenario is therefore thought to be very unlikely.

## 5.5.2 Volumes

The most realistic scenarios which were discussed in chapter 5.5.1.2, are scenario 1, 4.2, 5 and 6 which had the volumes of 62,817 $m^3$, 1.69 $Mm^3$, 4.67 $Mm^3$ and 7.87 $Mm^3$ (table 14) respectively. In previous studies the volume estimates has ranged from 22 $Mm^3$ (Blikra et al., 2009) to the newest study estimating the volume to be 6 $Mm^3$ (NVE, 2016) (see chapter 2.10). It was estimated a similar scenario from the failure of scenarios 6 and 7 (figure 36). In the 3D model scenario 6 gave almost a volume of 2 $Mm^3$ more than the estimated volume by NVE, while scenario 7 gave a volume of 4 $Mm^3$ more. This difference could be due to different depths of the sliding surface or that in the 3D model the failure scenario includes a larger surface area. While NVE placed the sliding surface at approximately 35 m bgl, the 3D model utilizes a sliding surface encountered at 45 m in borehole 1, borehole 2 at 50 m and borehole 3 at 40 m, which will give larger volumes for the 3D model. As the thickness of the sliding area deviates by as much as 15 m at the most, the depth to the sliding surface is assumed to be the main reason for a larger volume in the 3D model.

# 6 Conclusion

The main findings of this work are:

- The different joint sets at Jettan had similar strike as mapped regional faults in Troms and Finnmark, supporting the suggestion that the URS is deforming along inherited structures in the bedrock.

- The slope shows a retrogressive movement with tension cracks at the rear of high deforming areas.

- Three areas show particularly large movement rates. Deformation in domain 1 and 3 was initiated when removal of buttressing material in front occurred after an avalanche event.

- Change in movement compared to precipitation revealed that both temperature and precipitation influence movement at Jettan, but it also supported the suggestions of permafrost processes in the autumn.

- A weaker zone was found in the slope and interpreted to reduce the stability of the slope as it is preferentially weathered, deformation and weathering was found in thin sections, it contributes to the fluid flow of the URS and the fact that the soil had a residual shear strength of $17°$. The weak zones were interpreted to be present at depth and therefore thought to be potential sliding surfaces.

- Groundwater and groundwater flow contributes to the reduction of stability to the slope. It was found calcite coating in the lower parts of the slope, indicating that ground water flow follows joints and foliation in the interior of the slope.

- Permafrost processes as freezing and thawing may be a controlling factor as there is observed ice in the fractures of the URS and continuous deformation throughout the autumn.

- The 3D model supported a stepped sliding surface for domain 3 and suggested several possible failure scenarios.

- Volume estimates from the 3D model gave a volume of 7.87 $\text{Mm}^3$ for the largest most reasonable failure scenario. A deviation from previous findings of 2 $\text{Mm}^3$ was considered to be caused by a deeper sliding plane used for the 3D modeling.

- 3D modeling is time consuming and a more realistic model could have been made if more time was addressed to it and the work with Leapfrog had begun at an earlier stage.

# Work sited

Berger, A. (1988). Milankovitch theory and climate. *Reviews of geophysics, 26*(4), 624-657.

Bergh, S. G., Eig, K., Kløvjan, O. S., Henningsen, T., Olesen, O., & Hansen, J.-A. (2007). The Lofoten-Vesterålen continental margin: a multiphase Mesozoic-Palaeogene rifted shelf as shown by offshore-onshore brittle fault-fracture analysis. *Norwegian Journal of Geology/Norsk Geologisk Forening, 87*.

Blikra, L., Henderson, I., & Nordvik, T. (2009). Faren for fjellskred fra Nordnesfjellet i Lyngenfjorden, Troms. *Geological Survey of Norway Report, 2009*, 29.

Blikra, L. H., Eiken, T., Henderson, I., & Venvik-Ganerød, G. (2006). Forprosjekt fjellskred i Troms–Status 2005. *NGU Rapport*.

Blikra, L. H., & Bunkholt, H. (2012). Tunnel gjennom Nordnesfjellet i Kåfjord, Troms: Oversikt over nærliggende ustabile fjellparti og påvirkning på stabilitet. *NGU Rapport 2012.02*, 30.

Blikra, L. H., & Christiansen, H. H. (2014). A field-based model of permafrost-controlled rockslide deformation in northern Norway. *Geomorphology, 208*, 34-49.

Braathen, A., Blikra, L. H., Berg, S. S., & Karlsen, F. (2004). Rock-slope failures in Norway; type, geometry, deformation mechanisms and stability. *Norwegian Journal of Geology/Norsk Geologisk Forening, 84*(1).

Christiansen, H. H., Etzelmüller, B., Isaksen, K., Juliussen, H., Farbrot, H., Humlum, O., . . . Hjort, J. (2010). The thermal state of permafrost in the Nordic area during the International Polar Year 2007–2009. *Permafrost and Periglacial Processes, 21*(2), 156-181.

Corner, G. D. (1980). Preboreal deglaciation chronology and marine limits of the Lyngen - Storfjord area, Troms, North Norway. *Boreas, 9*(4), 239-249.

Dannevig, P. (2019, 28.01.2019). Troms - klima. Retrieved from https://snl.no/Troms_-_klima

Dehls, J. F., Olesen, O., Olsen, L., & Blikra, L. H. (2000). Neotectonic faulting in northern Norway; the Stuoragurra and Nordmannvikdalen postglacial faults. *Quaternary science reviews, 19*(14-15), 1447-1460.

Dimetix. (2016a). Distance Laser Sensor. Retrieved from https://dimetix.com/wp-content/uploads/2016/07/ManualDLSB.pdf

Dimetix. (2016b). DLS-C - for millimeter precise measuring in extreme situations.

Dimetix. (2016c). FLS-C - for fast measurements and unique accuracy.

Durham_Geo_Slope_Indicator. (2019). VW Crackmeter. Retrieved from https://durhamgeo.com/product/vw-crackmeter/

Elvebakk, H. (2013). Borehullslogging med optisk televiewer, Jettan 1, Nordnesfjellet, Kåfjord kommune, Troms. *Norges geologiske undersøkelse Report 2013.020*.

Elvebakk, H. (2014). Borehullslogging med optisk televiewer, Bh 2 og Bh 3, Jettan, Nordnesfjellet, Kåfjord kommune, Troms. *Norges geologiske undersøkelse Report 2014.016*.

Eriksen, H. Ø. (2013). *Slope displacement patterns observed using satellite InSAR data in the Storfjord-Kåfjord-Lyngen region, Troms.* Universitetet i Tromsø,

Eriksen, H. Ø., Bergh, S. G., Larsen, Y., Skrede, I., Kristensen, L., Lauknes, T. R., . . . Kierulf, H. P. (2017a). Relating 3D surface displacement from satellite-and ground-

based InSAR to structures and geomorphology of the Jettan rockslide, northern Norway.

Eriksen, H. Ø., Lauknes, T. R., Larsen, Y., Corner, G. D., Bergh, S. G., Dehls, J., & Kierulf, H. P. (2017b). Visualizing and interpreting surface displacement patterns on unstable slopes using multi-geometry satellite SAR interferometry (2D InSAR). *Remote Sensing of Environment, 191*, 297-312.

Ganerød, G. (2013). Geological logging of drill core from borehole NN-01-12 at Jettan, Nordnes mountain in Troms county, Northern Norway. *Norges geologiske undersøkelse Report 2013.042*.

Ganerød, G. (2014). *Geological logging of drill cores from borejole BH 02-13 and BH 03-13 at Jettan, Nordnes mountain in Troms county, Northern Norway* (2014.005). Retrieved from

Google. (2019). Google maps. Retrieved from https://www.google.no/maps/@65.5646791,26.2970033,5.5z/data=!5m1!1e4?hl=no

Hegstad, S. M. K. (2014). *Post-glacial sedimentary processes and slope instabilities off Nordnesfjellet, Lyngenfjorden, northern Norway.* UiT Norges arktiske universitet,

Henderson, I., & Blikra, L. (2007). Bakgrunnsinformasjon for oppbygging av flodbølgeanalyse ved Nordnesfjellet, Troms. *NGU Rapport*.

Henderson, I., Osmundsen, P., & Redfield, T. (2010). ROS Fjellskred i Troms: Status og planer, 2009. *Norges geologiske undersøkelse, Rapport*.

Hermanns, R., Hansen, L., Sletten, K., Böhme, M., Bunkholt, H., Dehls, J., . . . Høgaas, F. (2012a). Systematic geological mapping for landslide understanding in the Norwegian context. *Landslide and engineered slopes: protecting society through improved understanding. Taylor & Francis Group, London*, 265-271.

Hermanns, R., Oppikofer, T., Anda, E., Blikra, L., Böhme, M., Bunkholt, H., . . . Fischer, L. (2012b). Recommended hazard and risk classification system for large unstable rock slopes in Norway. *NGU Rapport*.

Hermanns, R. L., & Longva, O. (2012c). Rapid rock-slope failures. *Landslides: types, mechanisms and modeling*, 59-70.

Hermanns, R. L., Oppikofer, T., Molina, F. X. Y., Dehls, J. F., & Böhme, M. (2014). Approach for systematic rockslide mapping of unstable rock slopes in Norway. In *Landslide science for a safer geoenvironment* (pp. 129-134): Springer.

Høst, J., NGU, Protection, T. N. D. f. C., Agency, T. N. A., Administration, T. N. P. R., Authority, T. N. R., & Authority, T. N. M. (2006). *Store fjelskred i Norge*. Retrieved from

INC, N. G. S. (2005). Rock > field guide sheet. Retrieved from https://fl-nzgs-media.s3.amazonaws.com/uploads/2016/06/Field-guide-sheet-description-of-soil-and-rock-2005.pdf

Indrevær, K., Bergh, S. G., Koehl, J.-B., Hansen, J.-A., Schermer, E. R., & Ingebrigtsen, A. (2013). Post-Caledonian brittle fault zones on the hyperextended SW Barents Sea margin: New insights into onshore and offshore margin architecture. *Norwegian Journal of Geology, 93*(3-4).

Kartverket. (2016). Norge i bilder. Retrieved from https://norgeibilder.no/

Kartverket. (2019). Norgeskart. Retrieved from norgeskart.no

Lambrecht. (2017). Product Catalogue.

Lauknes, T., Shanker, A. P., Dehls, J., Zebker, H., Henderson, I., & Larsen, Y. (2010). Detailed rockslide mapping in northern Norway with small baseline and persistent

scatterer interferometric SAR time series methods. *Remote Sensing of Environment, 114*(9), 2097-2109.

Lauknes, T. R. (2011). Rockslide mapping in Norway by means of interferometric SAR time series analysis.

Marinos, P., & Hoek, E. (2000). *GSI: a geologically friendly tool for rock mass strength estimation.* Paper presented at the ISRM international symposium.

Nesje, A. (2012). *Brelære*. Kristiansand: Høyskoleforlaget AS-Norwegain Academic Press.

NGI. (2007). *Flodbølger etter mulig fjellskred, Nordnes, Lyngen kommune. Beregning av mulige fjellskred og flodbølger*. Retrieved from

NGI. (2013). *Flodbølger i Lyngen etter mulig skred, Nordnes, Lyngen kommune III. Detaljberegning av oppskylling for skred på 11 millioner kubikkmeter*. Retrieved from

NGI. (2015). Bruk av Q-systemet - Bergmasseklassifisering og bergforsterkning.

NGI. (2018). *Flodbølger etter fjellskred i Lyngen. Oppskyllingsberegninger ved hjelp av probalistiske metoder*. Retrieved from

NGI. (2019). Steinskred og fjellskred. Retrieved from https://www.ngi.no/Tjenester/Fagekspertise/Steinskred-og-fjellskred

NGU. (2016). *Rapport om fare - og risikoklassifisering av ustabile fjellparti - Jettan*. Retrieved from http://geo.ngu.no/api/faktaark/ustabilefjell2/visRapport.php?globalid=%7B56DB8DD2-876C-4514-8B0D-A4E825206E85%7D

NGU. (2019a). Løsmasser. Retrieved from http://geo.ngu.no/kart/losmasse/

NGU. (2019b). Unstable Rosk Slopes. Retrieved from https://geo.ngu.no/kart/ustabilefjellparti_mobil/?lang=eng

NGU. (2019c). Berggrunnskart. Retrieved from http://geo.ngu.no/kart/berggrunn/

NGU. (2020). InSAR Norway. Retrieved from https://insar.ngu.no/.  Retrieved 27.03.2020 https://insar.ngu.no/

Nordvik, T., Blikra, L. H., Nyrnes, E., & Derron, M.-H. (2010). Statistical analysis of seasonal displacements at the Nordnes rockslide, northern Norway. *Engineering geology, 114*(3-4), 228-237.

Norsk_Klimaservicesenter, institutt, M., NVE, NORCE, & Research, B. c. f. C. (2020). Observasjoner og værstatistikk. Retrieved from https://klimaservicesenter.no/observations/

NVE. (2016). Fare-og risikoklassifisering av ustabile fjellparti–Faresoner, arealhåndtering og tiltak. In L. Blikra, G. Majala, E. Anda, H. Berg, O. Eikenæs, G. Helgås, T. Oppikofer, R. Hermanns, & M. Böhme (Eds.), *NVE Report 77/2016, Norwegian Water Ressources and Energy Directorate, Oslo*.

NVE. (2019). Retrieved from https://www.nve.no/

Nystad, T. (2014). *Stabilitetsanalyse og modellering av det ustabile fjellpartiet Jettan på Nordnesfjellet, Troms.* NTNU,

Osmundsen, P., Redfield, T., Hendriks, B., Bergh, S., Hansen, J.-a., Henderson, I., . . . Anda, E. (2010). Fault-controlled alpine topography in Norway. *Journal of the Geological Society, 167*(1), 83-98.

Petley, D. (2004). The evolution of slope failures: mechanisms of rupture propagation. *Natural hazards and earth system sciences., 4*(1), 147-152.

Ramberg, I. B., Bryhni, I., & Nøttvedt, A. (2006). *Landet blir til*. Trondheim: Norsg Geologsik Forening.

Redfield, T. F., & Hermanns, R. L. (2016). Gravitational slope deformation, not neotectonics: Revisiting the Nordmannvikdalen feature of northern Norway. *Norwegian Journal of Geology/Norsk Geologisk Forening, 96*(3).

Rosen, P. A., Hensley, S., Joughin, I. R., Li, F. K., Madsen, S. N., Rodriguez, E., & Goldstein, R. M. (2000). Synthetic aperture radar interferometry. *Proceedings of the IEEE, 88*(3), 333-382.

Rønning, J., Dalsegg, E., Heincke, B., Juliussen, H., & Tønnesen, J. (2008). Geofysiske målinger på Nordnesfjellet sommeren 2007, Kåfjord kommune, Troms. *NGU Rapport 2008.024*.

Seequent. (2020). Capabilities Leapfrog Works. Retrieved from https://www.leapfrog3d.com/products/leapfrog-works/capabilities

Skrede, I. (2013). *Jettan, Nordnesfjellet, Kåfjord, Troms–indre geometri og struktur, kinematikk og styrande faktorar av eit ustabilt fjellparti, basert på strukturellanalyse, geomorfologi og overvakingsdata.* UiT Norges arktiske universitet,

Skrede, I. (2015). Radarkampanje ved Nordnesfjellet 2014. *Norges vassdrags- og energidirektorat Report 40-2015*, 22.

Sullivan, T. (2007). *Hydromechanical coupling and pit slope movements.* Paper presented at the Proceedings of the 2007 International Symposium on Rock Slope Stability in Open Pit Mining and Civil Engineering.

Temposonics, M. (2019). Temposonics® R-series Position Sensors. Retrieved from http://www.mtssensor.de/products/industrial-sensors/r-series/

Trimble. (2014). NETR9 Geospatial GNSS Receiver.

Tønnesen, J., & Dalsegg, E. (2004). Geofysiske målinger Nordnesfjellet, Kåfjord kommune, Troms. *Norges geologiske undersøkelse Report 2004.012*, 15.

VAISALA. (2006). Vaisala HUMICAP(R) Humidity and Temperature Probes HMP45A/D.

Vick, L. M., Böhme, M., Rouyet, L., Bergh, S., Corner, G. D., & Lauknes, T. R. (2020). Structurally controlled rock slope deformation in northern Norway. Retrieved from https://doi.org/10.1007/s10346-020-01421-7

Wyllie, D. C., & Mah, C. (2004). *Rock slope engineering*: CRC Press.

Xie, H., Pei, J., Zuo, J., & Zhang, R. (2011). Investigation of mechanical properties of fractured marbles by uniaxial compression tests. *Journal of Rock Mechanics and Geotechnical Engineering, 3*(4), 302-313.

Zwaan, K. (1988). Nordreisa, berggrunnsgeologisk kart–M 1: 250 000. *Norges geologiske undersøkelse*.

# Appendix

## Appendix A: Link for downloading of Leapfrog viewer:

https://www.leapfrog3d.com/products/seequent-view?gclid=Cj0KCQjw-_j1BRDkARIsAJcfmTFyAC6BzXfXvB7tuFvprhCSVfURKECjz0yOaAtWFRElcMA1yCmUlvwaAqUGEALw_wcB